



Influence of clouds on the solar radiation budget

H.M. Denke

Koninkrijk der Nederlanden

Scientific report = Wetenschappelijk Rapport; WR 2002-09

De Bilt, 2002

PO Box 201, 3730 AE De Bilt
The Netherlands
Wilhelminalaan 10
<http://www.knmi.nl>
Telephone +31 30 22 06 911
Telefax +31 30 22 10 407

Author: Hartwig Manfred Deneke

*Also published as Ph.D. thesis
Rheinische Friedrich-Wilhelms-Universität
Bonn, December 2002*

UDC: 550.521.1
551.576.1
(043-3)

ISSN: 0169-1651

ISBN: 90-369-2226-7



Influence of clouds on the solar radiation budget

H.M. Deneke

*I've looked at cloud from both sides now
From up and down, and still somehow
It's cloud illusions I recall
I really don't know clouds at all*

– Joni Mitchell

To Sinidu

Contents

Abstract	v
Zusammenfassung	vii
1 Introduction	1
1.1 Motivation	1
1.2 Overview	2
1.3 Structure	3
2 Theoretical Basis	5
2.1 Formulation of the Problem	5
2.1.1 Geometrical Setup	5
2.1.2 Solar Position and Solar Constant	6
2.1.3 Satellite Navigation and Image Geolocation	7
2.1.4 Surface Albedo	7
2.2 Atmospheric Radiative Transfer	7
2.2.1 Definitions	7
2.2.2 Origin of Radiation	10
2.2.3 Broad-band Quantities	11
2.2.4 Radiative Transfer Equation	12
2.2.5 Optical Properties of Atmospheric Constituents	13
3 Measurements	17
3.1 Pyranometer	17
3.1.1 Principle of Operation and Instrument Description	17
3.1.2 Measurement Accuracy	18
3.1.3 Pyranometer Calibration and its Accuracy	20
3.1.4 Combined Uncertainty of Measured Irradiances	25
3.2 Advanced Very High Resolution Radiometer	26
3.2.1 Principle of Operation and Instrument Description	26
3.2.2 Quantitative Analysis of AVHRR Data	26
3.2.3 AVHRR Calibration and its Uncertainty	27
4 Accuracy of Modeled Clear-Sky Global Surface Irradiances	31
4.1 Introduction	31
4.2 Sensitivity of the Clear-Sky Shortwave Atmospheric Transmissivity	32

CONTENTS

4.2.1	Atmospheric Gases	33
4.2.2	Aerosols	34
4.2.3	Surface Albedo	35
4.2.4	Solar Constant	36
4.2.5	Further Sensitivities	36
4.2.6	Conclusions	37
4.3	Model Intercomparison	37
4.3.1	Water Vapor Absorption	38
4.3.2	Radiation Budget for the Reference Atmosphere	39
4.3.3	Conclusions	40
4.4	Comparison of Model Calculations and Measurements	40
4.4.1	Measurements	41
4.4.2	Model Data	41
4.4.3	Comparison	42
4.5	Summary and Conclusions	44
5	Comparison of Cloud Optical Depths Retrieved from Transmitted and Reflected Solar Radiation	47
5.1	Introduction	47
5.2	Instrumental Data	48
5.2.1	Pyranometer	49
5.2.2	NOAA-14 AVHRR	49
5.3	Retrieval Technique	50
5.3.1	Radiative Transfer Model	51
5.3.2	Retrieval Procedure	52
5.3.3	Sensitivity of the Retrievals	53
5.4	Comparison of Retrieval Results	54
5.5	Discussion	57
5.5.1	Monte Carlo Model of the Retrieval Process for the Error Analysis	58
5.5.2	Measurement Uncertainties	58
5.5.3	Violation of Retrieval Assumptions	60
5.6	Summary and Conclusions	61
6	Retrieval of Solar Surface Irradiance from Satellite Measurements of the TOA Narrowband Reflectance	63
6.1	Introduction	63
6.2	Retrieval Method and Dataset	64
6.3	Validation	65
6.4	Discussion	71
6.4.1	Radiative Transfer Calculations	71
6.4.2	Instrumental Accuracy	72
6.4.3	Effects of Variability	73
6.5	Conclusions and Outlook	76

7 Evaluation of Model Predictions of Cloud Parameters and the Solar Radiation Budget	79
7.1 Introduction	79
7.2 Model Setup	80
7.3 Water Vapor	81
7.4 Cloud Cover	84
7.5 Cloud Transmissivity	88
7.6 Summary and Discussion	90
8 Conclusions and Outlook	95
A Pyranometer Stations	99
B Calibration Coefficients of the NOAA-14 AVHRR	101
C Aerosol Optical Properties	103
D Notation	105
D.1 List of Symbols	105
D.2 List of Subscripts	106
D.3 List of Acronyms	107
List of Figures	109
List of Tables	110
References	112
Acknowledgements	125
Curriculum Vitae	127

Abstract

This thesis investigates the accuracy of a current radiative transfer scheme and a single-column model for representing the influence of clouds on the solar radiation budget. An extensive set of pyranometer measurements and satellite observations collected throughout the Netherlands is used for this purpose.

First, an overview of the relevant parts of the theory of atmospheric radiative transfer is given and a literature study of the instrumental uncertainties of the dataset is presented. Special attention is paid to the thermal offset of pyranometers, which has recently been identified as the origin of a significant systematic underestimate of measured solar irradiances. A mechanism is proposed whereby the thermal offset can lead to additional calibration errors not accounted for in previous estimates of the pyranometer uncertainty. In combination with the direct effects of the thermal offset, a large range of systematic pyranometer errors has to be expected, which significantly exceeds the range specified by the World Meteorological Organization for these type of instruments.

A correct modeling of clear-sky atmospheric radiative transfer is an essential prerequisite for a correct treatment of cloudy atmospheres in radiative transfer models. To evaluate its accuracy, six years of global surface irradiance records obtained throughout the Netherlands during cloud-free situations are compared to model output of five different radiative transfer schemes, providing 6,132 individual cases. Two models calculate a significantly lower atmospheric absorption by gases in comparison to the other models. This is probably the consequence of the older spectroscopic datasets used for the parameterization of gas absorption. The three models based on more recent spectroscopic data show good agreement in radiative fluxes at the top of atmosphere and the surface. However, large uncertainties are introduced by the limited knowledge of aerosol optical properties for the current dataset. Compared to pyranometer measurements, the recent models overestimate the atmospheric transmissivity by 4.5% on average throughout the full range of solar zenith angles. This causes a mean overestimate of the global irradiance of 27 W m^{-2} . Systematic error sources in the measurements and the model assumptions are large enough to explain the full magnitude of the discrepancy. Therefore, the accuracy of the data is too limited to identify any shortcomings in the models or in the representation of aerosols used.

The main parameter determining the reduction of atmospheric transmissivity in cloudy conditions is the cloud optical depth. Retrieval results of two algorithms to infer the cloud optical depth from transmitted broad-band and reflected narrow-band solar radiation are compared in Ch. 5. The algorithms are applied to a six-year dataset of about 40,000 pyranometer measurements collected by 32 meteorological stations in the Netherlands and to 1,500 simultaneous and collocated observations of the $0.63 \mu\text{m}$

radiance inferred by the AVHRR instrument on board the NOAA-14 satellite. Both a strong negative bias of 22 – 46 % and a large random scatter are found for satellite-retrieved versus pyranometer-retrieved cloud optical depths. While the magnitude of the scatter is reduced if a selection of cases is made to restrict horizontal cloud inhomogeneity, no such dependence is present for the bias. Quantifying the impact of measurement uncertainties, it is possible to attribute the full bias to systematic errors in satellite calibration and pyranometer measurements. This finding highlights the importance of high instrumental accuracy for trustworthy retrieval results. Furthermore, the assumptions inherent in a comparison of a spatially extended instantaneous measurement to a temporally averaged time series of a point measurement are shown to contribute substantially to the observed scatter and to introduce a small bias.

Based on the methods used for the previous comparison, an algorithm is presented in Ch. 6 to derive the downwelling solar surface irradiance from satellite estimates of the $0.63\ \mu\text{m}$ reflectance, which explicitly accounts for variations in cloud optical depth and integrated water vapor. For validation, the dataset of 40,000 pyranometer measurements and 1,500 NOAA-14 AVHRR satellite scenes is used. A mean overestimate of the satellite-retrieved irradiance by 7 % is found, which is consistent with numerous other studies reporting positive biases of atmospheric transmissivities calculated by radiative transfer schemes in comparison to measurements. If a water cloud is assumed in the retrieval, a strong dependence of retrieval bias on solar zenith angle is found. The information available for the present study is insufficient to find a full explanation for this behavior. Using 40-minute averages of pyranometer measurements and a region of about $150\ \text{km}^2$ for the satellite analysis, a good performance of the retrieval is found for monthly averages and averages of all stations for individual satellite overpasses, resulting in RMSEs of $12\ \text{W m}^{-2}$ and $33\ \text{W m}^{-2}$, respectively. A comparison with individual measurements shows a much larger scatter of $85\ \text{W m}^{-2}$. Evidence is presented which suggests that a significant fraction of the scatter originates from the variability of the irradiance field caused by cloud inhomogeneities.

The study presented in Ch. 7 evaluates the representation of humidity, cloud amount and shortwave atmospheric transmissivity in a single-column model derived from the ECHAM4 GCM in comparison to radiosonde profiles, pyranometer measurements and synoptic reports. The model captures only part of the observed variance of relative humidity in the middle troposphere, and only about 40 % of the variance is explained by the model forecasts. A mean underestimate of total cloud amount by 14 % is found in comparison to synoptic reports. In the presence of clouds, the atmospheric transmissivity is strongly underestimated, indicating a general overestimate of the cloud optical depth. The model skill for predicting both the cloud amount and the atmospheric transmissivity on a case-by-case basis is found to be rather low. Similar types of shortcomings are typical for the current generation of climate models and highlight that the representation of clouds and cloud-radiation interactions need to be significantly improved for an accurate simulation of the climate system.

Zusammenfassung

Diese Arbeit untersucht die Genauigkeit, mit der ein aktuelles Strahlungstransportmodell und einem eindimensionalen Klimamodell den Einfluss von Wolken auf den solaren Strahlungshaushalt reproduzieren. Dazu wird ein umfangreicher Datenbestand von Pyranometermessungen und Satellitenbildern aus den Niederlanden verwendet.

Zunächst werden eine Übersicht der Theorie des atmosphärischen Strahlungstransports und eine Literaturstudie der instrumentellen Genauigkeit des verwendeten Datensatzes präsentiert. Besondere Aufmerksamkeit wird dabei auf den thermischen Offset von Pyranometern gerichtet, der unlängst als Ursache für eine systematische Unterschätzung der gemessenen solaren Einstrahlung identifiziert wurde. Ein Mechanismus wird postuliert, durch den der thermische Offset zusätzliche Eichfehler hervorrufen kann und der in herkömmlichen Schätzungen der Genauigkeit nicht berücksichtigt worden ist. In Verbindung mit dem direkten Einfluss des thermischen Offsets führt er zu einer deutlich größeren Spanne von systematischen Fehlern, als sie die World Meteorological Organization für diesen Typ von Instrumenten angibt.

Eine genaue Modellierung von wolkenfreien Fällen ist eine wichtige Voraussetzung für eine korrekte Behandlung des Strahlungstransports unter bewölkten Bedingungen. Um die Genauigkeit zu testen, werden 6.132 Messungen, die unter wolkenfreien Bedingungen in den Niederlanden über einen Zeitraum von 6 Jahren gesammelt wurden, mit den Ergebnissen von fünf Strahlungstransportmodellen verglichen. Zwei Modelle berechnen eine deutlich geringere Absorption durch atmosphärische Gase in Vergleich zu den anderen Modellen, vermutlich als Folge der älteren spektroskopischen Datensätze, die den verwendeten Parameterisierungen zugrunde liegen. Die drei Modelle, die auf neueren spektroskopischen Daten basieren, zeigen eine gute Übereinstimmung in Strahlungsflüssen am Erdboden und an der Obergrenze der Atmosphäre. Eine große Unsicherheit wird jedoch durch das begrenzte Wissen über die optischen Eigenschaften von Aerosolen hervorgerufen. Im Vergleich zu Pyranometermessungen wird die atmosphärische Transmission um etwa 4.5% bzw. die solare Einstrahlung um 27 W m^{-2} am Erdboden überschätzt. Der Bereich der Unsicherheiten von Messungen und verwendeten Eingangsparametern für die Berechnungen ist jedoch groß genug, um die festgestellte Diskrepanz komplett erklären zu können. Deshalb lassen sich keine Schwächen an den Modellen oder der verwendeten Beschreibung von Aerosolen folgern.

Die optische Dicke von Wolken ist der Parameter, der in bewölkten Situationen hauptverantwortlich für die Reduktion der atmosphärischen Transmission solarer Strahlung ist. Ergebnisse zweier Algorithmen zur Ableitung der optischen Dicke von Wolken aus reflektierten schmalbandigen Strahldichten und breitbandiger solarer Einstrahlung am Erdboden werden in Kapitel 5 verglichen. Zur Validierung werden beide Algorithmen auf einen Datensatz von 40.000 Pyranometermessungen von 32 meteorologi-

schen Stationen in den Niederlanden sowie auf zeitlich und räumlich übereinstimmende Messungen der $0.63\ \mu\text{m}$ Strahldichte des AVHRR Instruments an Bord des NOAA-14 Satelliten angewendet. Die Ergebnisse zeigen sowohl eine deutliche Überschätzung der optischen Dicke aus Pyranometerdaten im Vergleich zu satellitenabgeleiteten Werten um 22 -- 46 %, als auch eine erhebliche Streuung. Eine Einschränkung der Fälle zur Begrenzung der Wolkeninhomogenität reduziert die Streuung, hat aber keinen Einfluss auf den systematischen Fehler. Eine quantitative Analyse des Einflusses von Messfehlern zeigt, dass der systematische Fehler möglicherweise komplett durch Ungenauigkeiten in den Satelliten- und Pyranometermessungen erklärt werden kann, was die Bedeutung einer hohen Messgenauigkeit für die Ableitung der optischen Dicke von Wolken verdeutlicht. Ferner wird gezeigt, dass eine Verletzung der Annahmen, die dem Vergleich einer Punkt- mit einer Flächenmessung zugrunde liegen, einen erheblichen Anteil der Streuung verursachen.

Auf Basis der Methodik des vorigen Vergleichs wird in Kapitel 6 ein Algorithmus zur Ableitung der solaren Einstrahlungen aus Satellitenmessungen der $0.63\ \mu\text{m}$ Strahldichte vorgestellt, der explizit Variationen der optischen Dicke von Wolken und des vertikal integrierten Wasserdampfgehalts berücksichtigt. Zur Validierung wird derselbe Datensatz von 40.000 Pyranometer- und 1500 Satellitenmessungen des NOAA-14 AVHRR Instruments verwendet. Der Algorithmus überschätzt die mittlere Einstrahlung um 7% im Vergleich zu Messungen. Dieses Ergebnis ist konsistent mit den Ergebnissen etlicher weiterer Studien, die ebenfalls eine Überschätzung der atmosphärischen Transmission durch Strahlungstransportmodelle feststellen. Ein Vergleich von über 40 Minuten gemittelte Pyranometerdaten und einer Region von etwa $150\ \text{km}^2$ entsprechenden Satellitenmessungen zeigt eine gute relative Genauigkeit des Algorithmus für Monatsmittel und Mittelwerte aller 32 Stationen, mit Standardabweichungen von jeweils $12\ \text{Wm}^{-2}$ und $33\ \text{Wm}^{-2}$. Ein Vergleich einzelner Fälle zeigt hingegen eine deutlich grössere Streuung von $85\ \text{Wm}^{-2}$. Es werden Indizien präsentiert, die nahelegen, dass ein bedeutender Teil der Streuung auf die Variabilität im Strahlungsfeld auf der räumlichen Skala der Pyranometermessung zurückzuführen ist, die durch Wolkeninhomogenität hervorgerufen wird.

Die Studie in Kapitel 7 vergleicht die Repräsentation von Feuchte, dem Bedeckungsgrad von Wolken und der atmosphärischen Transmission von solarer Strahlung in einem eindimensionalen Modell, das auf dem ECHAM4 GCM basiert. Für diesen Vergleich werden Radiosondenprofile, synoptischen Beobachtungen und Pyranometermessungen verwendet. Das Modell gibt nur einen Teil der beobachteten Varianz in relativer Feuchte in der mittleren Troposphäre wieder. Ferner wird lediglich 40% der Varianz von den Modellvorhersagen erklärt. Der mittlere Bedeckungsgrad von Wolken wird im Vergleich zu synoptischen Beobachtungen um 14% unterschätzt. In bewölkten Fällen ist eine zu geringe atmosphärische Transmission feststellbar, was auf eine zu große mittlere optischen Dicke von Wolken hinweist. Die Übereinstimmung von Modellvorhersagen und beobachtetem Bedeckungsgrad und gemessener atmosphärischer Transmission für einzelne Fälle ist recht gering. Ähnliche Schwächen sind typisch für die aktuelle Generation von GCMs und ein Anzeichen dafür, dass die Beschreibung von Wolken und ihrer Interaktion mit Strahlung deutlich verbessert werden müssen, um das Klimasystem realistisch simulieren zu können.

Chapter 1

Introduction

1.1 Motivation

The driving force of the Earth's climate system is the radiation originating from the sun (Lorenz, 1955). The inhomogeneous zonal insolation results in a differential heating of the atmosphere, which is balanced by the general atmospheric circulation and a net transport of heat towards the poles. Accurate and regionally resolved information about the radiation budget is one of the key prerequisites for an understanding of the climate system and its susceptibility to change due to natural and anthropogenic forcings.

To judge the level of understanding of such a complex dynamic system, the important processes have to be represented in a model, and its predictions compared with observations. As a result, the development in climate research has been an evolutionary cycle, driven by advances in the relevant scientific topics and the accumulation of their findings in *General Circulation Models* (GCMs). Increases in computational power and more accurate measurement techniques for the identification of remaining shortcomings have aided the progress. *Numerical Weather Prediction Models* (NWP) have evolved in parallel, with higher priority on short-term weather forecasting skills at high spatial resolution, and less interest in matching long-term climatologies of observations and accurately representing the underlying physical processes and feedbacks.

Several scientific fields have contributed their insights into the processes which are of relevance to the climate system and need to be represented in numerical models. For the context of this thesis, the following subjects are of particular importance: Radiative transfer theory describes the propagation and distribution of radiation for a known atmospheric state and is mainly based on the foundations of classical electrodynamics. Dynamical meteorology and thermodynamics provide the equations determining the evolution of the atmospheric state. Cloud and aerosol microphysics study the formation and development of the hydrometeors dispersed in the atmosphere of relevance for the climate.

The interaction of radiation with atmospheric gases, aerosols and clouds needs to be accounted for in estimates of the radiation budget and in models of the climate system. The remaining uncertainty originating from the scattering and absorption properties of atmospheric gases are rather small. The direct effects of aerosols are known with much lower accuracy (Penner et al., 1994, this thesis). However, the largest source

of uncertainty is introduced by the formulation of cloud processes and cloud-radiation interactions (IPCC, 2001). Several reasons are responsible for this uncertainty. The radiation budget is very sensitive to changes in cloud microphysical and optical properties (Hu and Stamnes, 2000). The accuracy of predicted cloud parameters is currently rather low due to the complex, non-linear nature of cloud processes. The treatment of variability at spatial scales not resolved by the model is an unsolved problem, especially for the modeling of convection and convective clouds. The feedback processes influencing the relation of cloud microphysics and the resulting radiative properties are not fully understood and thus cannot be included correctly in models. The algorithms used in the radiative transfer schemes of GCMs have to trade off accuracy and numerical efficiency (Wild et al., 1998).

To overcome these difficulties, there is a need for comparisons of the model-predicted and measured radiative quantities and their dependence on cloud properties. Traditionally, surface based instruments have been the main source of evaluation data. Since the last two to three decades, satellites play an increasingly important role in model evaluation. Satellite observations provide a much better spatial coverage than the network of ground based measurements, as there is only a limited number of stations which are distributed very inhomogeneously. Moreover, satellites can obtain measurements at the top of atmosphere, which complement the surface measurements and can therefore be used to test the closure of radiative transfer models.

But as a result of the quick development of this field, many of the algorithms are still experimental, and the instrumental shortcomings are not as well understood as for the ground-based measurements. Thus, an important part of satellite remote sensing research is the task of validation of the derived products, to make sure that they provide a consistent picture together with traditional surface measurements.

1.2 Overview

This thesis studies the radiation budget of the broadband solar spectrum for the Netherlands, making use of a very dense network of surface measurement stations, detailed supplementary cloud information, and collocated observations by the AVHRR instrument on board the NOAA-14 satellite. Constraining the study to a single region limits the representativeness of the conclusions for the global scale. On the other hand, it offers an ideal and unique dataset for a thorough comparison of different measurement techniques and complements global studies such as the *International Satellite Cloud Climatology Project* (ISCCP), which have to be restricted to a much coarser resolution due to storage, computational and technical constraints.

The approach taken here is based on the fundamental assumption that current radiative transfer models represent the radiation budget *well enough* in clear-sky conditions for most applications. After a verification of this statement, the deviations for cloud-covered scenes are studied. The main parameter determining the radiative effects of a cloud is the cloud optical depth. Special focus will be given to techniques for its retrieval. Nevertheless, other quantities are shown to be of importance for a proper representation of cloud-radiation interactions in the solar spectral region.

This thesis investigates two different aspects of modeling. On the one hand, a detailed

radiative transfer scheme, representing the current level of knowledge, is used as basis for an analysis of a six-year dataset of satellite and surface measurements, enabling a good estimate of the overall consistency of the observations and the calculations of the model.

On the other hand, the representation of clouds and shortwave radiative fluxes in a single-column model based on the formulation of physical processes included in the ECHAM4 GCM is compared with observations for a 4-year time period. This comparison allows an assessment of the combined effects of predicted microphysical cloud parameters and the highly parameterized description of the resulting cloud-radiation interactions.

1.3 Structure

This thesis is structured as follows: Formal definitions of the quantities studied in the thesis and an overview of the theory required for their modeling are presented in Ch. 2. The instruments used for the measurements are described in Ch. 3, including a thorough evaluation of their expected accuracy. In Ch. 4, measurements obtained during clear-sky situations are compared with calculations of both sophisticated radiative transfer schemes and a highly parameterized model developed for use in GCMs. This is done in order to avoid the attribution of errors in the treatment of gas absorption and aerosol properties to shortcoming in the representation of clouds in the following studies. Results of two methods to retrieve cloud optical depth from the narrow-band reflectance inferred by the NOAA satellites and the broadband atmospheric transmissivity as measured by pyranometers are compared in Ch. 5. This comparison provides a consistency test of measured and modeled radiative quantities at the top of atmosphere and the surface. Based on the methodology developed for the previous investigation, a retrieval scheme to estimate the downwelling solar irradiance at the surface from narrow-band satellite measurements is described and validated in Ch. 6, which explicitly accounts for variations in cloud optical depth and vertically integrated water vapor. Ch. 7 evaluates the output of a single-column model based on the physical parameterisation of the ECHAM4 GCM with synoptic reports, radiosonde profiles and pyranometer measurements. In Ch. 8, the principle conclusions of this thesis are summarized and an outlook to possible extensions of the work is given.

Chapter 2

Theoretical Basis

Two quantities directly related to the solar radiation budget of the Earth's atmosphere are studied in this thesis. The first quantity is the total amount of solar radiation reaching the surface. The second quantity is the fraction of radiation reflected back into space at an arbitrary angle, as seen e.g. by meteorological satellites. Both parameters are readily available from measurements, and are used to gain insight into the radiative processes taking place within the Earth-atmosphere system.

A comparison of actual measurements and values predicted by models is used to evaluate our understanding of the underlying processes. In this chapter, the methods used for modeling both quantities are presented. After a formulation of the problem, a summary of atmospheric radiative transfer theory is given. It is mainly based on classical electrodynamics and applies Maxwell's equations to the interaction of radiation with the Earth's atmosphere. Hence, it provides the tools for calculating the radiation field and represents our understanding of the relevant processes.

2.1 Formulation of the Problem

The measurement geometry underlying the pyranometer and the satellite observations is shown in Fig. 2.1. Shortwave radiation originating from the sun passes through the atmosphere, and interacts with air molecules, aerosols and clouds. Radiation is either reflected back into space, absorbed within the atmosphere, or absorbed by the surface. The amount of downwelling radiation incident at the surface is measured by the pyranometer, while the satellite records photons reflected back into space in the direction of the satellite. The representation of the observational setup in a model requires the specification of the geometry and boundary conditions, as given by the direction and amount of incident irradiation, the position of the satellite, and the reflection characteristics of the surface. In combination with the optical properties of the atmosphere, these parameters need to be specified to form a well-defined mathematical problem.

2.1.1 Geometrical Setup

The local coordinate system of a given location on the Earth's surface is a convenient choice for describing the geometrical setup of radiative transfer calculations. Then,

2.1 Formulation of the Problem

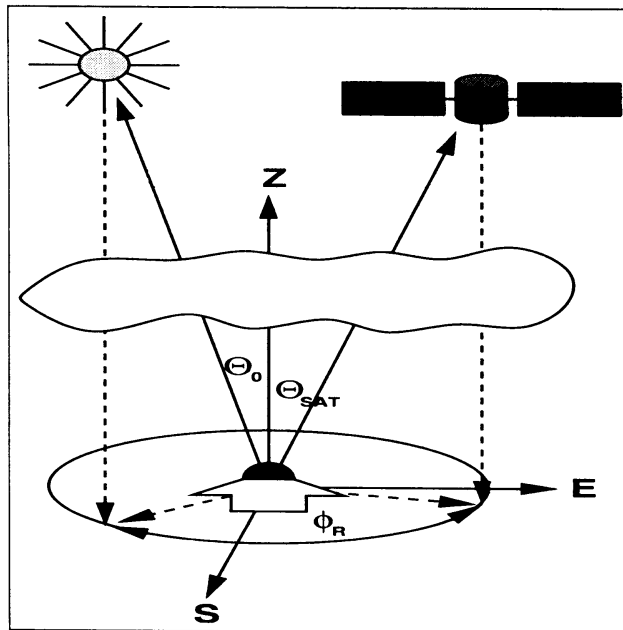


Figure 2.1: Schematic description of the measurement geometry analyzed within the thesis. A pyranometer determines the downwelling solar radiation at the surface. A radiometer on board of a satellite infers the amount of radiation reflected back into space at a known viewing geometry.

the sun's position in the sky can be specified by two angles, which are chosen as the solar zenith angle θ_0 and the azimuth angle ϕ_0 . The azimuth is defined as the angle between geographic North and the projection of the sun on the Earth's surface in clockwise direction. The position of a satellite can be described likewise by its zenith and azimuth angles θ_{SAT} and ϕ_{SAT} . If the reflection properties of surface and atmosphere are independent of the azimuth angle, only the two zenith angles and the relative azimuth, which is the difference ϕ_r between the azimuth angles ϕ_{SAT} and ϕ_0 , are relevant for radiative transfer calculations due to the symmetry of the problem.

2.1.2 Solar Position and Solar Constant

The Earth moves in an elliptical orbit around the sun. To determine the sun's position in the sky for a given geographic location on the Earth, both the Earth's rotation around its polar axis and the relative positions of Earth and sun need to be taken into account. The algorithm of Michalsky (1988a) is used throughout this thesis for this purpose, with the corrections and modifications proposed by Michalsky (1988b) and Spencer (1989). The energy reaching the Earth is inversely proportional to the square of the sun - Earth distance δ_{SE} due to the energy conservation principle. As this distance is large compared to the radius of the sun, the incident radiation can be assumed as a parallel beam. At the mean distance, the solar constant F_{\odot} , the amount of solar irradiance incident on a surface perpendicular to the direction of the solar beam, is approximately 1368 Wm^{-2} , the value used throughout this thesis. All measured irradiances are renormalized to refer

to mean sun - Earth distance. The actual distance is calculated with the algorithm of Spencer (1971). The spectral solar constant reported by Kurucz (1995) has been used to determine the amount of radiation contained within a spectral interval.

2.1.3 Satellite Navigation and Image Geolocation

The procedure of geolocating a pixel from a satellite image requires the accurate knowledge of the satellite's position relative to the Earth, together with the viewing angle of the instrument. For the NOAA series of satellites, the position is calculated using the Brouwer- Lyddane orbital propagators (Lyddane, 1963), a set of parameters describing the motion of the satellite in an approximated form of the Earth's gravitational field. The required orbital elements are obtained from the TBUS bulletins (Kidwell, 1998). A pixel's latitude and longitude is then found by the intersection of a line originating from the satellite at the given viewing direction with the Earth's surface. Using basic geometry, the satellite's zenith and azimuth angles are obtained. A detailed description of the procedure is given in the NOAA Polar Orbiter Data User's Guide (Kidwell, 1998).

2.1.4 Surface Albedo

The surface albedo, the amount of radiation reflected by the surface, is an important quantity in radiative transfer as it specifies the lower boundary condition. Its magnitude can vary significantly with wavelength and direction of incidence, depending on the type of surface. The specification of a realistic value is especially important for modeling cloudy atmospheres, as radiation can be reflected multiple times between the surface and cloud layers. Limited information exists about the albedo and its angular and spectral dependence for the measurement sites considered for this thesis.

2.2 Atmospheric Radiative Transfer

A summary of the theory of atmospheric radiative transfer is given, as far as it is needed for the understanding of the methods used in this thesis. More detailed discussions can be found in the standard textbooks on atmospheric radiative transfer, such as Goody and Yung (1989) and Lenoble (1993).

2.2.1 Definitions

Solar energy reaching the Earth is transported by means of electromagnetic waves. According to quantum mechanics, these consist of individual photons having a wavelength λ , which carry a fixed amount of energy E given by $E = \frac{hc}{\lambda}$. Here, h is the Planck constant and c is the speed of light. Thus, the amount of energy transported by an electromagnetic wave depends solely on the number of photons and their wavelength.

Radiance and Irradiance The number of photons carrying an energy amount dE that reach a surface out of a solid angle element $d\Omega$ is proportional to the time of

2.2 Atmospheric Radiative Transfer

exposure dt , the surface area ds and the width $d\lambda$ of the spectral range considered. The *spectral radiance* I_λ is therefore defined as

$$I_\lambda \equiv \frac{dE}{ds dt d\lambda d\Omega}. \quad (2.1)$$

The surface area ds either has to be oriented perpendicular to the propagation direction of the photons, or both the area ds and the solid angle $d\Omega$ have to be treated as vector quantities with lengths equal to their sizes and directions normal to their orientation. A tilt of angle θ between ds and $d\Omega$ is then accounted for by the scalar product of both vectors, resulting in $I_\lambda(\theta) = \cos(\theta) I_\lambda = \mu I_\lambda$, where μ denotes the cosine of the angle θ .

The *spectral irradiance*, also referred to as net flux, is a measure for the net energy transported through a given horizontal unit surface per unit time and wavelength interval, and can be derived by integrating the contribution of radiance from a particular direction over the full hemisphere according to

$$F_\lambda \equiv \int_{\Omega} I_\lambda \cos(\theta) d\Omega = \int_{-\pi/2}^{\pi/2} \int_0^{2\pi} I_\lambda \sin(\theta) \cos(\theta) d\phi d\theta = \int_{-1}^1 \int_0^{2\pi} I_\lambda \mu d\phi d\mu. \quad (2.2)$$

Here, the integration over the total hemisphere has been split into integrations over the cosine of the zenith angle μ and the azimuth angle ϕ .

Of interest are also the upward (+) and downward (-) components F_λ^\pm of the irradiance. They describe the flux of energy through a surface out of the upper and lower hemisphere, and are defined by

$$F_\lambda^\pm \equiv \int_0^{\pm 1} \int_0^{2\pi} I_\lambda \mu d\phi d\mu. \quad (2.3)$$

They are related to the spectral irradiance by

$$F_\lambda = F_\lambda^+ - F_\lambda^-. \quad (2.4)$$

Using this notation, both hemispheric irradiances are positive-semidefinite.

Optical Path and Optical Depth The interaction of radiation with a medium is described by three processes, which are emission, scattering and absorption. The sum of the scattering and absorption cross-sections is also referred to as the extinction cross-section. Within the Earth's atmosphere, these interactions are caused by air molecules, and by cloud and aerosol particles. Hence, the strength of the interaction is proportional to the particle number densities η , where the proportionality constant is the extinction cross-section k_λ , which depends on both particle type and wavelength.

For a light beam propagating from point $P1$ to $P2$, the optical path $\tilde{\tau}$ can be defined as

$$\tilde{\tau}_\lambda \equiv \int_{P1}^{P2} k_\lambda \eta ds, \quad (2.5)$$

where ds is the geometrical path length. Either a mean extinction cross-section has to be used, or the contributions of particles having different extinction cross-sections have to be added individually.

Within a plane-parallel atmosphere subdivided into horizontally homogeneous layers, a layer ranging from lower height z_1 to an upper height z_2 having a thickness $\Delta z = z_2 - z_1$ can be assigned an optical depth, the optical path along the zenith direction, according to

$$\tau_\lambda(z_1, z_2) \equiv \int_{z_1}^{z_2} k_\lambda(z') \eta(z') dz'. \quad (2.6)$$

Setting z_2 to the height of the top of atmosphere and omitting the subscript for z_1 , the optical depth becomes a monotonously decreasing function of z and is often used as vertical coordinate for plane-parallel atmospheres instead of the height.

Transmissivity, Reflectivity and Absorptivity For a horizontally homogeneous layer as described above, three quantities can be defined which characterize the fraction of incident radiation that is absorbed, reflected or transmitted by that layer. Assuming an illumination originating from the upper hemisphere and excluding any contributions from radiation sources within that layer, the transmissivity for downwelling radiation is given by

$$\mathcal{T}_\lambda \equiv \frac{F_\lambda(z_1)}{F_\lambda^-(z_2)}. \quad (2.7)$$

It is the ratio of irradiance leaving the layer at the bottom to the incident irradiance.

Similarly, the reflectivity is defined as the fraction of irradiance reflected back into the upper hemisphere

$$\mathcal{R}_\lambda \equiv \frac{F_\lambda^+(z_2)}{F_\lambda^-(z_2)}. \quad (2.8)$$

The reflectivity is also commonly referred to as the hemispherical albedo, or only albedo.

Radiation which is neither transmitted nor reflected has to be absorbed, leading to the following definition of the absorptivity

$$\mathcal{A}_\lambda \equiv \frac{F_\lambda(z_1) - F_\lambda(z_2)}{F_\lambda^-(z_2)}. \quad (2.9)$$

The principle of conservation of energy is then expressed by the equation

$$1 = \mathcal{R}_\lambda + \mathcal{T}_\lambda + \mathcal{A}_\lambda. \quad (2.10)$$

It should be noted that all three quantities generally depend not only on the layer optical properties, but also on the angular distribution of the incident irradiance field and the up- or downward direction. Commonly, these quantities are specified for the complete atmosphere by setting z_2 to the top of atmosphere and z_1 to the surface. Making use of the notation introduced above, the Earth's surface can be treated as an infinitesimally thin layer with zero transmissivity.

Phase Function and Anisotropy The probability of a photon to be deflected by a specified angle θ through particle scattering is given by the particle's phase function \mathcal{P} . For spherical particles, as well as an average of many arbitrarily shaped and randomly

2.2 Atmospheric Radiative Transfer

oriented particles, P is independent of the direction of incidence, and only a function of scattering angle θ . As a probability, it is normalized to unity according to

$$\frac{1}{4\pi} \int_{\Omega} \mathcal{P}_{\lambda}(\theta) d\Omega = 1. \quad (2.11)$$

A scatterer is called isotropic, if its phase function is constant for all scattering angles.

For a layer or surface illuminated by a collimated beam of radiation, the bidirectional reflectance distribution function (BRDF) ϱ describes the angular variations of the scattered radiance field I_{SCAT} . It depends on the direction (θ_{IN}, ϕ_{IN}) of the incident radiation, the beam's irradiance F_{IN} , as measured normal to the direction of propagation, and the direction of the outgoing radiance $(\theta_{OUT}, \phi_{OUT})$. It is defined as

$$\varrho_{\lambda}(\theta_{OUT}, \phi_{OUT}, \theta_{IN}, \phi_{IN}) \equiv \frac{\pi I(\theta_{OUT}, \phi_{OUT})}{\cos(\theta_{IN}) F(\theta_{IN}, \phi_{IN})}. \quad (2.12)$$

In this definition, the angle θ_{in} has been chosen as the tilt angle between the surface normal and the direction of the incident beam. Surfaces with a BRDF independent of the direction of incidence and reflection are called Lambertian. In this case, unity is an upper limit for the case of total reflection.

The angular distribution model (ADM) ζ is the ratio of the BRDF and the reflectivity, given by

$$\zeta_{\lambda} \equiv \frac{\varrho_{\lambda}}{\mathcal{R}_{\lambda}}. \quad (2.13)$$

For a specific direction of the incident beam, it describes the deviation of the resulting radiance field from an isotropic radiance distribution of a layer or surface having an equal reflectivity.

2.2.2 Origin of Radiation

Thermal emission is the dominant source of radiation originating from both the sun and the Earth. The intensity and spectral distribution of the radiation is then determined by the temperature of the source, as well as the source's efficiency for emitting radiation. A blackbody is an object that absorbs all incoming radiation. In this case, Kirchhoff's law demands that it also emits with the maximum possible efficiency. For such a blackbody, the emitted radiance is only a function of temperature and wavelength, and is given by Planck's Law

$$I(T, \lambda) = \frac{2 h c^2}{\lambda^5 (e^{hc/\lambda kT} - 1)}. \quad (2.14)$$

Integrating the radiance of a surface over all frequencies and the complete upper hemisphere, the total amount of energy radiated by a black body can be obtained using Stefan-Boltzmann's law, which states that

$$F^+ = \int_0^{\infty} F(T) d\lambda = \sigma T^4, \quad (2.15)$$

using the Boltzmann constant σ .

The solar spectrum closely follows the spectrum of a blackbody having a temperature of 5820 K, even though absorption and emission lines in the sun's corona cause some deviations. From the amount of incident solar radiation and an estimated planetary albedo of 0.3, the Earth's effective radiative temperature is found to be about 255 K, well within the range of temperatures observed at the surface and within the Earth's atmosphere.

The large difference in temperature in combination with the large distance of sun and Earth allows a separate treatment of radiation originating from the sun and radiation emitted by the Earth's atmosphere and the surface. Only solar radiation is considered further in this thesis.

2.2.3 Broad-band Quantities

The quantities discussed so far apply only to monochromatic radiation of a given wavelength, as indicated by their subscript λ . As seen from Planck's law (Eq. 2.14), the solar radiation is distributed over a wide range of wavelengths, with the main part confined to the spectral interval from 0.2 to 4.0 μm .

For studying the solar radiation balance, radiation within this wavelength interval has to be considered. Thus, it is necessary to generalize the monochromatic quantities and equations introduced so far to spectrally filtered or broad-band quantities. For a band ranging from wavelengths λ_1 to λ_2 , the radiance contained within the band is defined as

$$I \equiv \int_{\lambda_1}^{\lambda_2} I_\lambda d\lambda \quad (2.16)$$

The *broad-band radiance* is obtained by setting the lower limit to zero and the upper limit to infinity.

Replacing the spectral radiance by the band radiance in Eq. 2.3, the irradiance for a wavelength interval is given by

$$F \equiv \int_{\lambda_1}^{\lambda_2} F_\lambda d\lambda. \quad (2.17)$$

It can be used to define the broad-band transmissivity, reflectivity and absorptivity (Eq. 2.8 to 2.9) in analogy to their monochromatic counterparts.

Many instruments measuring radiation show a significant wavelength dependence in their sensitivity. This dependence is described by the spectral response function ψ of an instrument, which is normalized to a maximum value of unity here. A measurement of radiances by such an instrument is then sensitive to the radiance I_ψ found by multiplying its response function with the spectral radiance

$$I_\psi = \int_0^\infty I(\lambda) \psi(\lambda) d\lambda. \quad (2.18)$$

Defining the spectral width Δ_ψ of the response function by

$$\Delta_\psi \equiv \int_0^\infty \psi(\lambda) d\lambda, \quad (2.19)$$

2.2 Atmospheric Radiative Transfer

a mean spectral radiance can be inferred

$$\bar{I}_\psi = \frac{I_\psi}{\Delta}. \quad (2.20)$$

If a representative wavelength can be determined within the wavelength interval, radiances obtained from monochromatic radiative transfer calculations can be used instead of \bar{I}_ψ . Similar relations can be formulated to obtain response-weighted irradiances.

2.2.4 Radiative Transfer Equation

The interaction of radiation with a medium such as the atmosphere is formally described by the radiative transfer equation (RTE), given by

$$\mu \frac{dI_\lambda(\tau, \mu, \phi)}{d\tau} = -I_\lambda(\tau, \mu, \phi) + J_\lambda(\tau, \mu, \phi), \quad (2.21)$$

where I_λ is the spectral radiance, J_λ the source function, and μ and ϕ are the cosine of the zenith angle, and the azimuth angle, respectively. This form of the RTE uses the optical depth τ as the vertical coordinate, and is limited in applicability to plane-parallel atmospheres.

Generally, the components contributing to the source function are emission as well as scattering of both direct and diffuse radiation. For the shortwave region, emission within the atmosphere can be neglected as already mentioned. Then, the source function is given by

$$J_\lambda(\tau, \mu, \phi) = \frac{\omega}{4\pi} \int_0^{2\pi} \int_{-1}^1 I_\lambda(\tau, \mu', \phi') \mathcal{P}_\lambda(\mu, \phi; \mu', \phi') d\mu' d\phi', \quad (2.22)$$

where ω is the single-scattering albedo, which specifies the probability of a photon to be scattered in case of an interaction with the atmosphere. These two equations specify the physical constraints imposed on a radiance field by Maxwell's equations for plane-parallel media without internal sources of radiation.

Numerical Solution of the RTE

For an atmosphere with known optical properties and given boundary conditions, the desired radiative quantities can be calculated from the corresponding solution of Eq. 2.21. Hence, a way of solving this equation is required for given optical properties and boundary conditions. Unfortunately, there exists no general analytical solution to the RTE. Several techniques have been developed to find numerical approximations. A short summary of the Discrete-Ordinates method used for the calculations presented within this thesis is given here.

General Simplifications First, the direct beam irradiance F_{DIR} is calculated for the complete atmosphere. The irradiance of the direct beam is reduced according to the Law of Lambert-Beer

$$F_{DIR}(z) = F_\odot e^{-\mu_0 \tau(z)}, \quad (2.23)$$

a solution to the RTE in the absence of scattering and internal radiation sources. Here, the solar constant F_{\odot} , the irradiance on a surface normal to the beam direction at the TOA, has been used. A pseudo source term is then added to the RTE, which accounts for the scattering of the direct beam irradiance at a given height. This allows the separate solution of the RTE for the direct and the diffuse radiance fields.

Discrete Ordinates Method The Discrete Ordinates method for solving the RTE has been proposed by Chandrasekhar (1960). The model atmosphere is subdivided into layers having homogeneous optical properties.

A Fourier expansion of the azimuthal dependence of the diffuse radiance field and an expansion of the phase function in Legendre polynomials results in an infinite series of equations that are independent of the azimuth angle. The series is truncated considering enough equations to achieve the desired accuracy.

Choosing a number of representative zenith angles according to a Gaussian quadrature with corresponding weights, the zenith angle dependence of each equation can be separated into a set of non-homogeneous differential equations. The number of zenith angles is called the number of streams, and is often chosen equal to the number of equations used for describing the azimuthal dependence.

The solution for each atmospheric layer is a linear combination of the homogeneous solutions of these equations, plus a particular solution for the source term. The linear coefficients for a specific problem are fixed by the boundary conditions at the TOA and the surface, as well as the requirement of continuity of the radiance field at the layer boundaries.

For the calculation of radiative quantities within this thesis, DISORT has been used, an implementation of the discrete ordinates method described in and written by Stamnes et al. (1988). Its algorithms are based on detailed analyses of the mathematical properties of the problem to ensure numerical stability and computational efficiency. It is widely used in the scientific community and has been extensively tested against other models.

2.2.5 Optical Properties of Atmospheric Constituents

While discussing the solution of the RTE, the knowledge of the optical properties of the atmosphere has been assumed. This section shows how these properties can be derived for a known atmospheric composition. Of relevance for solar radiative transfer are scattering and absorption by gases, as well as cloud and aerosol particles.

Clear Air or Rayleigh Scattering

Rayleigh scattering describes the interaction of an electromagnetic wave with a polarizable scatterer, if the interaction can be reduced to the effects of the induced dipole moment of the scatterer's electron hull on the photon. This assumption is valid for particles much smaller than the wavelength of the radiation. Hence, it applies to the treatment of scattering of solar radiation by air molecules. Its functional form is given

2.2 Atmospheric Radiative Transfer

by

$$I_{\lambda}(\theta) = I_{0,\lambda} \frac{8\pi^4 \eta \alpha}{\lambda^4 r^2} (1 + \cos^2 \theta), \quad (2.24)$$

where $I_{0,\lambda}$ is the incident intensity, I_{λ} the scattered intensity, η and r the number density and radius of the scatterer, and α the polarizability of the molecule. For the thesis, the formulation of Nicolet (1984) is used to calculate the Rayleigh scattering cross section k_{RAY} for dry air

$$k_{RAY}(\lambda) = \frac{4.02 \times 10^{-28}}{\lambda^{4+\delta}}, \quad (2.25)$$

where λ has to be specified in units of μm and k_R is obtained in units of cm^2 . The correction term δ is given by $0.398 \lambda + \frac{0.0943}{\lambda} - 0.323$ for wavelengths less than $0.55 \mu\text{m}$ and is fixed to a value of 0.04 for larger wavelengths.

Gaseous Absorption

The total energy of a molecule is given as the sum of electronic energy, vibrational energy, rotational energy and translational energy. All but the last contribution are quantized.

Absorption of radiation by molecules is caused by transitions between different molecular energy states. The radiative energy has to closely match the energy difference of initial and final states for a transition to occur. The term *closely match* is quantified by the line shape, which describes the probability of absorption as function of distance from the central wavelength of a line. A lower limit on the width of a line is set by Heisenberg's uncertainty principle. For typical atmospheric conditions, Doppler- and collision broadening are the main processes determining the width and functional form of absorption lines.

Line-by-Line Methods For monochromatic radiation, the combined transmissivity of two molecular species is the product of the individual transmissivities. This multiplication property also holds for spectral intervals, as long as the absorption cross-section is constant over the interval. Line-by-line radiative transfer schemes make use of this fact by choosing a high-enough spectral resolution to ensure that the condition is met with sufficient accuracy. The required optical properties can be derived from databases such as HITRAN (see Rothman et al., 1998), which tabulate parameters describing the line strengths and shapes for relevant molecular species found in the atmosphere. To obtain results for broad spectral regions, calculations for a large number of spectral intervals are required, making this technique mainly suitable for reference calculations. For most practical applications, line-by-line calculations are computationally too expensive.

Correlated-k Distribution Method Several methods have been developed to determine gaseous absorption properties representative for larger wavelength intervals. Generally, these intervals are chosen in such a manner that the solar irradiance can be considered constant throughout the wavelength interval, while allowing for variations in the absorption cross-section. The correlated-k distribution method is one technique able to obtain accurate results under these conditions, as shown by Fu and Liou (1992).

Assuming a wavelength independent spectral solar irradiance $F_{\odot,\lambda}$, the band-averaged direct beam transmittance \mathcal{T}_{DIR} for a single absorber and a homogeneous path can be expressed as function of absorber concentration η and absorption cross-section k using

$$\mathcal{T}_{DIR}(\eta) \equiv \frac{\int_{\lambda_1}^{\lambda_2} F_{\odot}(\lambda) e^{-k(\lambda)\eta} d\lambda}{\int_{\lambda_1}^{\lambda_2} F_{\odot}(\lambda) d\lambda} = \frac{1}{\Delta\lambda} \int_{\lambda_1}^{\lambda_2} e^{-k(\lambda)\eta} d\lambda. \quad (2.26)$$

Defining a normalized probability function f for the occurrence of a fixed value of k and requiring $\int_0^{\infty} f(k) dk = 1$, we can then rewrite the transmissivity as

$$\mathcal{T}_{DIR}(\eta) = \int_0^{\infty} f(k) e^{-k\eta} dk, \quad (2.27)$$

thereby losing any wavelength dependence. Using the functional form of f , the cumulative probability $g(k) = \int_0^k f(k) dk$ can be calculated and its inverse function $k(g)$ inferred. This inverse exists, because the cumulative probability is a monotonous function. Rewriting the integral expression of the previous equation making use of the inverse, the integral can be evaluated by a Gaussian quadrature to obtain

$$\mathcal{T}_{DIR}(\eta) = \int_0^1 e^{-k(g)\eta} dg \approx \sum_{j=1}^n a_j e^{-k(g_j)\eta}, \quad (2.28)$$

where n is the number of quadrature points, a_j are the Gaussian weights and $k(g_i)$ is the cross-section at the quadrature point g_i . Up to the integral in Eq. 2.28, the treatment is exact. This reformulation of the transmissivity is called the k-distribution method. For an accurate numerical evaluation of the integral, fewer quadrature points are required than for Eq. 2.27, as the cumulative probability g is generally smoother than f due to its monotonous behavior.

A homogeneous optical path has been assumed up to here. The method can be extended to the inhomogeneous case by requiring that the absorption cross-section resides in the same Δg interval for the combined layer properties, thus is correlated with the value of g for different temperatures and pressures.

Then, the combined transmissivity of two layers can be written as

$$\mathcal{T}_{DIR} = \sum_{j=1}^n a_j e^{-(k_{1,j}\eta_1 + k_{2,j}\eta_2)}, \quad (2.29)$$

which is referred to as the correlated-k distribution method in the literature.

Above assumption is fulfilled exactly for both weak and strong lines as well as single non-overlapping absorption lines. For normal atmospheric conditions, it provides accurate results with maximum expected errors of about one percent (Fu and Liou, 1992).

For the radiative transfer calculations done within the scope of this thesis, two implementations of the correlated-k distribution method are used, unless specified otherwise. For calculations covering the total solar spectral region, the scheme of Kato et al. (1999) has been used, which splits the wavelength range from 0.241 μm to 4.6 μm

2.2 Atmospheric Radiative Transfer

into 32 bands. It takes into account the absorption of oxygen, carbon dioxide, ozone and water vapor including continuum absorption using the treatment of Clough et al. (1989). To simulate narrow-band radiances as measured by the AVHRR instrument on board the NOAA series of satellites, the Kratz (1995) scheme has been applied. Both schemes are based on absorption properties as specified in the 1992 release of the HITRAN database (Rothman et al., 1992).

Clouds and Aerosols

Apart from air molecules, cloud and aerosol particles interact with shortwave radiation. Both aerosols and the water droplets of clouds can be approximated as homogeneous spherical particles with good accuracy. Hence, their optical properties can be inferred by Mie theory, which solves Maxwell's equations for this particular problem.

There is no such solution for ice particles, due to their complex and diverse geometrical shapes. As they are larger than the dominant solar wavelengths, ray tracing, a stochastic approach based on the geometrical optics approximation, can be used to estimate their optical properties.

Mie Theory Mie theory (Mie, 1908) describes the solution of Maxwell's equations for the case of an incident plane wave that scatters off a homogeneous spherical particle. Its equations are obtained by expanding the outgoing radiation field in a series of spherical harmonics and studying the behavior of this solution in the far field limit. The solution does not depend on the absolute sizes of the wavelength λ and the radius r of particle, but only on the size parameter $\chi \equiv \frac{2\pi r}{\lambda}$, as well as the change in complex index of refraction between the particle and the surrounding medium. The real part of the refractive index describes the change in phase velocity for photons propagating within the particle, and the imaginary part describes the probability of absorption. From the solution, the scattering and absorption cross-sections and the phase function can be derived. For particles large compared to the wavelength, such as cloud droplets, the extinction cross-section is approximately two times the area of its geometrical cross-section. A detailed discussion is given in van de Hulst (1957).

Ray Tracing For non-spherical particles such as ice crystals, there exists no general solution to Maxwell's equations similar to Mie theory. A common technique applied to such particles having a large size parameters χ is the *ray tracing* approach. The path of individual photons is simulated from entering the crystal until it exits again or is absorbed. Repeating this for a large number of photons and recording the angles between incoming and outgoing direction, together with the fraction of photons that are absorbed, a statistical estimate of the optical properties of the crystal can be found. The accuracy of this approach depends on the validity of the assumptions made by geometrical optics (see e.g. van de Hulst, 1957). Hence, its applicability is limited to large size parameters, a criterion which is fulfilled for solar wavelengths and the ice particles found in the atmosphere.

Ice crystals found in the atmosphere have a large variety of shapes and sizes (Pruppacher and Klett, 1978). Therefore, a particle type having representative optical proper-

ties needs to be chosen to obtain accurate results from the ray tracing calculations. In a comparison of the angular dependence of radiances expected from RTM calculations and the one measured from satellite by the POLDER instrument for a large number of scenes containing ice clouds, Knap et al. (2002) find rather good agreement for the *imperfect hexagonal ice crystals* proposed by Hess et al. (1998), which is significantly better than that of other commonly used crystal shapes. Their optical properties are therefore used for the representation of ice clouds in the radiative transfer calculations within this thesis.

Chapter 3

Measurements

In the previous chapter, the two radiative quantities central to this thesis have been introduced, together with the theoretical framework for their modeling.

A description of the instruments used for the measurements is given here. The first instrument is the pyranometer, which infers the downwelling global solar irradiance at the surface. The second instrument is the Advanced Very High Resolution Radiometer (AVHRR) flown on board the NOAA series of polar orbiting satellites. It estimates the radiance within several narrow spectral regions at a known viewing geometry.

Special focus is given to the analysis of error sources in the measurement process, to provide an estimate of the expected accuracy. Any comparison of model results and measurements is sensitive to instrumental errors. Thus, care must be taken to separate differences originating from instrumental errors and model deficiencies.

3.1 Pyranometer

The Koninklijk Nederlands Meteorologisch Instituut (KNMI) maintains an operational network of 32 stations measuring the global broad-band solar irradiance at the surface. A list of the station names, together with their WMO identification numbers, their coordinates and a map showing their geographic distribution can be found in Appendix A. Data loggers record the mean, minimum and maximum level of irradiance measured by the instruments during 10 minute intervals. The instruments used are pyranometers of type CM 11 built by *Kipp en Zonen*.

3.1.1 Principle of Operation and Instrument Description

The thermoelectric pyranometer is an instrument capable of an accurate measurement of broad-band hemispherical irradiances in the solar spectral region. Its main application is the measurement of the downwelling solar irradiance at meteorological stations. It can measure either the global or the diffuse irradiance. For the latter, the pyranometer is operated in shaded conditions, where the direct beam of the sun is blocked by a shadow disk.

The pyranometer's operational principle is based on the effect of differential heating of an absorbing detector exposed to shortwave radiation, relative to a temperature

3.1 Pyranometer

reference whose thermal state is not altered by radiation. The resulting temperature difference is used to deduce the level of incident irradiance.

In case of the CM11, a black painted ceramic disk is located in the center of the instrument and acts as absorber. The disk is in good thermal contact with the pyranometer body, which serves as heatsink and temperature reference. 100 thermocouples produce a voltage proportional to the temperature gradient from the center of the disk to the instrument's body. They are applied in thin-film technique and are arranged in a rotationally symmetric manner to minimize differences in the directional sensitivity. Two hemispherical glass domes filter out longwave radiation and shield the instrument from environmental influences. They transmit radiation in the spectral range between 0.3 and 2.8 μm . More details about the CM11 are given in Kipp en Zonen (1992).

The response of a pyranometer to incident irradiance is modeled by a linear equation, which links the level of irradiance F to the output voltage U . This equation contains two parameters, the instrumental sensitivity κ and a possible offset F_{ZO}

$$F = \kappa U + F_{ZO}. \quad (3.1)$$

The accuracy of the measurements is then determined by the accurate knowledge and the temporal stability of both parameters, as long as the instrumental response fulfills the assumed model sufficiently well.

3.1.2 Measurement Accuracy

The CM11 is classified as a *secondary standard* instrument in accordance with ISO 9060 (ISO, 1996) and the *WMO Guide to Meteorological Instruments and Methods of Observation* (WMO, 1996), which define mandatory criteria to ensure a high degree of accuracy. Three and two percent are the maximum expected errors for hourly and daily sums, respectively, if the instruments are operated under optimal conditions.

Several parameters have an influence on the error characteristics of an instrumental dataset, such as the length of the measurement period, and the number and maintenance of the instruments. For this thesis, data recorded by 32 different stations starting at the beginning of the year 1995 until the end of the year 2000 are used, including data of many different instruments. The KNMI operates the pyranometers without ventilation. Human inspections and cleaning of the domes are done at maximum intervals of once per year, or as soon as inconsistencies show up in the collected data. Each instrument is calibrated biannually. The instruments installed at a particular site are regularly interchanged as a result. These operating conditions are less than optimal due to the low level of maintenance and can affect the reliability of the dataset. Thus, rigorous quality checks of the measurements are necessary.

The different error sources are described in the following paragraphs. To assess their impact on the dataset, relative errors, which change the sensitivity, are distinguished from absolute errors, which cause uncertainties with a magnitude independent of the measured signal. Also, their statistical properties are analyzed. Random errors vary significantly over the measurement period, requiring a Gaussian error treatment. Systematic errors have an unknown, but stable impact on the dataset. The estimated magnitude of each error is listed in brackets for the CM11 instrument based on the specifications reported in Kipp en Zonen (1992).

Uncertainties in Sensitivity

Changes in the instrumental sensitivity κ are called *non-linearity* (0.6%), if they depend on the magnitude of the input signal, and *non-stability* (0.5% per year), if they result from changes in the instrumental characteristics occurring over longer time periods. The sensitivity of the pyranometer is also altered by changes in ambient temperature (1.0% for normal field conditions). All three errors are random for the considered dataset, as their magnitude varies for measurements obtained by several instruments throughout multiple years.

The *directional response* describes changes in sensitivity depending on the direction of incidence for a collimated beam of radiation (1.2%). These variations are caused by imperfections in the glass domes and the absorbing paint on the ceramic disk. In principle, a correction would be possible, if the ratio of diffuse to direct irradiance and the response function of the instrument were known. As it varies for different instruments, the impact on the considered data is considered as random. In cloudy conditions, this error can be neglected due to the rather isotropic distribution of radiation. For cloudless skies, model calculations as described in Ch. 4 show that the direct component contributes about 60 to 80% of the global irradiance during typical conditions in the Netherlands. Thus, a value of 1.0% is assumed as its value for the measurements of the global irradiance during cloud-free conditions.

Apart from the random error, a systematic dependence of the response on the solar zenith angle, the *cosine response*, is expected for each type of instrument. It is caused by two competing effects, a reduced overall transmissivity of the glass dome and an increased reflection within the dome, as the solar zenith angle increases. The magnitude of both effects depend on the details of construction, and are not known for the CM 11 instruments.

Spectral sensitivity is a result of both variations in the transmissivity of the glass dome, and the remaining reflectivity of the absorbing paint on the detector throughout the solar spectral region. Its magnitude is about 1 percent for monochromatic radiation. The effect is much smaller for measurements of solar radiation, because the energy is distributed over a wide range of frequencies for both clear-sky and cloudy conditions. A second point to consider is the limited spectral range transmitted by the glass dome (0.3 to 2.8 μm). Nevertheless, the instrument is calibrated to output the total amount of incident solar irradiance. Thus, a systematic error can result, if the fraction of radiation within that spectral window to the total incident solar radiation changes significantly from calibration to measurement conditions. Both effects are analyzed in more detail in Wardle et al. (1996) and found to be negligible for ordinary field conditions.

As the instruments are operated without regular cleaning in the field, the outer glass dome gets contaminated with dust and dirt over time, reducing its transmissivity and resulting in a systematic underestimate of the measured irradiance. Kuik (1997) reports an increase of about 0.5% in the output signal after cleaning a pyranometer which had been deployed in the field for half a year at De Bilt, the Netherlands. As the maximum interval between inspection and cleaning of the instrument is one year, this value is probably a reasonable estimate of the mean effect of contamination on irradiances recorded by KNMI's measurement network. This value depends on several unknown parameters such as precipitation and the deposition rate of dust. Therefore, an addi-

3.1 Pyranometer

tional uncertainty of 0.5% is used as upper and lower bounds to quantify the mean effect of contamination.

Thermal Offset

The measurement principle of the pyranometer relies on an equilibrium thermal state of the detector, which is governed by heating through shortwave absorption and cooling through heat conduction to the heatsink. Any unaccounted term in the energy balance of the instrument will result in an offset voltage, if it affects heatsink and detector differently.

Two different reasons exist for a thermal offset. The first originates from changes in ambient temperature, because the heat capacities of detector and instrumental body are different. Its magnitude can be measured experimentally, and is found to be 2.2 Wm^{-2} for the CM11 as result of a temperature change with a rate of 5 Kelvin per hour. Changes of this magnitude are typical for standard measurement conditions, and will have a random effect on the measurements.

A second mechanism leading to a thermal offset is caused by the difference in the temperature of the pyranometer and the radiative temperature of the sky. Due to this difference, which is typical for normal operation and especially large during clear-sky conditions, the glass domes are cooled, resulting in a net loss of longwave radiation from the detector to the glass domes and to the atmosphere. This loss of energy is proportional to the difference of the fourth powers of the temperatures of detector and dome (Bush et al., 2000). Applying this relation to measurements of both temperatures, they show that this thermal offset can reach maximum values as high as 30 Wm^{-2} . Typically, it causes an underestimate of the measured irradiance in the order of 5 Wm^{-2} to 20 Wm^{-2} for shaded operation during clear-sky day conditions. These values are significantly larger than previous estimates, which were based on observed night-time offsets and their correlation with the net longwave radiation. Using this technique, Wardle et al. (1996) report values of only up to 7 Wm^{-2} .

The actual magnitude of the thermal offset depends on several parameters, such as instrumental construction, wind speed and ventilation, instrumental temperature, and the net longwave radiation balance (Dutton et al., 2001). Also, Bush et al. (2000) report a strong reduction of the thermal offset for pyranometers after unshading them. The reason for this reduction is still uncertain, but a likely cause seems to be heating of the dome by the direct solar beam which could compensate part of the longwave loss of energy. The glass domes of commonly used pyranometers, such as the Kipp en Zonen CM11 and the Eppley Precision Spectral Pyranometer (PSP), only transmit shortwave radiation in the spectral range from $0.3 \mu\text{m}$ to $2.8 \mu\text{m}$. The remaining part of the solar irradiance is absorbed and heats the glass dome.

3.1.3 Pyranometer Calibration and its Accuracy

Pyranometers used in KNMI's measurement network are calibrated by an own indoor calibration laboratory, which relies on a reference instrument. This reference is calibrated annually at the World Radiation Center at Davos, Switzerland. Thus, an es-

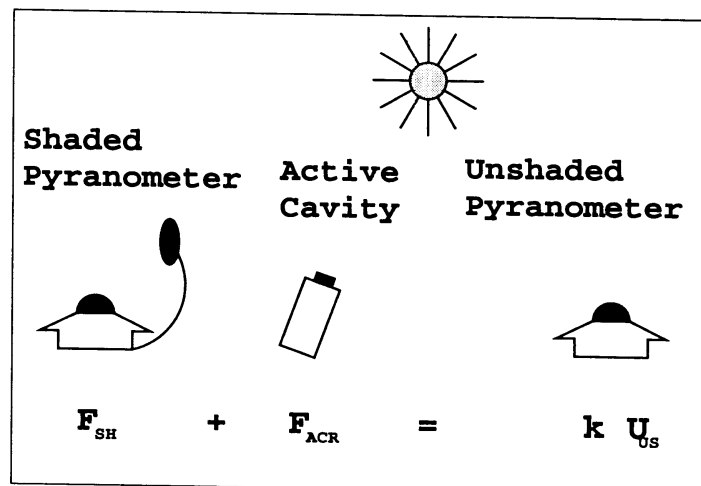


Figure 3.1: Setup used for pyranometer calibration according to the component summation method. An ACR measures the direct irradiance and a shaded pyranometer the diffuse irradiance. Their measurements are summed to provide a reference value of the global irradiance. The sensitivity of the unshaded pyranometer is chosen as the factor of proportionality linking the output voltage to this reference irradiance.

estimate of the uncertainty of the calibration process has to combine the error sources inherent in both calibration procedures.

Indoor Calibration at the KNMI

KNMI's indoor calibration laboratory uses a 500 W halogen lamp as irradiance source. Two pyranometers of identical type are operated on a rotating disk, one being the accurately calibrated reference. The sensitivity of the instrument to be calibrated is then adjusted to match the output of the reference. Uncertainties for translating the calibration are estimated to be about 0.5%. This uncertainty results from the possible existence of systematic differences between individual instruments of the same type. As the reference instrument is not exchanged, this error can have a systematic impact on the calibration results.

Pyranometer Calibration at the World Radiation Center

The reference instrument used by the calibration laboratory of the KNMI is sent to the World Radiation Center (WRC) at Davos, Switzerland, once every year for recalibration. There, the *component summation method* (CSM) is used to obtain a highly accurate calibration. Its principle is described in detail in WMO (1996), and is based on two fundamental assumptions. Firstly, the output voltage U of the pyranometer is linked to the incident shortwave irradiance F by a linear relationship according to $F = \kappa U$, neglecting the offset in Eq. 3.1. Then, calibration is equivalent to the determination of the sensitivity κ of the instrument. Secondly, closure of three independent measurements of the direct (F_{DIR}), diffuse (F_{DIF}) and global (F_{GLOB}) irradiance is

3.1 Pyranometer

assumed, expressed by

$$F_{GLOB} = F_{DIR} + F_{DIF}. \quad (3.2)$$

In the CSM, the pyranometer to be calibrated is operated unshaded to obtain a voltage proportional to the global irradiance. Reference measurements of the direct and diffuse components are required to determine the sensitivity. At the WRC, the direct irradiance is measured by an active cavity radiometer (ACR) of the World Radiometric Reference (see Fröhlich, 1991) and the diffuse irradiance is measured by the WRC standard pyranometer operating in shaded condition (F_{SH}).

The sensitivity of the unshaded instrument is then obtained according to

$$\kappa = \frac{F_{ACR} + F_{SH}}{U_{US}}, \quad (3.3)$$

where U_{US} is its output voltage.

The accuracy of the ACR is determined to be 0.1% relative to other instruments of the World Radiometric Reference, and estimated to be better than 0.3% in absolute sense, due to the lack of any accurately known reference (Fröhlich, 1991). Hence, the significantly larger pyranometer uncertainties dominate the total error during the calibration process. In the absence of any significant absolute error, uncertainties in the reference measurement of the shaded instrument will also have little impact, as the contribution of the diffuse irradiance to the global irradiance is small for typical clear-sky conditions at Davos. Thus, the main source of error originates from the pyranometer to be calibrated, or from potential absolute errors of the shaded reference pyranometer.

The CSM achieves a reproducibility in the order of a few tenths of a percent. Taking all possible uncertainties into account, the overall accuracy of the calibration procedure is believed to be about 0.5% (Wardle et al., 1996).

Impact of the Thermal Offset on Calibration

The thermal offset violates the assumption of an offset-free linear response made in Eq. 3.1, which is fundamental to pyranometer calibration. Here, an analysis is presented to quantify possible errors due to this violation.

For simplicity, any error in the ACR measurement is neglected, and a perfectly linear response for both pyranometers assumed, in combination with a correct calibration of the shaded reference pyranometer. Both shaded and unshaded pyranometers are affected by a thermal offset, which are allowed to have different magnitudes. Then, the actual global (F_{GLOB}) and diffuse irradiances (F_{DIF}) are linked to the unshaded and shaded irradiances reported by the instruments, F_{US} and F_{SH} , by

$$\begin{aligned} F_{US} &= F_{GLOB} - F_{TO,US} \\ F_{SH} &= F_{DIF} - F_{TO,SH}, \end{aligned} \quad (3.4)$$

where $F_{TO,SH}$ and $F_{TO,US}$ are the thermal offsets of the shaded and unshaded instruments.

To study the impact of the thermal offset, we consider the dependence of the reported output of the instruments on the true incident irradiance, as illustrated in Fig. 3.2. The

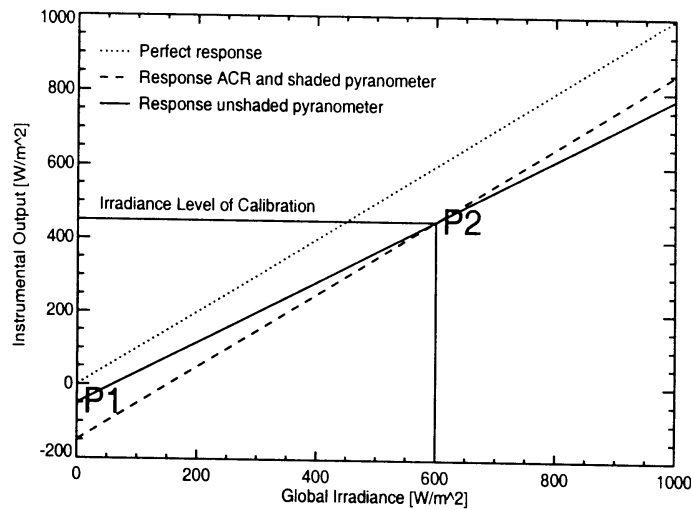


Figure 3.2: Response of an unshaded pyranometer (solid line), as determined by the CSM calibration, if the thermal offset of pyranometers is not considered. Desired would be a perfect response of unity (dotted line). The combined outputs of an ACR and a shaded reference pyranometer are used as reference (dashed line). For illustration purposes, unrealistically large thermal offset values of 150 Wm^{-2} for the shaded and 50 Wm^{-2} for the unshaded instrument have been used

true irradiance is shown on the abscissa, and the measured instrumental output is shown on the ordinate. The slope of the response of a correctly calibrated linear instrument is unity. A calibration error will show up as a deviation of the slope from unity. Thus, the slope of the response of the reference irradiance obtained from the sum of ACR and shaded pyranometer has to be one, due to the assumption of correct sensitivities of both measurements.

Both the response of the reference, composed of the outputs of ACR and shaded pyranometer, as well as the pyranometer to be calibrated, are equal to the value of the thermal offset at zero irradiance. Hence, one point P1 ($0, -F_{TO,US}$) of the response of the instrument to be calibrated is already known.

If the sensitivity of the unshaded pyranometer is inferred at a given level of global irradiance F_{GLOB} during calibration, the outputs of the reference and the unshaded pyranometer are assumed to be equal. This will occur at the point P2, specified by the coordinates $(F_{GLOB}, F_{GLOB} - F_{TO,SH})$. Two details should be noted here. The thermal offsets shown are the ones at the moment of calibration, and might be different during operating conditions. Also, the choice of a smaller thermal offset for the shaded than the unshaded instrument, as shown in Fig. 3.2, is arbitrary at this point, and is responsible for the underestimate of the sensitivity. A larger thermal offset of the unshaded than the shaded reference instrument will lead to an overestimate. No bias in calibration will occur if both offsets are equal. This can be visualized by varying P1 in the figure.

The calibration error shows up as deviation of the slope κ' of the response of the

3.1 Pyranometer

unshaded pyranometer from unity. It can be determined using the two points P1 and P2 according to

$$\begin{aligned}\kappa' &= \frac{y_2 - y_1}{x_2 - x_1} = \frac{F_{GLOB} - (F_{TO,SH} - F_{TO,US})}{F_{GLOB}} \\ &= 1 - \frac{F_{TO,SH} - F_{TO,US}}{F_{GLOB}}.\end{aligned}\tag{3.5}$$

The assumptions made in this derivation have been simplified for clarity, as pyranometers are calibrated over long periods of time using different levels of irradiance and solar zenith angles. Thus, the instantaneous values have to be averaged to find representative mean values, which makes the mathematical analysis more complicated. Still, the underlying mechanism causing the calibration bias will still be present.

Eq. 3.5 shows that the component summation method of calibration will lead to erroneous sensitivities, if significant differences in the size of thermal offsets for the reference pyranometer and the instrument to be calibrated exist. Bush et al. (2000) report such differences for Eppley PSP instruments operating without ventilation in shaded and unshaded conditions, to our knowledge the only investigation that has actually measured this difference.

On the other hand, Cess et al. (2000) observe large inconsistencies in a one-year dataset of measured direct, diffuse and global irradiances collected as part of the Atmospheric Radiation Measurements (ARM) program. They attribute these to differences in the thermal offset of pyranometers operating in shaded and unshaded conditions, in the absence of any other known error source of the observed size. If their conclusion is correct, the difference also has a strong diurnal cycle. Hence, the difference of thermal offsets would correlate with the amount of incident irradiance, a fact which complicates the analysis. Thus, only a rough estimate of the magnitude of the resulting calibration uncertainty can be given without further research.

For this estimate, the magnitude of the thermal offset for shaded and unshaded operation as determined by Bush et al. (2000) and listed in their Table 2 are used. From the temperatures of the dome and the detector, they infer the changes in thermal offset after shading a PSP on 5 clear-sky days. The measured changes are 6.1, 8.5 and 15.2 Wm⁻² for the minimum, mean and maximum difference, with the shaded offset always being larger. As they do not list the level of irradiance at the moment of shading, the mean level of irradiance (610 Wm⁻²) during the last calibration of the reference pyranometer of the KNMI is used (World Radiation Center, 2000). This step introduces a significant uncertainty in the estimate, due to a possible correlation of the difference in thermal offset with the amount of incident irradiance. Employing Eq. 3.5, this mechanism would result in a mean underestimate of the calibration constant κ by 1.4%, with a range from 1 up to 2.5%.

The calibration bias proposed here has not been considered in previous estimates of the pyranometer uncertainty. Due to its hypothetical nature, it will not be included in the estimate of the total uncertainty in pyranometer measurements. Nevertheless, the possible impact of this bias is discussed in the comparison of pyranometer data to model output and satellite measurements later in this thesis. A detailed experimental investigation is required to confirm or reject its relevance. If it is confirmed, an exact

Relative Errors	Stability	Uncertainty [%]
non-linearity	random	± 0.6
temperature sensitivity	random	± 1.0
non-stability (per year)	random.	± 0.5
directional response	random	± 1.0
contamination	systematic	-0.5 ± 0.5
calibration	systematic,random	$\pm 0.5, \pm 0.5$
combined error clear-sky	random	± 1.7
combined error cloudy-sky	random	± 1.4
combined error all-sky	systematic	-0.5 ± 1.0
Absolute Errors		Uncertainty [Wm^{-2}]
temperature changes (5K/hr)	random	± 2.2
thermal offset, clear-sky	systematic	-10 ± 7
thermal offset, cloudy-sky	systematic	-4 ± 3
combined error all-sky	random	± 2.2
combined error clear-sky	systematic	-10 ± 5
combined error cloudy-sky	systematic	-4 ± 3

Table 3.1: Overview of the individual and total measurement uncertainties for an unshaded pyranometer operating in clear-sky or cloudy conditions. Error sources are classified according to their impact on the considered dataset as relative or absolute errors, and as systematic or random errors.

quantification of the resulting bias is desirable to account for its effects on historical records of pyranometer measurements. Such a correction probably also has to increase the estimates of instrumental uncertainty, due to the complexity of the factors causing the thermal offset.

3.1.4 Combined Uncertainty of Measured Irradiances

The error sources described in the previous discussion are summarized in Tab. 3.1, differentiating between relative and absolute errors, as well as systematic and random errors. Also, each class of errors is summed to a combined total. Gaussian error propagation has been assumed for random errors, and systematic errors have been added using their absolute values. For a given clear-sky or cloudy measured irradiance, a final estimate has to convert the relative errors to an absolute value using the magnitude of the measured irradiance.

The combined error estimate in Tab. 3.1 shows that the required accuracy for a secondary standard (3% for hourly sums), as demanded by WMO (1996) is only met by the CM11 instrument, if the thermal offset is not considered. The existence of the thermal offset, and the possibility of the calibration bias outlined in the previous section, can lead to a significantly larger measurement uncertainty. As both effects have a systematic impact on the instrumental output and do not increase the variability, their presence cannot be detected by a purely statistical analysis of the inferred irradiances.

3.2 Advanced Very High Resolution Radiometer

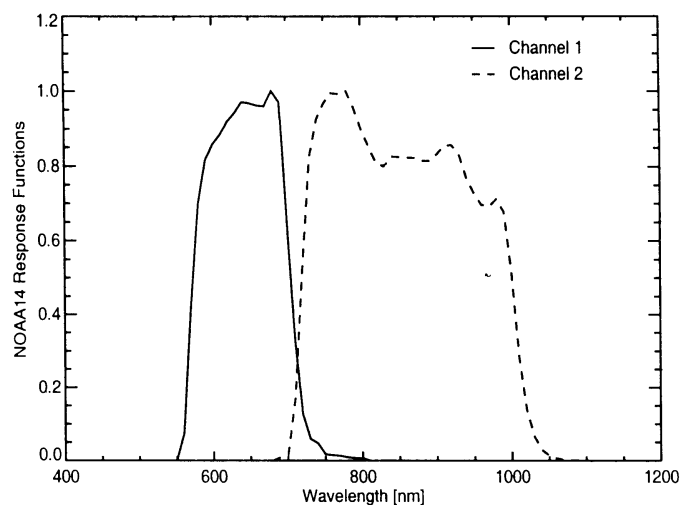


Figure 3.3: Spectral response function of the $0.65 \mu\text{m}$ channel (solid line) and the $0.9 \mu\text{m}$ channel (dashed line) of the AVHRR instrument on board NOAA-14 .

3.2 Advanced Very High Resolution Radiometer

3.2.1 Principle of Operation and Instrument Description

The *Advanced Very High Resolution Radiometer* (AVHRR) instrument is an imaging radiometer operated on board of the NOAA series of polar-orbiting, sun-synchronous satellites, which orbit the Earth at a height of approximately 850 kilometers above the surface. Only data from NOAA-14 are considered for this thesis, which was launched on December 30th, 1994, to avoid inconsistencies in the data resulting from different instrumental calibrations.

The AVHRR has five channels measuring radiation in different wavelength regions. Two channels are sensitive to the visible ($0.6 \mu\text{m}$) and near-infrared ($0.9 \mu\text{m}$) part of the solar spectrum. Its scan mirror rotates at sixty revolutions per second, acquiring 2048 samples with a viewing angle range of ± 55 degrees and an instantaneous field of view of 0.7×10^{-3} degrees. This results in a nadir pixel resolution of $1.1 \times 1.1 \text{ km}^2$, and increases up to about $1.1 \times 2.5 \text{ km}^2$ at 55 degrees. Photo diodes made of silicon are used as detectors for the visible channels and have a radiometric resolution of 10 bit. They are sensitive to the incident radiance as filtered by the spectral response function shown in Fig. 3.3 for the visible channels. More information about the instrument can be found in the NOAA Polar Orbiter Data User's Guide (Kidwell, 1998).

3.2.2 Quantitative Analysis of AVHRR Data

The digital counts sampled from the output voltage of the instrument's detectors are linearly related to the radiative energy deposited in the detector. This energy is proportional to the response-weighted radiance, as given by Eq. 2.18. Hence, it depends on the functional form of the spectral response and can differ for instruments of the same

type. For a quantitative analysis of AVHRR images, it is therefore preferable to determine the mean spectral radiance \bar{I}_i for a given channel (see Eq. 2.20), where the index i indicates the channel number and replaces the response function ψ as subscript. It will be comparable for different instruments, as long as the spectral response is sufficiently similar.

Another convenient quantity to work with is the bidirectional reflectance at the TOA

$$r_i \equiv \pi \frac{I_i}{\mu_0 F_{\odot,i}} = \pi \frac{\bar{I}_i \Delta_i}{\mu_0 F_{\odot,i}}. \quad (3.6)$$

It is a sample of the BRDF (Eq. 2.12) at a particular viewing angle, and has been modified to use band-averaged quantities. It is the ratio of the measured radiance to the one expected for a perfectly reflecting Lambertian surface without atmospheric attenuation.

Following Rao and Chen (1996), the reflectance factor R_i is defined by

$$R_i \equiv \pi \frac{\bar{I}_i \Delta_i}{F_{\odot,i}(\delta_{ES} = 1AU)} = r_i \frac{\mu_0}{\delta_{ES}^2}, \quad (3.7)$$

where the sun - Earth distance δ_{ES} has to be specified in astronomical units (AU), and the time-dependent parts of the bidirectional reflectance are factored out. This definition is particularly useful for calibration studies. The instrumental response is always proportional to the reflectance factor for scenes with isotropic and time-independent bidirectional reflectance, because the dependences on the sun - Earth distance and the viewing zenith angle have been factored out.

The uncertainties inherent in AVHRR measurements are of very different nature compared to the pyranometer uncertainties. Environmental parameters have nearly no short-term impact on the sensitivity of the silicon detectors. On the other hand, cosmic radiation significantly reduces the sensitivity of the instrument over the lifespan of the satellite. Hence, the accuracy of AVHRR measurements is mainly determined by the accuracy of calibration.

3.2.3 AVHRR Calibration and its Uncertainty

The goal of calibration is the determination of the relation between the measured radiance I_i and the detector output counts C_i reported by the instrument. The conversion is assumed to be a linear function of the received radiance

$$I_i = \kappa_i(t)(C_i - C_{i,0}), \quad (3.8)$$

where $C_{i,0}$ is the detector zero offset and κ_i is the detector sensitivity. The offset $C_{i,0}$ is found by looking at deep space and is thus known rather accurately. It has a good temporal stability, as shown by Mitchell (2001). Hence, it will be neglected as a source of error. It has a value of 41 counts for both channels of the NOAA-14 AVHRR.

As the sensor is affected by cosmic radiation, its sensitivity κ decreases with age, and becomes a function of time t . Thus, the absolute value and the time-dependence of the sensitivity have to be inferred by calibration. As there is no on-board calibration source

3.2 Advanced Very High Resolution Radiometer

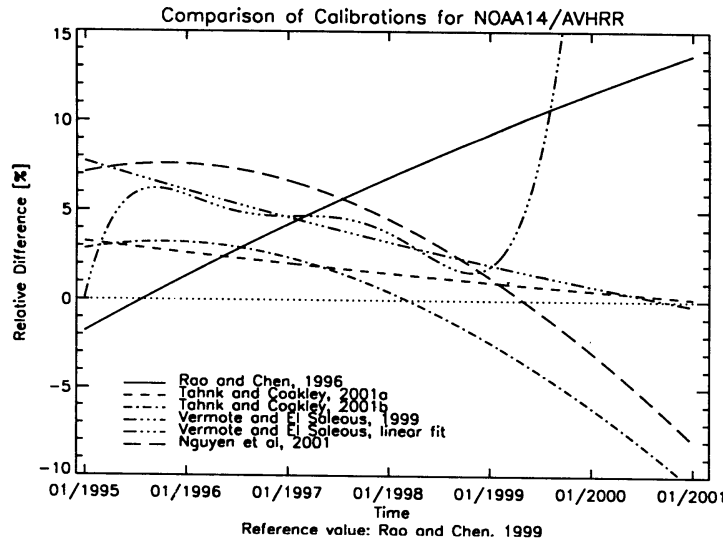


Figure 3.4: Relative difference of the instrumental response derived from the calibration-coefficients given by Rao and Chen (1996), Tahnk and Coakley (2001a), Tahnk and Coakley (2001b), Nguyen et al. (2001) and Vermote and El Saleous (1999) to the ones given in Rao and Chen (1999) as a function of time.

present for both visible channels, targets with stable and well-known reflectivity have to be used.

Instead of using a conversion to the response-weighted radiance as shown in Eq. 3.8, it is more practical to use a conversion to the reflectance factor R_i defined in Eq. 3.7, leading to a sensitivity κ' , which implicitly includes all quantities depending on the spectral response.

$$R_i = \kappa'_i(t)(C_i - C_{i,0}) = \frac{\Delta_i}{F_{i,0}(\delta_{ES} = 1AU)} \kappa_i(t)(C_i - C_{i,0}). \quad (3.9)$$

As the spectral response is only known from pre-launch measurements, its changes cannot be detected, but will be accounted for in changes of κ' .

Note that this is similar to the so-called albedo representation used in Rao and Chen (1996), but the sensitivity κ' in the definition presented here is independent of the sun - Earth distance at the time of the satellite measurement, as this dependence is included in the reflectance factor (Eq. 3.7).

Comparison of Different Calibration Studies

An overview of several calibration studies dealing with the NOAA-14 AVHRR instrument is given here. The time-dependence of the sensitivity κ' is accounted for by a polynomial of the form

$$\kappa'_i = \sum_{n=0}^N \kappa'_{i,n} d^n, \quad (3.10)$$

in all calibrations considered, where N is the maximum order of the polynomial and d is the number of days since the launch of the satellite. Then, a calibration can be specified by the coefficients $\kappa'_{i,n}$. The coefficients of the calibrations considered in the following are given in Appendix B.

Rao and Chen (1996) use parts of the Lybian desert as calibration targets with an assumed time-independent reflectivity of around 40 percent in both channels of the AVHRR, as known from aircraft measurements. From a linear fit to data obtained during the year 1995, they derive the sensor's sensitivity and its degradation. Using the same method, they update their findings in Rao and Chen (1999), including overpasses until the end of 1997.

For an independent study by Tahnk and Coakley (2001a), the ice sheets of Antarctica and Greenland are chosen as targets. A reflectivity of around 78 percent is used to fit data from January 1995 until November 1998, also assuming a linear degradation of the sensor. The estimate of the reflectivity of the ice sheets is based on a study of Loeb (1997) for an absolute calibration of the NOAA-12 satellite. Applying this calibration, they discover inconsistencies in the measured irradiances after 1998, and published a new set of coefficients (Tahnk and Coakley, 2001b), this time using overpasses up until January 2001 and assuming a second order polynomial for the functional form.

A different method for calibration has been developed by Vermote and Kaufman (1995). They use cloud-free ocean views and high-altitude optically-thick clouds and take into account water vapor and aerosol information for an absolute calibration. This method has been applied to NOAA-14 by Vermote and El Saleous (1999), using a polynomial of fifth degree. As the functional form clearly limits the applicability of the dataset to the fitting period, a linear regression has been applied to the sensitivity for the period from 1996 until the end of 1998, which allows an extrapolation of the calibration under the assumption of a further linear degradation.

In a study to intercalibrate different satellites to get comparable datasets, Nguyen et al. (2001) have determined the sensitivity of NOAA-14 using a second order polynomial. Due to the functional form, they recommend not to use the calibration past December 2001.

The plot in Fig. 3.4 shows the difference between the calibrations. As a reference, the calibration of Rao and Chen (1999) has been chosen, which is the calibration recommended by NOAA. As the sensitivity enters the calculation of the bidirectional reflectance linearly, the relative errors of sensitivity and calculated reflectances will be the same. Thus, the abscissa value represents the relative deviation of the calculated reflectance, if a given calibration is chosen instead of the recommended calibration by Rao and Chen (1999). All four newer calibrations suggest that the original results of Rao and Chen (1996) overestimate the degradation of the sensor. Possible explanations are the short time period used for fitting, or a fast degradation of the sensitivity directly after launch which slowed down within the first year. The other studies disagree significantly on the absolute value of the sensitivity, having highest values in Nguyen et al. (2001) and lowest values in Rao and Chen (1999). Differences between the calibrations are in the order of several percent, and are largest directly after launch.

As pointed out by Tahnk and Coakley (2001b), the sensor degradation seems to deviate from the linear form assumed in most calibrations early in the year 1999. This

3.2 Advanced Very High Resolution Radiometer

fact is clearly shown by the functional form of the two calibrations which take into account data past that time.

Choice of Calibration and Calibration Accuracy

Due to the lack of a stable on-board calibration source for the visible channels, the accuracy of calibration of the AVHRR is rather limited. In case of the instrument on board NOAA-14, part of the problem is probably amplified by rapid non-linear changes in the sensitivity of the sensor shortly after its launch and after the year 1998. For an accurate calibration, the functional form of the change in sensitivity needs to be known or assumed. The choice of a higher-order polynomial constrains the applicability of the calibration to the fitting period. While the second-order polynomial used by Nguyen et al. (2001) and Tahnk and Coakley (2001b) accounts better for the sensor's degradation, there seems little reason to expect an increase in sensitivity of the sensor, as predicted after mid-1999 for both the calibrations of Nguyen et al. (2001) and Tahnk and Coakley (2001b). Hence, extrapolation of both calibration results into the future will be problematic, making further monitoring of the sensor's sensitivity necessary.

For the analysis of the AVHRR data used in this thesis, the mean of the sensitivities obtained using the calibrations of Nguyen et al. (2001) and Tahnk and Coakley (2001b) are used. This choice is based on two reasons. Both calibrations consider scenes throughout the full period of measurements studied within this thesis. Also, there is a good agreement between this mean calibration and the calibration of Vermote and El Saleous (1999).

The overall accuracy of this calibration is estimated to be in the order of 5 percent, as this is the typical difference found between the individual calibrations presented here.

Chapter 4

Accuracy of Modeled Clear-Sky Global Surface Irradiances

4.1 Introduction

An accurate modeling of clear-sky conditions is of great importance for our understanding of the solar radiation budget. The variability of clouds and their optical properties introduces large uncertainties in the modeling of cloudy atmospheres. As a consequence, clear-sky observations provide the most reliable reference cases for evaluating the representation of the interaction of radiation with atmospheric aerosols and gases in radiative transfer models (RTMs). Errors in gas absorption and aerosol properties will propagate to cloudy situations and lead to biased estimates of the radiation budget (Bennartz and Lohmann, 2001). Furthermore, clear-sky conditions are often used as reference for an assessment of the effects of clouds on radiation (e.g. Ramanathan et al., 1989). While there is good agreement of measurements and models at the top of atmosphere, recent investigations have found large deviations for the incident solar radiation at the surface, which has led to an ongoing and controversial debate about the accuracy of current RTMs (e.g. Kato et al., 1997; Wild et al., 1998; Halthore et al., 1998) and the measurements (see Ch. 3).

Radiative closure of measurements and models is obtained, if radiative transfer calculations reproduce the measurements within the range of instrumental uncertainties. Clear-sky radiative closure studies are conducted to evaluate the accuracy of radiative transfer models and rely on a detailed characterization of the atmospheric profiles of gases and aerosols. A wealth of supplementary measurements are often made, which are not routinely available, and time consuming line-by-line codes are commonly used for the radiative transfer calculations.

In contrast, the aim of the present study is the understanding of the long-term mean and variability of the downwelling solar irradiance during clear-sky conditions and its representation in RTMs developed for applications requiring a higher numerical efficiency. Therefore, the investigation is based on solar irradiance measurements collected at 16 stations throughout the Netherlands during a 6-year time period. The large number of observations enables a statistically reliable assessment of difference between the measurement and model climatology. Important parameters such as e.g. aerosol pro-

4.2 Sensitivity of the Clear-Sky Shortwave Atmospheric Transmissivity

μ_0				0.2		0.5		0.8
Ref. CGSI [Wm^{-2}]				144.5		476.0		838.5
Ref. Transmissivity [%]				53.19		70.07		77.15
Sensitivity to Gaseous Profile								
IWV [kg m^{-2}]	16.4	± 7.5	-1.53	2.34	-1.53	2.23	-1.42	2.06
O ₃ [DU]	328.0	± 44.0	-0.22	0.29	-0.14	0.19	-0.11	0.14
p_{SFC} [hPa]	1013	± 30	-0.20	0.21	-0.20	0.20	-0.17	0.17
T [°C]		± 20	-0.16	0.18	-0.14	0.15	-0.12	0.13
Sensitivity to Aerosols								
τ_{500nm}	0.22	± 0.13	-3.85	5.11	-2.58	2.78	-1.54	1.53
r_{eff} [nm]	70	45, 100	-1.53	-2.22	-1.37	-0.89	-0.94	-0.38
ω		± 0.1	1.62	-2.3	1.16	-1.78	0.92	-1.44
g		± 0.1	1.60	-0.55	1.52	-0.63	0.96	-0.51
Other Sensitivities								
ω_{SFC} [%]	18.0	± 8.0	0.38	-0.38	0.54	-0.53	0.61	-0.60
F_{∞} [W m^{-2}]	1368	± 5.0	-0.19	0.19	-0.26	0.26	-0.28	0.28

Table 4.1: Reference values of total atmospheric transmissivity (in % of incoming irradiance) for solar radiation at three solar zenith angles and its sensitivity to variations in several input parameters to the radiative transfer calculations carried out with the LDK scheme.

properties have to be represented by climatological estimates similar to their treatment in GCMs. By analyzing the deviations of measurements and the results of radiative transfer calculations, the uncertainties inherent in this approach are quantified. Furthermore, the suitability of the irradiance data collected by KNMI's operational network for model evaluation is assessed.

This study is structured as follows: First, a mean atmospheric state and its uncertainties and expected variability are estimated, and the resulting sensitivity of the broad-band atmospheric transmissivity is calculated with a RTM. Then, the results of this model are compared to four additional radiative transfer schemes to evaluate the mutual agreement of different models for these calculations. Three of these models are detailed schemes specifically developed to achieve accurate results, while the last scheme is a highly parameterized RTM included in a GCM and is evaluated in an original and a modified version. Finally, differences between observations and model calculations are analyzed using the sensitivity analysis and the estimated instrumental uncertainties. Reasons for discrepancies are discussed, including uncertainties in water vapor absorption, aerosol properties and instrumental error sources.

4.2 Sensitivity of the Clear-Sky Shortwave Atmospheric Transmissivity

Calculations of the clear-sky radiation field and the clear-sky global surface irradiance (CGSI) require the optical properties of the atmosphere as input to radiative transfer models. Processes which have to be considered are the absorption and scattering caused by both air molecules and aerosol particles. Realistic input values for typical conditions in the Netherlands are estimated here and resulting mean values of the CGSI are calculated together with their sensitivity, based on both the uncertainties and natural variability of the input parameters.

Calculations are done with the libRadtran software package (Kylling and Mayer, 2001), using DISORT (Stamnes et al., 1988) with 8 streams for the solution of the RTE and accounting for gaseous absorption with the correlated-k scheme of Kato et al. (1999). This setup is referred to as the LDK scheme.

As the atmospheric transmissivity depends on the solar zenith angle, three values corresponding to a high, medium, and low sun above the horizon are chosen with $\mu_0 \in \{0.8, 0.5, 0.2\}$. Instead of using absolute values of CGSI, changes in the total atmospheric transmissivity are discussed, which is defined as $\mathcal{T}_{ATM} \equiv \frac{F_{GLOB}}{\mu_0 F_{\odot}}$. This is done in order to facilitate the comparison of the results obtained at different solar zenith angles, as the variability caused by changes of the incident TOA irradiance is removed, and only the effects of the different optical paths through the atmosphere remain.

4.2.1 Atmospheric Gases

The optical properties of the molecular atmosphere are derived from the Anderson et al. (1986) mid-latitude summer standard atmospheric profile. The optical depth for Rayleigh scattering and its phase function are obtained from the air density (see Ch. 2), and can be calculated with high accuracy (Teillet, 1990).

Gas absorption within the solar spectral region is mainly caused by water vapor, ozone, carbon dioxide and oxygen, which are the gaseous absorbers accounted for by the LDK scheme. Both water vapor and ozone are not well-mixed gases, but vary significantly in space and time. Thus, climatological mean column values for the Netherlands are used to scale the water vapor and ozone profiles of the standard atmosphere. The column water vapor is calculated from radiosonde soundings conducted 4 times a day at De Bilt, the Netherlands (52.10° N, 5.17° E). The ozone value is derived from measurements of a Brewer spectrometer also operated at De Bilt. Mean column amounts of $16.4 \pm 7.5 \text{ kg m}^{-2}$ for the integrated water vapor (IWV) and 328 ± 44 Dobson units (DU) for the ozone are found for the period from 1995 to 2000. The carbon dioxide concentration used is 365 ppm, a representative value for this period.

Temperature and pressure variations cause changes in molecular absorption due to their influence on the shape of absorption lines. Also, both the Rayleigh scattering optical depth and the total absorber amounts of well-mixed gases change proportionally to the surface pressure for hydrostatic atmospheres. Perturbations of $\pm 20^\circ \text{ C}$ and $\pm 30 \text{ hPa}$ have been applied to the temperature profile and the surface pressure to quantify the effects of temperature and pressure variability on the atmospheric transmissivity.

4.2 Sensitivity of the Clear-Sky Shortwave Atmospheric Transmissivity

The results listed in Tab. 4.1 show that changes in the water vapor column have by far the largest impact on the atmospheric transmissivity, leading to variations of several percent. Changes in temperature, pressure and ozone column only cause minor variations with maximum values of up to a quarter of a percent.

4.2.2 Aerosols

Aerosols significantly increase the scattering and absorption optical depth of clear-sky atmospheres. Their representation in radiative transfer models requires the extinction cross-section, single scattering albedo and phase function to be specified as a function of height and wavelength. In principle, these parameters can be determined from the size distribution and aerosol composition by the use of Mie calculations. In reality, both microphysical and optical properties of aerosols are difficult to measure and exhibit a strong spatial and temporal variability. As a consequence, the required input parameters for these calculations are often not available.

The knowledge of typical aerosol characteristics for the Netherlands is based on a limited number of investigations. Their results do not provide sufficient information to reliably infer all required optical properties on either a case-by-case basis or as a climatological mean. Nevertheless, a reasonable estimate is possible. Ten Brink et al. (1997) investigate the composition of aerosols obtained from measurements conducted close to Petten, the Netherlands, during 6 campaigns of 10 days each during the years 1992 to 1994. They identify a large fraction of the aerosol mass present over the Netherlands as water-soluble particles. Stammes and Henzing (2000) use multi-spectral measurements of a sun photometer during clear-sky conditions to infer aerosol optical properties at De Bilt from the year 1997 onwards. They find values of 0.22 ± 0.13 for the optical depth at 500 nm and 1.41 ± 0.45 for the Ångström exponent (Ångström, 1929), which is a measure for the decrease of aerosol optical depth with wavelength.

A log-normal size distribution with an effective radius of 70 nm and a variance of 1.8 has been used to derive optical properties from Mie calculations. The spectral dependence of the refractive index is chosen similar to a water soluble aerosol, but has been simplified somewhat. A constant value of 1.5 is used for the real part, and the characteristic increase from a value of 5×10^{-3} at $0.3 \mu\text{m}$ to a value of 1×10^{-2} at $0.8 \mu\text{m}$ is included for the imaginary part. For larger wavelengths, the imaginary part has been fixed to 1×10^{-2} , ignoring the variations in the infrared part of the spectrum, which cause significant differences to other aerosol types. This can be justified by the low aerosol optical depth in that part of the spectrum and the resulting minor influence on the broadband irradiance. The precise values of refractive indices used for each wavelength band of the LDK schemes are listed in Appendix C. This aerosol description reproduces the wavelength dependence found by Stammes and Henzing (2000) and quantified by the Ångström exponent, which justifies the choice of effective radius. Radii of 45 nm and 100 nm correspond to the upper and lower limits set by the standard deviation of the Ångström exponent. Thus, those radii have been used to infer the sensitivity of the CGSI to the aerosol particle radius given in Tab. 4.1.

For the vertical profile of aerosol extinction, the boundary layer profile corresponding to 22 km visibility and the background profiles above the boundary layer from Shettle

Surface Type	$\bar{\omega}_{srf}$	$\Delta\mathcal{T}_{ATM}$	$\Delta\mathcal{A}_{ATM}$	$\Delta\omega_{TOA}$
Grass (38)	23.8	0.86	-0.50	-0.16
Conifer (32)	23.2	0.79	-0.48	-0.13
Deciduous Tree (34)	25.8	0.89	-0.51	-0.15

Table 4.2: Changes in atmospheric transmissivity \mathcal{T}_{ATM} absorptivity \mathcal{A}_{ATM} , and planetary albedo ω_{TOA} (in % of incoming TOA irradiance) caused by the assumption of a spectrally invariant mean broad-band albedo for three types of vegetated surfaces (taken from MODTRAN, type number shown in brackets) at a solar zenith angle of 60° . Also shown is the broad-band surface albedo $\bar{\omega}_{srf}$ (in %) used as spectrally invariant value and calculated as ratio of modeled upwelling to downwelling irradiance at the surface.

and Fenn (1979) are selected. The profile is then scaled to the desired total optical depth at 500 nm wavelength. A Henyey-Greenstein phase function (Henyey and Greenstein, 1941) is used to describe the phase function of aerosol scattering, which provides sufficient accuracy for irradiance calculations (Boucher, 1998).

The model treatment of aerosols used here matches the observations well. Nevertheless, the available information is not sufficient to allow an unambiguous specification of aerosol properties, and systematic deviations from the true optical properties have to be expected. To estimate the resulting uncertainty for calculations of the CSGI, both the single scattering albedo and the asymmetry parameter have been varied by ± 0.1 .

The calculations listed in Tab. 4.1 clearly indicate that aerosol properties cause large variations in the clear-sky atmospheric transmissivity. These variations are largest for a sun low above the horizon, due to the longer path of photons through the atmosphere. However, the resulting absolute changes in CSGI are still smaller than for smaller solar zenith angles as a consequence of the lower amount of downwelling solar irradiance at the TOA. While the aerosol optical depth is the dominating parameter, other quantities such as the composition and size of the aerosol particles, and the resulting single scattering albedo and asymmetry parameter also cause significant variations in shortwave atmospheric transmissivity.

The results of this section show that aerosols cause large variations the clear-sky solar radiation budget. The information needed to model these variations in RTMs is currently neither available for individual cases nor mean clear-sky conditions for the Netherlands. Hence, aerosols introduce the largest source of uncertainty in model estimates of the solar radiation budget during clear-sky conditions at the moment.

4.2.3 Surface Albedo

A spectrally invariant surface albedo having values of $18 \pm 8\%$ has been assumed in the radiative transfer calculations shown in Tab. 4.1. This estimate is based on the ratio of the upwelling to the downwelling solar irradiance measured at the Cabauw and Garderen sites in the Netherlands. Albedos in the order of 12% are obtained for the forest surface present at Garderen, and in the range from 20 to 25% for the grassland present at Cabauw. These values are in agreement with values found in the literature

4.2 Sensitivity of the Clear-Sky Shortwave Atmospheric Transmissivity

(e.g. Bowker et al., 1985), and cause changes in total atmospheric transmissivity of about half a percent. Variations of the surface albedo due to changes in solar zenith angle and season are observed in the measurements, but have been neglected in this study, as the resulting influence on the atmospheric transmissivity will be significantly smaller than for aerosols and water vapor.

To investigate the effects of neglecting the wavelength dependence of the surface albedo, calculations using the measured spectral albedos for three types of vegetation included in version 4 of the MODTRAN RTM (Berk et al., 1989) have been carried out, as vegetated surfaces are typical for KNMI's measurement sites. First, a mean broad-band surface albedo $\bar{\omega}_{SFC}$ is obtained from the ratio of upwelling to the downwelling broad-band irradiance at the ground, which are calculated taking into account the spectral variation of the surface albedo. The changes in the atmospheric transmissivity \mathcal{T}_{ATM} , atmospheric absorptivity $\mathcal{A}_{ATM} \equiv \frac{F_{TOA}^- - F_{SFC}}{F_{TOA}^-}$ and planetary albedo $\omega_{TOA} \equiv \frac{F_{TOA}^+}{F_{TOA}^-}$ are given in Tab. 4.2, if this mean value is used as a spectrally invariant surface albedo in the calculations. The value of mean broad-band surface albedo $\bar{\omega}_{SFC}$ used is also shown in Tab. 4.2.

The differences of close to one percent in atmospheric transmissivity are caused by the typical spectral dependence of the surface albedo for vegetation. The albedo is small for wavelengths below $0.6 \mu\text{m}$, and increases significantly at the red edge around $0.7 \mu\text{m}$. Due to the decrease of Rayleigh scattering optical depth with wavelength (see Eq. 2.25), the albedo at shorter wavelengths is dominating the calculations of the diffuse irradiance. Hence, the assumption of a spectrally invariant surface albedo leads to an overestimate of the diffuse irradiance and the atmospheric transmissivity, as shown in Tab. 4.2. As water vapor absorption is strong in the spectral regions with high surface albedo, the overestimate of transmissivity is compensated by an underestimate of atmospheric absorption.

If the spectral dependence of the grass albedo resembles the true spectral dependence at the measurement sites, calculations show that the assumption of a spectrally invariant surface albedo of 18% leads to an overestimate of the atmospheric transmissivity of about 0.5% for the full range of solar zenith angles. The use of the mean broad-band surface albedo, as calculated from measurements of up- and downwelling irradiance at the surface, will lead to a further increase of this overestimate.

4.2.4 Solar Constant

To obtain the broad-band atmospheric transmissivity, the spectral distribution of the solar radiation incident at the TOA is used to weight the spectral transmissivities calculated for individual wavelength bands. Also, the magnitude of the solar constant is required to link the transmissivity and the corresponding CSGI.

The estimated uncertainty of the solar constant is 5 Wm^{-2} (Lenoble, 1993). Kato et al. (1997) find differences of similar magnitude in the CSGI as result of using different solar spectra in radiative transfer models. For our calculations, the solar spectrum of Kurucz (1995), as included in version 4.0 of MODTRAN, has been used to infer the solar irradiance at the TOA within a given spectral band.

4.2.5 Further Sensitivities

Several other factors have influence on the accuracy of radiative transfer calculations, but are small for the LDK setup and the output values of the CSGI. The lack of polarization treatment in radiative transfer leads to negligible errors (Lacis et al., 1998). The discrete ordinate method considering 8 streams is accurate for irradiance calculations (Valero and Bush, 1999). Rayleigh scattering properties are known rather well (Teillet, 1990). Changes in the vertical distribution of aerosols and gases are neglected, as they only affect the diffuse irradiance field for higher orders of scattering. For clear-sky atmospheres, variations in column densities are the dominating parameters for the global irradiance at the surface, as the typical number of scattering events remains low.

4.2.6 Conclusions

Realistic input parameters are an important prerequisite for an accurate modeling of the clear-sky radiation budget and the CGSI. However, most parameters can be represented by estimates of the climatological mean values without a significant loss of accuracy.

Realistic variation in atmospheric water vapor introduce changes in the order of a few percent in atmospheric transmissivity. However, a large part of this impact can be accounted for by models as information on the amount of water vapor present in the atmosphere is available from several sources, such as radiosondes, GPS stations or NWP predictions with sufficient accuracy. Changes in atmospheric transmissivity resulting from variations of atmospheric temperature, pressure and the column integrated amount of ozone are significantly smaller.

The largest source of variability and uncertainty in the clear-sky radiation field originates from the interaction with aerosols. The available information about the optical properties of aerosols is too limited to allow an accurate representation in radiative transfer models for the dataset used here. As a consequence, both a significant bias and a statistical scatter have to be expected between observed irradiances and values calculated by radiative transfer schemes.

The practice of assuming a spectrally invariant surface albedo in radiative transfer calculations leads to a small but systematic bias in atmospheric transmissivity and absorption for vegetated surfaces, which is the dominating type of land cover for the measurements used in this study.

4.3 Model Intercomparison

In the previous section, the sensitivity of radiative transfer calculations to the input parameters has been analyzed. Here, values of the CSGI obtained by different RTMs are compared. Differences in the partitioning of the incident solar energy are also studied. For this purpose, the TOA albedo $\omega_{TOA} = \frac{F_{TOA}^+}{F_{TOA}^-}$, and the absorptivities of the atmosphere $\mathcal{A}_{ATM} = \frac{F_{TOA} - F_{SFC}}{F_{TOA}^-}$ and the surface $\mathcal{A}_{SFC} = (1 - \omega_{SFC}) F_{SFC}^-$ are calculated with identical inputs. This is done in order to quantify the uncertainties resulting from the different algorithms and assumptions used by the RTMs.

4.3 Model Intercomparison

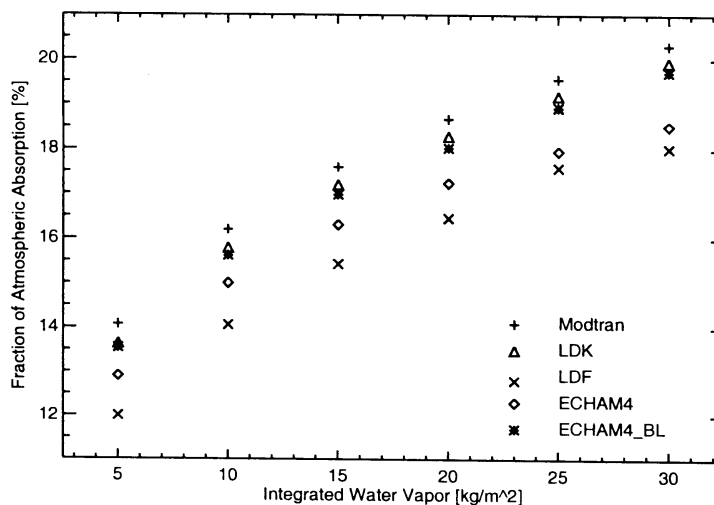


Figure 4.1: Fraction of solar radiation absorbed in an aerosol-free reference atmosphere (in % of incident irradiance) as a function of vertically integrated water vapor for a high sun ($\mu_0 = 0.8$) and calculated by different radiative transfer models.

Five different models are considered. The most detailed model is the current version 4 of MODTRAN (Berk et al., 1989). It performs calculations at a high spectral resolution of 1 cm^{-1} , is based on the 1996 release of the HITRAN database (Rothman et al., 1998), and incorporates recent updates to the water vapor absorption (Giver et al., 2000). Calculations done by this model are rather time consuming. Its results are therefore used only as references for an evaluation of the LDK scheme and an otherwise identical setup using the 6 band correlated-k scheme of Fu and Liou (1992), which is referred to as the LDF setup. Lastly, the highly parameterized radiative transfer scheme included in the ECHAM4 GCM (Roeckner et al., 1996) is tested as an example of radiative transfer schemes developed for use in GCMs. A modified version including an updated parameterization of water vapor absorption proposed by Bennartz and Lohmann (2001) is also evaluated.

A source of deviations originates from the differences in the spectral ranges considered by the RTMs. The spectral range is $0.24 - 4.6 \mu\text{m}$ for MODTRAN and LDK calculations and $0.2 - 4.0 \mu\text{m}$ for the LDF and ECHAM4 schemes. To obtain comparable results, the solar spectrum within the considered spectral range has been scaled to be equal for all models, and to correspond to the spectral range of the LDK setup ($0.24 - 4.6 \mu\text{m}$, containing 1358.5 W m^{-2} of the 1368.0 W m^{-2} of the Kurucz, 1995, spectrum).

4.3.1 Water Vapor Absorption

Gaseous absorption within the solar spectral region is dominated by water vapor. An accurate treatment is required in radiative transfer models to avoid biased estimates of the shortwave radiation budget (Bennartz and Lohmann, 2001).

An atmosphere free of aerosols is chosen for testing the treatment of gaseous absorp-

tion to avoid uncertainties due to differences in the aerosol formulation. A high sun ($\mu_0 = 0.8$), and 6 values of the water vapor ranging from 5 to 30 kg m⁻² are used for this purpose.

The results of the LDK scheme show good agreement with the MODTRAN calculations, with the LDK values being lower by about 0.5%. Possibly, this is caused either by the neglect of trace gases in LDK, or by the use of updated absorption data in MODTRAN. A part of this difference is also present if no water vapor is included in the model atmosphere.

The LDF scheme predicts significantly less atmospheric absorption as compared to the LDK and MODTRAN results. Several possible reasons exist. Only water vapor is considered as absorber in the shortwave spectral range. No treatment of continuum water vapor absorption is included. Furthermore, the underlying spectroscopic dataset used for the derivation of the scheme is rather old (Rothman et al., 1983). No attempt has been made to quantify these effects separately. In the current form, the Fu and Liou (1992) scheme cannot be recommended for applications relying on a high accuracy of the calculations.

The atmospheric absorption is also significantly underestimated by the ECHAM4 radiative transfer scheme in its original form. Applying the modified treatment of water vapor absorption proposed by Bennartz and Lohmann (2001) (referred to as ECHAM4.BL) which is based on data from Giver et al. (2000), the ECHAM4.BL and LDK schemes agree rather well. Hence, the algorithm used within ECHAM4 is capable of achieving accurate results in principle and only suffers from shortcomings in the description of water vapor absorption in the original version.

Differences in CGSI and planetary albedo are similar in magnitude to the differences in atmospheric absorption, and only small deviations are found for the MODTRAN, LDK and ECHAM4.BL results.

4.3.2 Radiation Budget for the Reference Atmosphere

Here, the model estimates of the shortwave radiation budget are compared for the reference atmosphere described in Sec. 4.2. In particular, model results for the CGSI, the amount of atmospheric and surface absorption and the planetary albedo are compared.

The same aerosol optical properties are used as input to the MODTRAN, LDK and LDF models. However, some remaining discrepancies are expected due to the interpolation to the spectral bands of the model, especially for the rather large bands of the LDF scheme. The aerosol optical depth prescribed in ECHAM4 for the Netherlands has been changed to match the value used in the other models, as the ECHAM4 value overestimates the measurements of Stammes and Henzing (2000) by a factor of two. Without this modification, large differences have to be expected, which would make a comparison meaningless. Other aerosol optical properties have been left unchanged, as the available information is not sufficient to identify the more realistic description.

The results of MODTRAN and the LDK scheme for the different radiation components agree closely within half a percent. The remaining differences can be attributed to the slightly higher atmospheric absorption present in MODTRAN. The results of the LDF scheme are affected by the underestimate of gaseous absorption mentioned previ-

4.3 Model Intercomparison

Model	μ_0	CSGI	\mathcal{A}_{SFC}	ω_{TOA}	\mathcal{A}_{ATM}
MODTRAN	0.8	840.0	63.45	17.70	18.85
LDK		838.7	63.28	18.24	18.48
LDF		862.2	65.17	18.25	16.58
ECHAM4		847.9	64.09	16.86	19.05
ECHAM4_BL		841.6	63.62	16.67	19.71
MODTRAN	0.5	476.4	57.55	20.75	21.70
LDK		476.1	57.47	21.28	21.25
LDF		495.0	59.86	20.96	19.17
ECHAM4		481.2	58.19	19.58	22.23
ECHAM4_BL		476.3	57.60	19.33	23.07
MODTRAN	0.2	145.1	43.60	28.27	28.14
LDK		144.5	43.59	28.87	27.54
LDF		155.0	46.86	27.89	25.26
ECHAM4		142.9	43.20	26.93	29.87
ECHAM4_BL		138.1	41.76	26.46	31.78

Table 4.3: Clear-sky global surface irradiance (CSGI, in W m^{-2}), atmospheric and surface absorptivity (\mathcal{A}_{SFC} and \mathcal{A}_{SFC}) and the planetary albedo (ω_{TOA}) as calculated by the models for the reference atmosphere at three solar zenith angles.

ously. Both the modified and the unmodified ECHAM4 scheme calculate the highest atmospheric absorption and a differing distribution of radiation. This results mainly from a higher aerosol absorption and differences in the asymmetry parameter prescribed by ECHAM4’s aerosol climatology. In agreement with the results of Sec. 4.2, an increase of discrepancies in CSGI at larger solar zenith angles is observed. As the atmospheric absorption is further increased by the adjustment of water vapor absorption, the differences to the MODTRAN and LDK models are larger for the ECHAM4_BL than for the ECHAM4 model.

4.3.3 Conclusions

Recent RTMs, represented by MODTRAN, LDK and ECHAM4_BL, show good agreement in calculations of the clear-sky solar radiation budget. Even the highly parameterized treatment employed in ECHAM4 does not cause a significant loss of accuracy in clear-sky conditions. The limited knowledge of aerosol optical properties dominates the uncertainty in estimates of the solar radiation budget calculated by different RTMs.

The discrepancies of the LDF and the ECHAM4 models are mainly caused by a lower gas absorption, in particular due to water vapor. This suggests that model disagreements found in previous studies (see e.g. Fouquart et al., 1991) might be attributable to old and inaccurate spectroscopic datasets which underestimate the absorption by atmospheric gases.

Calculations made with the LDK scheme offer a comparable accuracy to MODTRAN results, a conclusion which justifies the choice of LDK as the tool for the sensitivity

study presented in Sec. 4.2, and for further radiative transfer calculations presented within this thesis.

4.4 Comparison of Model Calculations and Measurements

The good mutual agreement of the MODTRAN, LDK and the ECHAM4.BL radiative transfer schemes supports the assumption that these models represent our current understanding of clear-sky radiative transfer processes. To put this understanding to test, a comparison of model results and observational data is presented here. While the LDK setup is used for this comparison, results would be similar if any of the two other models were used instead.

4.4.1 Measurements

Pyranometer measurements by Kipp en Zonen CM 11 instruments collected at 16 synoptic observation stations of KNMI's operational network are analyzed in this comparison. Details about the measurements and their expected accuracy are given in Ch. 3. The measurements are available as 10-minute averages of the solar irradiance. A record has been included in the comparison, if the 10-minute interval precedes a synoptic report of zero octa cloud cover.

Due to the operation conditions of the instruments, a number of quality checks have to be performed on the measurements. Data are rejected, if the minimum and maximum reported CGSI within a 10 minute interval deviated by more than 30 Wm^{-2} , to avoid cloud contamination and defective instruments. As ice and frost can affect the measurements through reflection and attenuation of radiation (Kuik, 1997), only data measured at temperatures above 3° C are considered. Further consistency checks are performed to identify corrupted records in the database. 6,132 individual measurements pass these criteria for the time period from the year 1995 until the end of 2000. About 5% of the measurements are identified as corresponding to clear-sky conditions, and roughly 70 % percent pass the quality checks, with most of the rejections caused by the temperature threshold.

Relevant systematic uncertainties affecting the pyranometer measurements are the contamination of the glass domes of the instruments by the deposition of dust, the thermal offset, and the resulting calibration uncertainty described in (see Ch. 3). None of these effects can be quantified with sufficient accuracy to allow a correction for the present dataset. Hence, their resulting uncertainties are used a posteriori to judge the relevance of observed differences between observations and model results for the accuracy of the RTMs.

4.4.2 Model Data

A simple method for deriving model estimates of the solar irradiance at the surface has been implemented. Calculations of the CGSI from the LDK scheme at 40 equidis-

4.4 Comparison of Model Calculations and Measurements

tant values of the cosine of the solar zenith angle have been stored in lookup tables. The atmospheric properties are specified as described in Sec. 4.2. To account for the variability of CSGI caused by changes in water vapor in the model, three sets of these tables are generated, with the climatological mean value of the vertically integrated water vapor (IWV) varied by its standard deviation. The value corresponding to individual measurement has been inferred from the radiosondes launched at De Bilt every six hours by linear interpolation in time. For each measurement, the CSGI is estimated by bilinear interpolation of the lookup tables in the cosine of the solar zenith angle and the estimated value of IWV.

The inclusion of the IWV in the model increases the correlation of calculated and observed transmissivities from 0.88 to 0.92. It also leads to a reduction of the standard deviation of both datasets from 4.7% to 3.7%. Both facts indicate that the choice to account for variations in water vapor absorption leads to a significant improvement in the quality of model estimates of the transmissivity. However, a slight increase of the bias by 0.2% results, because the lookup tables are calculated for a climatological mean IWV of 16.4 kg m^{-2} , which overestimates the IWV during clear-sky situations.

4.4.3 Comparison

Fig. 4.2 shows the estimated distribution density of the difference between measured and modeled clear-sky shortwave atmospheric transmissivities. Contour lines enclose a specified percentage of the data points for a given value of μ_0 .

The behavior of the model at values of μ_0 smaller than 0.2 is probably unrealistic, as the setup used for the radiative transfer calculations does not account for the sphericity of the Earth and diffraction of the direct beam. Also, the measurements become increasingly unreliable. Hence, only values of μ_0 larger than 0.2 are discussed.

The model predicted values of the total atmospheric transmissivity are significantly larger than the measured values for all solar zenith angles, ranging from about 3% of the incident solar irradiance at high sun to about 5% at $\mu_0 = 0.2$. This results in a mean overestimate of the atmospheric transmissivity by 4.5% and the CSGI by 25.7 W m^{-2} for the complete dataset. While the bias and standard deviation are expected to be a smooth function of the solar zenith angle, some variability of the bias is present in the figure. This is visible at the value of $\mu_0 = 0.5$, where the overestimate is significantly larger than the values found for the two surrounding bins. Autocorrelation of the measured irradiances is a plausible explanation. Similar aerosol properties and amounts of water vapor determine the measurements corresponding to a single clear-sky situation. Often, such conditions persist over time periods of a few hours up to several days, and extent over most of the meteorological stations used here due to their small distances. Hence, a single clear-sky episode can contribute dozens of data points to the used dataset, which are not statistically independent. The removal of autocorrelation would require a weighting of the data taking into account their statistical dependence. A quantification of the spatial and temporal correlation of individual measurements is required for this, which is outside the scope of this study. Instead, a simplified approach is used. The mean bias of modeled and measured atmospheric transmissivities are calculated for each year and bin of the cosine of the solar zenith angle having a width

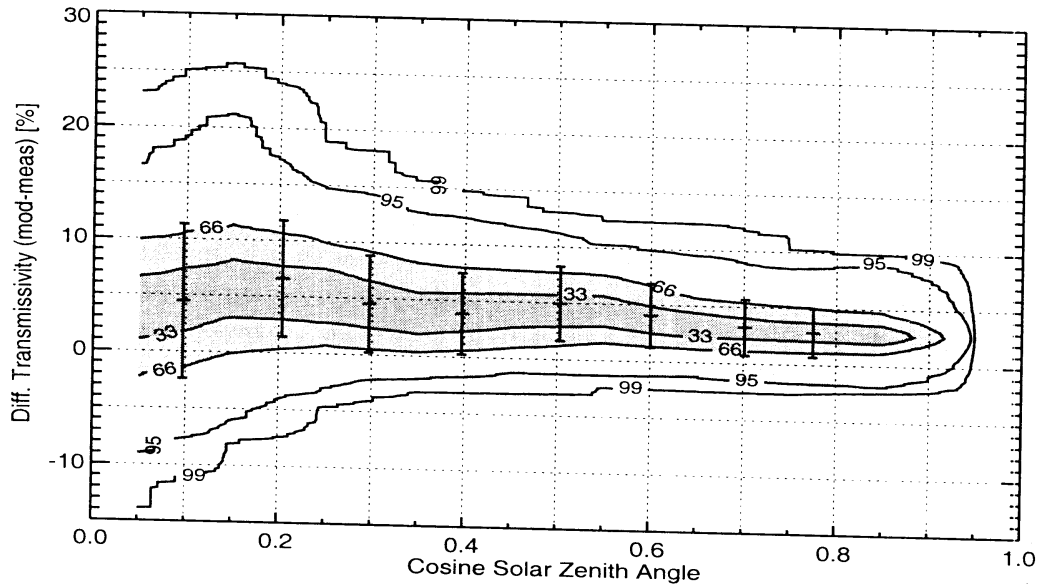


Figure 4.2: Estimated distribution density of the differences between observed and modeled clear-sky shortwave atmospheric transmissivity (in % of incident irradiance) for the LDK scheme as function of the solar zenith angle. Also shown are the mean bias and the standard deviation obtained for 8 bins of the cosine of the solar zenith angle.

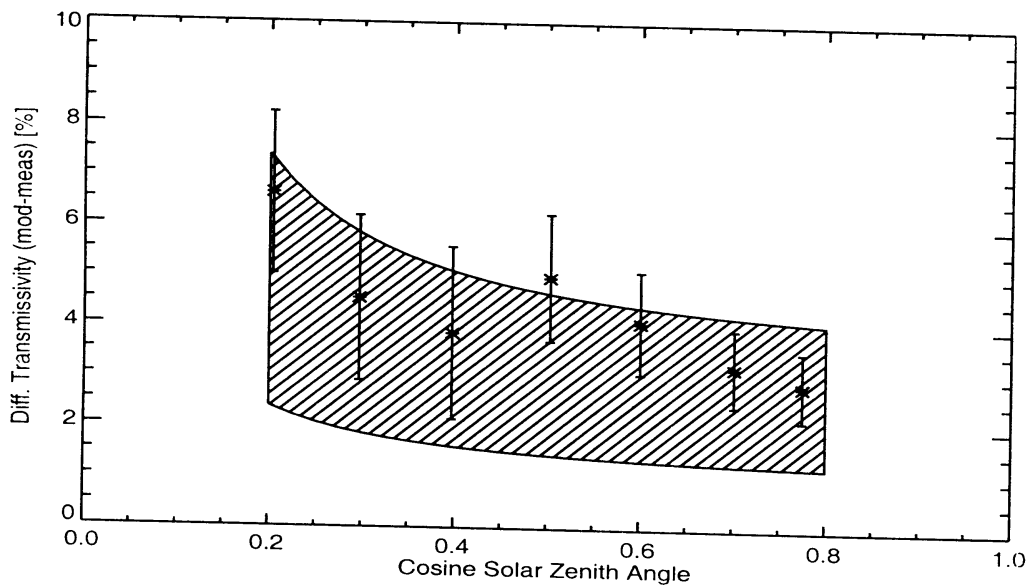


Figure 4.3: Mean and standard deviation of the bias of modeled and measured atmospheric transmissivities, calculated from yearly averages for 7 bins of the cosine of the solar zenith angle (for a complete description, see text). The shaded area indicates the range of systematic uncertainties.

4.4 Comparison of Model Calculations and Measurements

of 0.1, obtaining values which are certainly statistically independent. By calculating the total average and the standard deviation for the six yearly averages, a measure for both the size and the uncertainty of the bias is obtained. This range is shown by the error bars in Fig. 4.3. The large standard deviation indicates that autocorrelation indeed affects the estimate of a mean bias, unless other influences cause the significant interannual variability.

The estimates of pyranometer uncertainties given by the WMO (WMO, 1996) and stated to be 3 percent for hourly values of solar irradiance are insufficient to explain the observed systematic difference, as the majority of the error sources should have a random impact on the measurement and thus are not expected to cause a bias. Erroneous values of the mean aerosol optical depth or IWV used in the radiative transfer calculation are improbable, as they are based on sufficiently accurate measurements (see Sec. 4.2). Three systematic sources of uncertainty affecting the measurements and not accounted for by WMO (1996) have been identified in Ch. 3. These are the thermal offset of pyranometers ($10 \pm 5 \text{ Wm}^{-2}$), the influence of contamination on the measurements ($0.5 \pm 0.5 \%$), and a possible calibration bias as a result of the thermal offset ($0 - 2 \%$). Also, the representation of the surface albedo by a spectrally invariant value in the model calculations can lead to a bias (0.5%). All effects cause a reduction of the measurements or an apparently too-large modeled irradiance. To find the total range of systematic uncertainty resulting from the combination of individual uncertainties, the minimum and maximum absolute values of each uncertainty have to be added, which are listed in the brackets. This range is shown as shaded area in Fig. 4.3 as a function of the solar zenith angle, allowing a direct comparison with the mean bias.

The range of systematic uncertainties is sufficient to explain the full range of the observed systematic difference, as is visible in the plot. Hence, the model setup for inferring the CSGI described here is capable of reproducing measurements of CSGI within the limits set by instrumental shortcomings and model approximations.

On the other hand, an erroneous description of aerosol optical properties or gas absorption in the model can also be responsible for the bias. The thermal offset of pyranometers, combined with the resulting calibration bias, cause a significantly larger systematic uncertainty than demanded for secondary standard instruments by ISO (1996). Thus, a more accurate characterization of both effects is highly desirable to reduce the measurement uncertainty and enable a more thorough evaluation of the results of radiative transfer models.

The standard deviation between measured and model-calculated transmissivities allows an assessment of the quality of the model results and the measurements. An increase of the standard deviation with solar zenith angle from a value of 2 percent at $\mu_0 = 0.8$ to about 5 percent at $\mu_0 = 0.2$ is visible in Fig. 4.2. This range is consistent with the variability expected from the sensitivity study as well as instrumental uncertainties, and can be attributed mainly to variations in aerosol optical properties (see Tab. 4.1). This result is an indication that the estimates of random instrumental uncertainties and atmospheric variability made in this study are realistic, ruling out the neglect of large random error sources in the measurements or the radiative transfer calculations.

4.5 Summary and Conclusions

This study presents an intercomparison of five different radiative transfer schemes and actual measurements of the clear-sky downwelling solar irradiance for mean atmospheric conditions for the Netherlands.

Only minor deviations of calculated radiative fluxes at the surface and the top of atmosphere are found for recent radiative transfer schemes, if similar atmospheric and aerosol properties are prescribed as input parameters, a finding in contrast to earlier model intercomparisons (e.g. Fouquart et al., 1991). The remaining differences are easily explained by the algorithms used for the treatment of gas absorption and the employed numerical algorithms. As a consequence, the actual choice of model is of secondary importance for a comparison of measurements and model calculations. Significantly larger differences result from realistic variations of the aerosol properties used in the models. As the currently available information about the optical properties of aerosols for the Netherlands is limited, they cause the largest source of uncertainty in estimates of the clear-sky shortwave radiation budget.

Comparing pyranometer data with model results, the calculated atmospheric transmissivities overestimate the measured values by several percent at all solar zenith angles. This result is in agreement with several earlier investigations (e.g. Kato et al., 1997; Wild and Liepert, 1998). Four mechanisms are identified as likely contributors to this bias. The measurements are affected by contamination of the instruments ($0.5 \pm 0.5\%$), the thermal offset of pyranometers ($10 \pm 5 \text{ Wm}^{-2}$) and a possible calibration bias ($0 - 2\%$) as a result of the thermal offset. The neglect of the spectral dependence of the surface albedo in RTMs can also result in a systematic error, which is found to be in the order of 0.5% for vegetated surfaces.

The combination of these effects introduces a large range of systematic uncertainties in the pyranometer data and is sufficient to completely explain the observed bias. Hence, no shortcoming in the modeling of clear-sky radiative transfer can be identified. It should be noted, however, that this conclusion relies mainly on the existence of the thermal offset and the calibration bias, which have not been considered in traditional estimates of pyranometer uncertainty and are the subject of current investigations. As they are purely instrumental shortcomings, which possibly affect all records of pyranometer measurements, they have to be viewed as a major obstacle for a more thorough evaluation of the modeling of clear-sky radiative transfer. Improved instrumentation, combined with detailed measurements of aerosol optical properties, are hence essential requirements for evaluating and improving the treatment of aerosols and gaseous absorption in radiative transfer models, as well as accurate estimates of the clear-sky radiation budget.

Chapter 5

Comparison of Cloud Optical Depths Retrieved from Transmitted and Reflected Solar Radiation

5.1 Introduction

Clouds significantly influence the radiation budget of the atmosphere (e.g. Bishop and Rossow, 1991). As clouds exhibit large variability over a wide range of spatial and temporal scales (Rossow and Lacis, 1990; Cahalan and Joseph, 1989), accurate information about the statistical properties of the relevant cloud parameters including their regional dependence is required to assess the impact of clouds on the Earth's climate. The density and coverage of the traditional network of meteorological stations are too limited to provide the required information on a global scale. Current and upcoming meteorological satellite observations are much better suited for this task due to their larger spatial coverage and the high spatial and temporal resolution of their measurements. On the other hand, the products retrieved from satellites need to be evaluated with independent data to establish their accuracy and identify possible shortcomings.

In the presence of clouds, variations in the reflection and transmission properties of the atmosphere across the solar spectral region are dominated by changes in cloud optical depth τ (see e.g. van de Hulst, 1980). Hence, the cloud optical depth is the single most important parameter for quantifying the influence of clouds on the solar radiation budget. It is also closely related to the cloud water present within a vertical column, the liquid water path (*LWP*). For a given effective radius r_{eff} of the cloud droplet size distribution, it is linked to the *LWP* with high accuracy by

$$\tau = \frac{3}{2} \frac{LWP}{r_{eff} \rho_{H_2O}}, \quad (5.1)$$

where ρ_{H_2O} is the density of water (e.g. Kriebel, 1989). For this relation, the effective radius of a cloud droplet size distribution is defined as

$$r_{eff} \equiv \frac{\int \eta(r) r^3 dr}{\int \eta(r) r^2}, \quad (5.2)$$

5.2 Instrumental Data

where η is the spectral number density of droplets. The effective radius is also the main parameter determining the cloud optical parameters required for irradiance calculations, which are given by the single scattering albedo and the asymmetry parameter (Hu and Stamnes, 1993). These relations provide a convenient means to incorporate cloud microphysics in radiative transfer schemes.

The most comprehensive source of information available on the global climatology of cloud optical depths is provided by the International Satellite Cloud Climatology Project (ISCCP) (Rossow and Schiffer, 1991). Their retrieval method is based on the relation of top-of-atmosphere (TOA) reflectance and cloud optical depth (see e.g. King, 1987), which is widely used in remote sensing. Several studies have also been reported in the literature which derive cloud optical depths from transmitted solar radiation (e.g. Leontyeva and Stamnes, 1994; Barker et al., 1998).

Comparing both methods, Barker et al. (1998) and Min and Harrison (1996) find significantly higher values of cloud optical depth if it is inferred from transmitted instead of reflected radiation. These results hint at the existence of unidentified problems hidden either in the measurements or in the retrievals and the underlying representation of cloud-radiation interactions. Furthermore, they are consistent and probably related to the generally too large model-predicted atmospheric transmissivities reported by Cess et al. (1995) and Ramanathan et al. (1995) in comparison to observations. Those findings have led to a controversial and ongoing debate about the accuracy of the representation of atmospheric absorption in current radiative transfer models (Stephens, 1996), an aspect which is of major importance for a correct modeling of the climate system (Ramanathan, 1987).

The current study compares cloud optical depths derived from simultaneous and collocated measurements of reflected and transmitted solar radiation collected during a six-year period throughout the Netherlands. The large number of more than 40,000 cases allows a statistically significant evaluation of systematic and random differences of both retrievals.

In the next section, the measurements used for this investigation are described. Then, a summary of the radiative transfer scheme at the heart of the retrieval is given, together with details on the inversion procedure applied to the measurements. This is followed by the comparison of the results of both retrievals under different conditions. Possible mechanisms leading to the observed discrepancies of the two retrievals are discussed to judge the implications for the accuracy of the derived optical depths. Finally, a summary of the findings is given and suggestions for future research are made.

5.2 Instrumental Data

For the estimation of cloud optical depths from reflected and transmitted solar radiation, satellite data of the $0.63\ \mu\text{m}$ reflectance obtained by the AVHRR instrument flown on board the NOAA-14 satellite are used together with simultaneous and collocated measurements of the global downwelling solar irradiance as obtained from KNMI's network of 32 meteorological stations located throughout the Netherlands. Only a quick summary of the data is given here as a detailed description can be found in Ch. 3. The satellite measurements have been restricted to observations obtained from

5. Cloud Optical Depth from Transmitted and Reflected Solar Radiation

the NOAA-14 satellite to avoid problems caused by the possibility of inconsistent calibrations of different AVHRR instruments. Images starting from March 1995, when NOAA-14 commenced operational transmission of measurements, until the end of the year 2000 are included in the comparison. Both the radiance and irradiance values have been renormalized to mean sun – Earth distance and converted to bidirectional reflectance and transmissivity which are used as retrieval inputs.

5.2.1 Pyranometer

Secondary standard pyranometers of type CM 11 built by Kipp en Zonen are used for the measurement of global solar irradiance at KNMI's meteorological stations. The minimum, mean and maximum values of irradiance measured during a ten-minute interval are recorded. To be classified as a secondary standard instrument, the WMO demands an accuracy of 3% for hourly mean values of the irradiance (WMO, 1996). As the instruments are operated automatically without ventilation and heating and checked at rather long maintenance intervals of up to a year, the accuracy of the measurements is somewhat degraded by the deposition of pollution on the instrument's glass domes, but has been found to not exceed 5% (Kuik, 1997).

However, recent investigations of pyranometer accuracy suggest that the estimates of instrumental errors forming the basis of WMO (1996) are too optimistic. Bush et al. (2000) report a significant systematic underestimates of solar irradiance measurements as a result of thermal cooling of the detectors, a finding confirmed by several other studies. While this thermal offset is more important in clear-sky than in cloudy conditions, it can also lead to an erroneous calibration of pyranometers (see Ch. 3 or Philipona, 2002). Initial results of a comparison of traditional and improved measurements which are compensated for these effects report an underestimate in mean solar irradiance in the range of 3 – 8% by traditional measurement setups in all-sky conditions (Philipona, 2002). However, part of the difference could also be caused by rain drops, frost and ice reducing the transmission of the dome of the instruments.

At this stage, the mechanisms leading to this underestimate are still speculation, allowing no reliable estimate of the mean influence on long-term measurements. Hence, no correction of the data is possible. Nevertheless, the effects of such a bias on the retrieval of cloud optical depths will be quantified and discussed later on in this study.

5.2.2 NOAA-14 AVHRR

The AVHRR instrument on board the NOAA series of polar-orbiting sun-synchronous satellites is one of the main sources of global information about cloud properties (e.g. Rossow and Schiffer, 1991; Han et al., 1994). The AVHRR instrument acquires satellite images with a viewing angle range of 55 degrees across track and has a nadir pixel resolution of approximately $1.1 \times 1.1 \text{ km}^2$. Images are taken at 5 wavelength channels (0.63, 0.89, 3.7, 11 and $12 \mu\text{m}$). For the current investigation, only the $0.63 \mu\text{m}$ channel is used in the retrieval. Due to degradation of the detectors during launch and over time, combined with the lack of an on board calibration source, the sensitivity of the shortwave channels of the AVHRR instruments are only known with limited accuracy.

5.3 Retrieval Technique

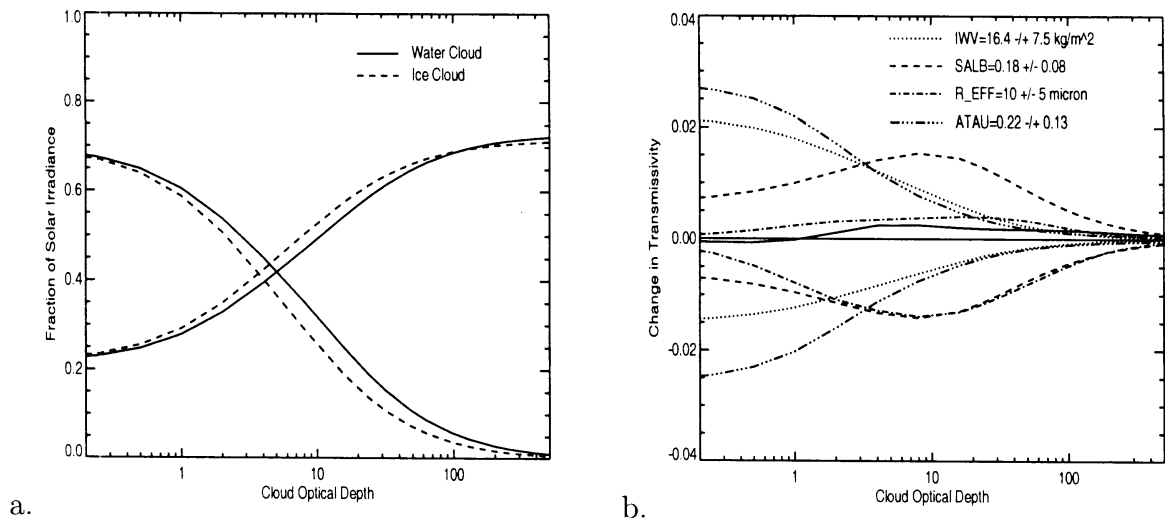


Figure 5.1: (a.) Dependence of broad-band atmospheric transmissivity and planetary albedo on cloud optical depth at $0.55 \mu\text{m}$ for a water and an ice cloud at a solar zenith angle of 60° and standard overcast conditions found in the Netherlands. (b.) Absolute changes in atmospheric transmissivity as function of cloud optical depth due to realistic variations of the assumptions required for the radiative transfer calculations in comparison to the water cloud results shown in(a.).

In case of the NOAA-14 AVHRR, the issue is further complicated by the low temporal stability and the non-linear degradation of the two shortwave channels (see Fig. 1 of Tahnk and Coakley, 2001b). If the coefficients obtained by earlier calibration studies were applied to data collected after the year 1998, this would lead to a rather strong overestimate of the measured reflectances. To minimize the expected error resulting from calibration uncertainties, the mean of the two sensitivities derived from the calibration coefficient reported by Nguyen et al. (2001) and Tahnk and Coakley (2001b) are used. The absolute accuracy of the sensitivity is unlikely to be better than about 5%, as is concluded in Ch. 3. This accuracy translates to an equal relative accuracy of the measured reflectances. Because typical reflectances of cloudy scenes are in the order of 25 – 80%, an absolute uncertainty of about 1 – 4% has to be expected.

5.3 Retrieval Technique

The basic principle of the retrieval of cloud optical depth from reflected and transmitted solar radiation is the unique relation of both radiative quantities to the cloud optical depth. An example of this relation is shown in Fig. 5.1.a for atmospheric conditions representative for the Netherlands and a solar zenith angle of 60° . The retrieval procedure assumes that the monochromatic cloud optical depth at any particular wavelength, here chosen to be $0.55 \mu\text{m}$, is the only free parameter, and other effects can be modeled with sufficient accuracy. Two major limitations of this assumption exist.

First, large errors will result from small errors in the retrieval inputs or the estimate

5. Cloud Optical Depth from Transmitted and Reflected Solar Radiation

of the retrieval function, as the retrieval error grows approximately proportionally with the magnitude of the cloud optical depth. Hence, the retrieval results are extremely sensitive to uncertainties resulting from erroneous assumptions and shortcomings in the radiative transfer model, as well as measurement errors. Typical variations in broad-band atmospheric transmissivity (BAT) resulting from realistic variations in input parameters of the radiative transfer model are shown in Fig. 5.1.b for the water cloud situation presented in Fig. 5.1.a, and will be discussed in more detail in Sec. 5.3.3. Variations of integrated water vapor (IWV), surface albedo (SALB), effective droplet radius of the cloud (R_EFF) and the aerosol optical depth (ATAU) are plotted.

The second limitation is of more fundamental nature, as the existence of the one-to-one relation assumed within the retrievals is closely coupled to the concepts of plane-parallel horizontally homogeneous clouds and one dimensional radiative transfer theory. However, real clouds show significant variability in time and space (4D) which can lead to a breakdown of the invertible relations required by both retrievals (Várnai and Marshak, 2001; Boers et al., 2000).

For the present study, the KLAROS satellite analysis environment (Feijt, 2000) is used to calibrate the images and calculate the viewing geometry. A detailed radiative transfer code is used to calculate the relation of cloud optical depth to radiances and irradiances, which is different from the standard KLAROS setup. A description of the radiative transfer calculations is given in the following section. Uncertainties of both retrievals arising from measurement shortcomings and assumptions made about the input parameters used in the radiative transfer calculations are discussed. Finally, details about the lookup tables and the technique used to infer the cloud optical depth from these lookup tables are given. The relevance of 4D cloud structure and its impact on the retrievals is subject of ongoing research and will be covered in the discussion of the results.

5.3.1 Radiative Transfer Model

The radiative transfer calculations are conducted with the libRadtran software package (Kylling and Mayer, 2001) and the setup described in Ch. 2. To solve the RTE, the DISORT algorithm (Stamnes et al., 1988) has been selected, using 8 streams for the modeling of irradiances and 72 streams for radiances. The correlated-k distributions of Kato et al. (1999) and Kratz (1995) are used to account for gaseous absorption within the atmosphere for the total solar wavelength interval and the spectral ranges of the AVHRR 0.63 μm channel, respectively.

The atmosphere is represented by the midlatitude summer profile of Anderson et al. (1986). However, the mean vertically integrated water vapor column is adjusted to 16.4 kg m^{-2} and the ozone column to 328 DU, which are the climatological mean values for De Bilt, the Netherlands (52.10° N, 5.17° E). An aerosol profile with an optical depth of 0.1925 at 0.55 μm and of water-soluble composition is included in the atmosphere. More details and a justification of this treatment are given in Ch. 4.

To incorporate the effects of clouds in this atmosphere, both a representative water cloud and an ice cloud are assumed. The water cloud droplet size spectrum is given by a Gamma-shaped distribution with an effective radius of 10 μm and an effective variance

5.3 Retrieval Technique

of 0.1. This choice of droplet spectrum is consistent with the ISCCP retrievals (Rossow and Schiffer, 1991). Furthermore, the results of a global survey of mean effective radii conducted by Han et al. (1994) confirm this as a typical mean value for Northern hemisphere mid-latitude conditions. They also report a natural variability given by a standard deviation of the observations of about $\pm 5 \mu\text{m}$. The optical properties of the cloud are calculated using Mie theory. The cloud base and top altitudes are fixed to 1 and 2 km in the atmosphere, and vertically homogeneous profiles of the cloud optical properties are assumed.

For the altitude of the ice cloud, the height interval from 8 to 9 km is chosen. Compared to water clouds, much more uncertainty exists in the optical properties of ice particles which are caused by the large variety of crystal sizes and shapes found under typical atmospheric conditions (Pruppacher and Klett, 1978). For our study, the optical properties of the C2 model (Hess and Wiegner, 1994) consisting of imperfect hexagonal ice crystals and obtained by ray-tracing calculations are used (Hess et al., 1998). This choice is motivated by the findings of Knap et al. (2002) who compare the model-calculated and measured angular dependence of bidirectional reflectances for ice-cloud scenes observed by the POLDER instrument. From several commonly used crystal shapes, this model and the model of C.-Labonnote et al. (2000) reproduce the observed angular dependence best, achieving significantly better performance than e.g. the polycrystals of Macke et al. (1996) which are used as basis for the ISCCP cloud property retrievals (Rossow et al., 1996; Doutriaux-Boucher et al., 2000).

A realistic estimate of the surface albedo is a further important prerequisite for an accurate retrieval of cloud optical depth from reflected and transmitted solar radiation (King, 1987; Leontyeva and Stamnes, 1994). The dominating land cover throughout the Netherlands, and in particular at the measurement stations, are grass pastures and low vegetation. For grass land within the $0.63 \mu\text{m}$ spectral region and the total solar spectrum, typical values of 10% and 18% are reported in the literature (e.g. Bowker et al., 1985). Effects resulting from spectral dependence and bidirectionality of the surface albedo have been neglected. Attempts to obtain the broad-band surface albedo from clear-sky AVHRR images by a standard retrieval similar to Csiszar and Gutman (1999) confirm this estimate, but show a rather large case-to-case variability. It is unclear whether this variability is mainly caused by real changes of surface albedo or rather the effects of remaining cloud contamination, variations in aerosol profile and the changes in viewing geometry. The use of this data was further complicated by the limited calibration accuracy of the $0.9 \mu\text{m}$ channel, which introduced large interannual variations of the mean clear-sky reflectance in this channel. Hence, it has been decided not to include this information in the retrieval and rely on climatological mean values instead.

5.3.2 Retrieval Procedure

To reduce the computational time to a feasible level, the radiative transfer calculations have been done off-line for representative mean conditions and stored in lookup tables.

For the generation of the lookup tables, radiative transfer calculations have been conducted at equidistant values of the cosine of the solar zenith angle (0.1-1.0 in steps

5. Cloud Optical Depth from Transmitted and Reflected Solar Radiation

of 0.05). At each value of the solar zenith angle, 14 values of the cloud optical depth are used ranging from 0.125 to 512 and spaced at integer powers of 2. For the satellite retrieval, radiances have been output at 19 values of the relative azimuth ($0 - 180^\circ$ in steps of 10°) and the cosine of the satellite zenith angle (0.4-1.0 in steps of 0.05). As the BAT is significantly influenced by the vertically integrated water vapor (IWV), three sets of lookup tables are generated, based on values of the mean IWV and its standard deviation (8.9, 16.4 and 23.9 kg m^{-2}). For the model inversion, the function linking cloud optical depth and the reflectance/transmissivity is obtained by multi-linear interpolation in the parameters describing the geometrical setup of satellite, sun and the pyranometer. For the transmissivity, a further linear interpolation in IWV is used to estimate the retrieval function corresponding to the actual IWV of the pyranometer measurement, which is obtained from the radiosonde soundings conducted at De Bilt at six hour intervals. As a smooth function linking cloud optical depth and reflectance is expected, bicubic spline interpolation is used to determine the cloud optical depth corresponding to a given measurement.

5.3.3 Sensitivity of the Retrievals

Detailed sensitivity analyses of retrievals similar to the two schemes used for the current study have been given previously (see e.g. Leontyeva and Stamnes, 1994; Barker et al., 1998; King, 1987; Han et al., 1994). Only a short overview is given here. Uncertainties affecting the results can be classified into four groups: Limited knowledge exists about the true input parameters required for the radiative transfer calculations. The measurements used as the inputs to the retrieval have an uncertainty caused by instrumental shortcomings. The accuracy of the forward model is limited, and the concepts forming the basis of the model might not include all relevant processes. Estimates of the measurement uncertainties have been given in Sec. 5.2. Here, the uncertainties resulting from our limited knowledge about correct inputs to the radiative transfer calculations are described. Comparing this estimate to observed discrepancies of the two retrievals will allow us to assess both the validity of the conceptual models forming the basis of the retrievals and the accuracy of the radiative transfer model.

The spectral range of the $0.63 \mu\text{m}$ AVHRR channel has been selected to minimize the influence of the atmosphere and simplify the retrieval of cloud and surface properties. Hence, only minor changes of less than one percent result from realistic variations in the gaseous profiles for the model-calculated reflectances, with largest variability originating from changes in the column amounts of water vapor and ozone. For the broad-band solar spectral interval, much larger variations of the surface irradiance are found due to changes in water vapor caused mainly by the presence of strong absorption lines in the near infrared. The relevance of these changes decreases with increasing cloud optical depth. In the setup presented here, a large fraction of this variation should be compensated by the use of an interpolated version of the lookup table corresponding to the actual value of the IWV for each measurement.

For standard atmospheric conditions, changes of the BAT by several percent can result from variations in aerosol properties. Much less impact is found for the TOA reflectances, as most of the aerosol is located at or below the level of the cloud and the

5.3 Retrieval Technique

aerosol optical depth decreases towards larger wavelengths (see Ch. 4).

A reliable estimate of the surface albedo is required for accurate radiative transfer calculations. While significant errors for the satellite analysis are mainly expected for small cloud optical depths or the detection algorithms for the presence of clouds, multiple reflections of photons between the cloud base and the ground introduce a high dependence of downwelling surface irradiance on the surface albedo ω_{SFC} . The increase of the downwelling solar irradiance caused by surface reflections is given by the factor $(1 - \omega_{sfc})^{-1}$ to a good approximation in the presence of optically thick clouds (Barker et al., 1998).

A correct representation of the optical properties of the cloud is very important for accurate retrieval results. Ice and water droplets have different phase functions, which is already indicated by a large difference in asymmetry parameter (0.86 for the water cloud and 0.77 for the used ice crystal model at a wavelength of $0.55 \mu\text{m}$). Hence, a reliable separation of cloud cases according to the thermodynamic phase of the cloud is particularly desirable, as the scaled optical depth τ' , defined by $(1 - g)\tau$, is the parameter which dominates the BAT and the planetary albedo for the case of conservative scattering (King, 1987). In this formula, τ denotes the true cloud optical depth and g the asymmetry parameter. For the satellite retrieval, changes in the higher-order moments of the phase functions can lead to additional changes in the anisotropy distribution function (ADM) of up to several percent. As the ADM is required for linking the measured reflectances and the hemispherical albedo, a further uncertainty is introduced for the satellite retrieval. The phase function depends on the cloud droplet size distribution. Han et al. (1994) estimate a random uncertainty of about 7% in estimates of the cloud optical depth as a result of assuming a constant effective radius of $10 \mu\text{m}$. On the other hand, the absorption of water droplets in the infrared spectral region and its dependence on droplet size leads to typical variations of the BAT in the order of 1 – 2%. This influence is especially important once effective radii of less than $6 \mu\text{m}$ are encountered.

Our calculations have shown negligible dependence of calculated transmissivities and reflectances on cloud height compared to the other sensitivities. Generally, errors due to the use of mean conditions increase with solar zenith angle, due to the longer path length of photons through the atmosphere. Hence, the retrievals are expected to produce most accurate results at small solar zenith angles. The retrieval function shown in Fig. 5.1 corresponds to a solar zenith angle of 60 degrees. From this value onwards, error increase rather rapidly, making retrievals at angles of more than 75 degree rather error-prone and unreliable.

A combined estimate of expected errors caused by the use of a single mean atmospheric state and incomplete knowledge of some of the input parameters is difficult to obtain due to the non-linear retrieval functions and possible correlations of some of the error sources, e.g. water vapor and aerosols. However, errors of the retrieved cloud optical depths are not expected to exceed the range of 10 – 20% for each of the two retrievals, even if the random uncertainties affecting the measurements used as retrieval inputs are included. At this stage, errors resulting from 4D cloud structure and systematic measurement errors are neglected on purpose as they will be the subject of further discussion in Sec. 5.5.

5.4 Comparison of Retrieval Results

Cloud optical depths retrieved from bidirectional reflectances as measured by the $0.63\ \mu\text{m}$ channel of the AVHRR instrument are compared to cloud optical depths obtained from broad-band global solar irradiances at the surface, which are inferred from pyranometer measurements. Scatter plots of the results are shown in Fig. 5.2 for all cases and Fig. 5.3 for selected cases which were chosen to resemble plane-parallel horizontally homogeneous clouds. Clouds with an infrared brightness temperature above 273 K and below 260 K are classified as water and ice clouds, respectively.

To obtain these cloud optical depths, a value of the BAT has been obtained from the mean level of irradiance during each 10-minute interval, which are archived by the instruments. Then, an average BAT is calculated from the 4 intervals closest to the time of the satellite overpass, and is used as input to the pyranometer retrieval. Average reflectances obtained from a 10×10 pixel grid located above the pyranometer are used for the satellite retrieval, corresponding to a region of about $11 \times 11\ \text{km}$ for a nadir view. The chosen averaging scales have been determined by trial and error to represent a reasonable trade-off between high resolution and maximum achievable correlation. Reducing the scales leads to a strong decrease of the correlation. For larger averaging scales, however, only slightly higher correlations are found. Nevertheless, this choice is somewhat arbitrary at this point, and its effects will be discussed in Sec. 5.5.

Only cases with a solar zenith angle less than 65 degrees and a satellite zenith angle of less than 55 degrees are included in the comparison. Furthermore, only data with a minimum reflectance exceeding 0.15 and having a maximum BAT 5% below the model-calculated clear-sky transmissivity are considered to ensure completely overcast scenes. These constraints have been selected to limit problems associated with the geometrical setup, collocation, cloud inhomogeneity and broken cloud fields (Boers et al., 2000; Várnai and Marshak, 2001). Results exceeding a cloud optical depth above 80 and 50 for water and ice clouds, respectively, in any one of the two retrievals are rejected. The retrieval functions become too sensitive to instrumental and modeling errors at larger values of the optical depth for reliable results, as is illustrated by the small magnitude of the slope in Fig. 5.1.a at large values of the optical depth. The upper limits of ice and water clouds correspond to approximately the same value of scaled optical depth (see King, 1987).

Significant deviations of the cloud optical depths obtained by both retrievals are observed for standard conditions, as is shown by the large scatter and the low correlation of 0.73 and 0.70 for the water and ice clouds displayed in Fig. 5.2. The separation of ice and water clouds does not improve the agreement of both retrievals, as similar correlations are found if no selection is done according to their brightness temperature or if different thresholds are used. Cloud optical depths inferred from satellite are on average about 40% smaller for the ice and 22% for the water cloud cases if compared to the pyranometer measurements. This is also shown by the slopes of the fitted linear relation. As the scatter is rather large and a similar magnitude of the uncertainties are expected for both retrievals, the ordinary least-squares bisector method is applied for the estimate of the linear model, which treats scatter in both x and y variables symmetrically and performs best for noisy datasets (Isobe et al., 1990).

5.4 Comparison of Retrieval Results

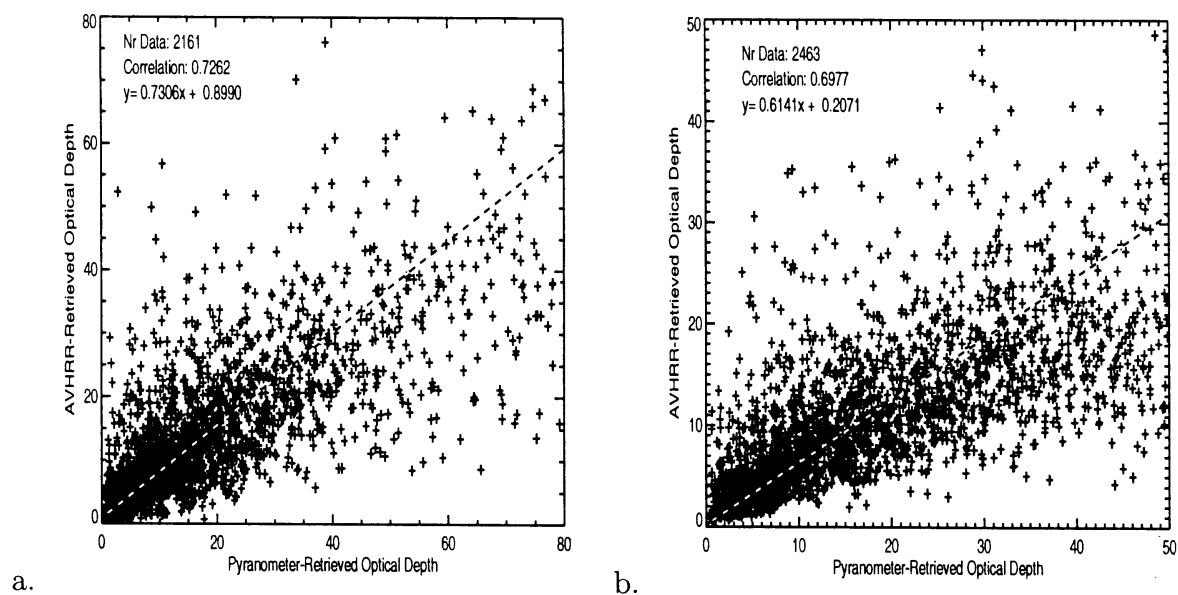


Figure 5.2: Comparison of cloud optical depths retrieved from broad-band solar irradiances at the surface and $0.63 \mu\text{m}$ TOA reflectances. (a.) Cases having a brightness temperature above 273 K, which are assumed to be water clouds. (b.) Cases having a brightness temperature below 260 K which are assumed to be ice clouds.

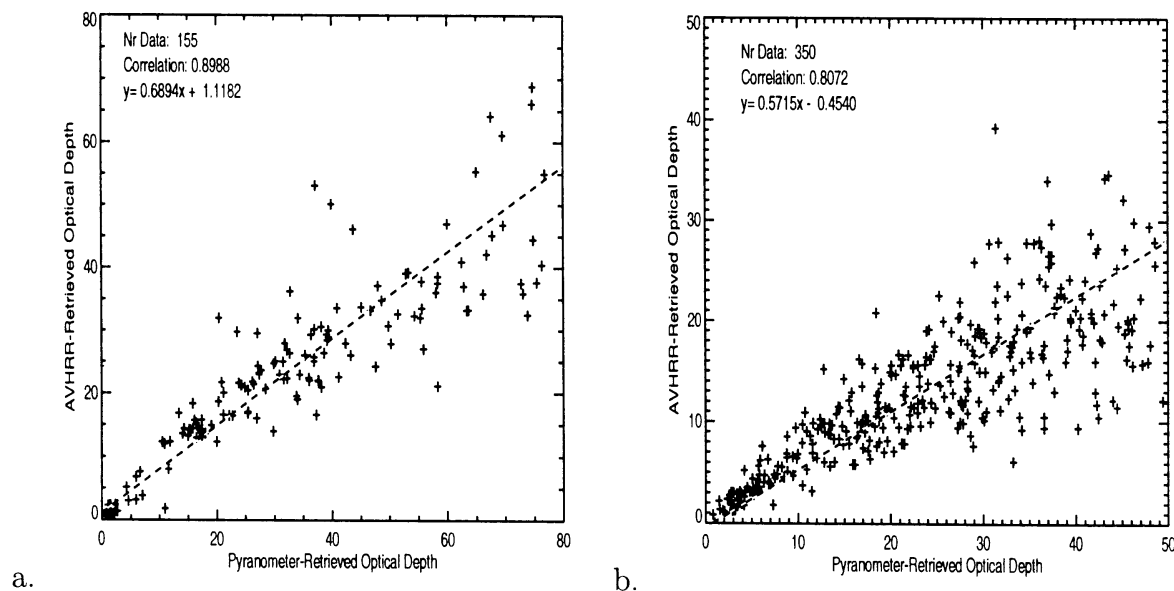


Figure 5.3: Same as Fig. 5.2, but restricted to cases with standard deviations of less than 3% in the $0.63 \mu\text{m}$ reflectance and less than 3°C in $11 \mu\text{m}$ temperature as calculated for a 10×10 pixel grid to ensure a good approximation to the model of a plane-parallel homogeneous cloud.

5. Cloud Optical Depth from Transmitted and Reflected Solar Radiation

Cloud inhomogeneity is not considered in the retrieval assumptions and is expected to lead to significant uncertainties and biases. Hence, a sub-selection of cases with a low horizontal variability is also studied. Thresholds in standard deviation of 3% in reflectance and 3 K in brightness temperature across the 10×10 pixels of the AVHRR image, as well as 5% for the four values of BAT measured during the 40 minute interval, are used as selection criteria. These cases are expected to fulfill best the assumption of a plane-parallel horizontally homogeneous cloud inherently made in 1D radiative transfer theory. The results for this subset is shown in Fig. 5.3. Significantly higher correlation coefficients of 0.90 and 0.81 for the water and ice cloud cases indicate a much better agreement of satellite- and pyranometer-derived cloud optical depths. This finding supports the hypothesis that a large part of the scatter is caused by 4D cloud structure.

The numerical values found for the correlation coefficient and the linear regression can change considerably, if slightly different selection criteria are used to restrict the range of viewing geometries and the variability. Hence, the exact magnitude of these values has to be regarded with due caution. The qualitative behavior described here, however, has been verified to be independent of the selection criteria used.

It is interesting to note that the bias present between the satellite and pyranometer results is larger for the cloud cases with low horizontal variability. Values of 28% and 46% are calculated for the water and ice cloud scenes. Hence, the bias is not caused by cloud variability detectable at the scales preserved by our datasets, but even seems to partly compensate for it.

At first sight, the larger correlation coefficient of 0.9 found for the homogeneous water cloud scenes as opposed to 0.8 for the homogeneous ice clouds could lead to the conclusion that the retrieval setup for water clouds performs better than the retrieval assuming ice clouds. However, this conclusion cannot be confirmed. Applying the water cloud retrievals to the scenes classified as ice clouds, and the ice cloud retrievals to the scenes classified as water clouds, the numerical values for the linear regression and the correlation coefficient are very similar to the ones obtained using the correct classification. Thus, it seems that the larger scatter present in the cases classified as ice clouds is caused by the morphology of these clouds, and not by the different assumptions made in the two retrievals. From a different perspective, this also means that no measurable gain in the agreement of ground-based and satellite retrievals is achieved by separating ice and water clouds.

Summarizing the results, both a significant scatter and bias are observed comparing cloud optical depths derived from reflected and transmitted solar radiation. While a reduction of the scatter is achieved by selecting cases having a low horizontal cloud variability, this even leads to a further increase in the bias. Similar biases have been reported previously in the literature (Barker et al., 1998; Min and Harrison, 1996).

5.5 Discussion

The results presented in the previous section clearly show that the comparison of cloud optical depths retrieved from transmitted and reflected solar radiation is of limited value for individual cases, as the scatter and bias introduce a large uncertainty in the results of the two methods.

Furthermore, without the ability to provide a thorough and consistent explanation of both scatter and bias, the error characteristics of both retrievals are not completely understood. This leaves open the possibility of significant unaccounted error sources hidden in the retrievals.

In this section, several different aspects of the retrievals are studied, which might be responsible for the observed behavior. In particular, the impact of systematic errors possibly present in the measurements and the effects of comparing the average of a spatial distribution to an average of a time series as obtained by a point measurement are investigated.

5.5.1 Monte Carlo Model of the Retrieval Process for the Error Analysis

Due to the non-linearity of the two retrievals, an analytical error treatment is impossible. Hence, a simplified Monte-Carlo simulation of the retrieval process is used instead to study the impact of different error sources on the retrieval results, and to quantify the resulting uncertainties. For this, a large number of samples of cloud optical depth are generated, which correspond to a Gamma-shaped probability distribution given by

$$P(\tau) = \frac{1}{\Gamma(\nu)} \left(\frac{\nu}{\bar{\tau}}\right)^\nu \tau^{\nu-1} e^{-\nu\tau/\bar{\tau}}, \quad (5.3)$$

where Γ is the Gamma function, $\bar{\tau}$ the mean cloud optical depth and ν a shape parameter. Satellite observations (Barker et al., 1996) and cloud-resolving models (Oreopoulos and Barker, 1999) indicate that this functional form is a good approximation for realistic distributions of cloud optical depth. This sample is transformed to corresponding values of transmissivity and reflectance based on the lookup tables calculated for the retrievals. Then, noise is added to the simulated observation with pre-defined characteristics, and the perturbed values are transformed back to a cloud optical depth. Comparing the initial and final set of cloud optical depths, the impact of instrumental uncertainties on the retrieval accuracy can be accurately quantified. A mean cloud optical depth of 25 and a shape parameter of 1.8 is used in all simulations. The corresponding distribution matches the distribution of cloud optical depths found for the water cloud cases of our dataset rather well. However, it has been verified that variations in either of the two parameters do not change our conclusions. To avoid problems arising from the limited resolution of the lookup tables, the retrieval functions have been interpolated to steps of 0.01 in cloud optical depth by cubic spline interpolation prior to their use. Linear interpolation is applied to link cloud optical depths on the one hand and BATs and bidirectional reflectances on the other hand, as it ensures the numerical exactness of the inversion process. An equal number of 100,000 samples each at 6 values of the cosine of the solar zenith angle, ranging from 0.3 to 0.8, are used in all simulations. This is done in order to represent the effects of different solar zenith angles as they occur within our dataset of observations. Only a nadir-looking satellite viewing geometry is considered, and a water cloud is assumed.

While this model neglects several parameters which are also of relevance to the real retrieval, it serves as a useful tool to study and understand the impact of different sources of uncertainty.

5. Cloud Optical Depth from Transmitted and Reflected Solar Radiation

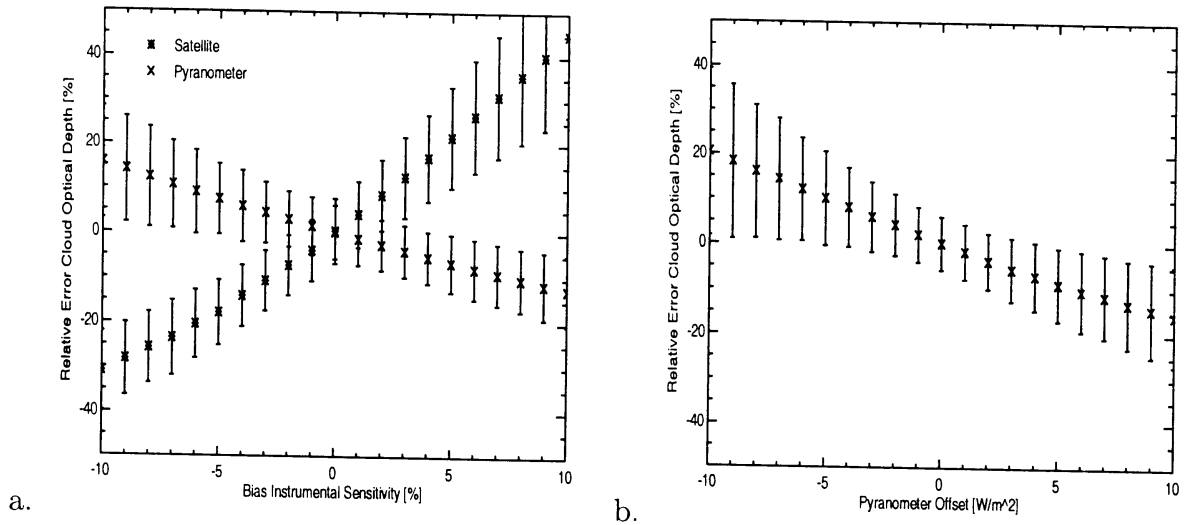


Figure 5.4: Bias of retrieved cloud optical depths resulting from systematic instrumental errors (a.) Mean relative bias resulting from erroneous sensitivities of the AVHRR instrument and the pyranometer (b.) Mean relative bias resulting from a systematic offset in the pyranometer measurements.

5.5.2 Measurement Uncertainties

The uncertainties of the instruments have been analyzed in detail in Ch. 3 and summarized in Sec. 5.2. Here, the impact of these uncertainties is quantified using the Monte-Carlo simulation of the retrieval process. The resulting bias and scatter in cloud optical depth for three different scenarios are presented in Fig. 5.4. The effects of calibration errors resulting in an erroneous sensitivity of the AVHRR and the pyranometer are shown in the left panel for a range of errors from -10 to 10 %. The right panel illustrates the retrieval errors resulting from a systematic pyranometer offset ranging from -10 to 10 W m^{-2} . An additional random relative uncertainty of 2 % for the satellite and 3 % for the pyranometer has been added together with the systematic errors to account for the effects of random retrieval uncertainties by a lower bound of the expected noise.

The result shows that the retrieval of cloud optical depths from AVHRR data critically depends on a high accuracy of the calibration. If our estimate of ± 5 % for the accuracy is correct, a systematic bias of ± 20 % in mean cloud optical depth is possible. In contrast, current estimates of the calibration accuracy of pyranometers of about 1 % would imply a resulting accuracy of mean optical depths within a few percent. However, a systematic negative offset of about 5 W m^{-2} during cloudy conditions found by Bush et al. (2000) will also lead to a mean overestimate of cloud optical depths by 10 %. Furthermore, realistic systematic errors in both measurements can also introduce random noise with a magnitude in the order of 5 – 10 %, as has been found by running the same simulations without the addition of a random noise term.

To provide a full explanation for the observed bias in cloud optical depths derived from transmitted and reflected radiation, both the systematic errors of pyranometer

and AVHRR need to be added up with close to their maximum expected range, which seems a somewhat unlikely explanation. The results of the studies of Bush et al. (2000) and Philipona (2002), however, present strong evidence that current pyranometer measurements severely underestimate the global irradiance. Hence, a substantial fraction of the bias can probably be attributed to shortcomings in the pyranometer measurements. No further information is available about the expected sign and magnitude of the bias of the satellite retrieval.

These findings clearly highlight the necessity of highly accurate measurements, if a good accuracy of retrieved cloud optical depths is desired. Especially the uncertainty in the calibration of the AVHRR has to be considered as a major limitation of the achievable accuracy. The stability of pyranometer measurements seems sufficient in principle, once the problems resulting from the thermal offset and from calibration are resolved, which are described in Ch. 3.

5.5.3 Violation of Retrieval Assumptions

The study of Barker and Li (1997) points out two fundamental shortcomings in the comparison of radiation quantities obtained at the TOA and the surface. Any interpretation of the measurements based on 1D radiative transfer theory implicitly assumes an atmospheric column with zero net horizontal flux across the vertical boundaries. The surface measurement is also assumed to be representative for the complete lower boundary, while it is a point measurement in reality. This shortcoming is compensated to some degree by choosing a sufficiently long period for averaging instead of using an instantaneous value. Nevertheless, the ground measurement has to be interpreted as a stochastic sample used for estimating the mean value of a spatial distribution.

No methods exist to measure the spatial mean irradiance for larger regions to quantify the magnitude of this effect. Two pyranometer datasets collected at De Bilt (WMO number 260, 52.10° N, 5.17° E) and Soesterberg (265, 52.13° N, 5.27° E) are compared instead to assess the representativeness of a point measurement for estimating the spatial mean. These two stations are separated by a distance of only 7.5 km. The comparison of the time series of transmissivities and irradiances averaged over a period of 40 minutes reveals a standard deviation of 9 % or 69 W m⁻². If a Gaussian distribution is assumed for the deviation of an individual measurement from the spatial mean, and the two pyranometer are treated as random and independent samples used for estimating this mean, statistical theory states that the variance of the two measurements will be two times the variance of the Gaussian. Based on these assumptions, 6.4 % or 49 W m⁻² are expected as standard deviation of the pyranometer-inferred values from the area-averaged transmissivity and irradiance. However, this interpretation is overly simplified for two reasons. Firstly, clear-sky measurements are included in this comparison, which will lead to an underestimate of variability if these values are used during cloudy conditions. If cloudy cases are selected by setting an upper limit of the irradiance corresponding to 80 % of the expected clear-sky irradiance (calculated as described in Ch. 4), the standard deviation of the two time series increases from 9 to 11 %. Secondly, irradiance measurements are strongly correlated at such small distances (Long and Ackerman, 1995). Without further knowledge about the spatial dependence of the

5. Cloud Optical Depth from Transmitted and Reflected Solar Radiation

correlation present in the irradiance field, the impact of spatial auto-correlation is difficult to assess. However, two arbitrary points located within the 10×10 pixel region used for the satellite analysis have a mean distance of 6.4 km , as has been determined by numerical integration. As this distance is close to the distance of the two stations, the standard deviation of the two time series is probably a reasonable first-order estimate of the deviation of individual measurements from the spatial mean.

The Monte Carlo simulation of the retrieval is used to provide a qualitative estimate of the impact of this variability. Adding a Gaussian noise term with an amplitude of 10% to the atmospheric transmissivities, a positive bias of 2% and a standard deviation of 20% is found for cloud optical depths retrieved from pyranometer measurements. This result indicates that the limited representativeness of the pyranometer measurement indeed introduces significant scatter and even causes a small bias.

At first sight, the deficiency in sampling seems to apply only to the pyranometer retrieval. However, the second criticism of Barker and Li (1997) has been neglected so far, which questions the assumption of zero net horizontal flux of radiation across the column boundaries. An analysis of this effect will be given in the next chapter. It is important to realize that both phenomena are caused by the spatial and temporal variability inherently present in the radiation and cloud fields. Hence, they should not be seen as two unrelated issues, but rather as two symptoms of the same fundamental shortcoming of the retrieval assumptions. Within 1D radiative transfer theory, the spatial and temporal variability of clouds is completely neglected. To overcome the shortcomings found in the comparison, the 4D structure of clouds needs to be accounted for in the retrievals. In particular, the effects of 3D radiative transfer and the statistical nature of the resulting observations need to be considered (Várnai and Marshak, 2001; Barker et al., 1996; Boers et al., 2000).

With these difficulties in mind, the choice of a 40 minute averaging period and a 10×10 pixel region for the comparison of the satellite and the pyranometer data can be motivated from a different perspective. The averaging period is sufficiently long to provide a reasonable sampling of the mean irradiance corresponding to the region used in the satellite analysis, and the region is chosen large enough to minimize the influence of horizontal photon transport.

5.6 Summary and Conclusions

In this study, a comparison of cloud optical depths derived from transmitted and reflected solar radiation has been presented. Consistent with the findings of previous investigations (Barker et al., 1998; Min and Harrison, 1996), the retrieval results show a negative bias having a magnitude of 20 to 45% for cloud optical depths inferred from reflected instead of transmitted radiation. Large deviations between both retrievals are found for standard conditions, resulting in a correlation of about 0.7. If selection criteria are imposed to limit cloud variability, this scatter is strongly reduced and the correlation coefficient increases up to 0.9. For these selected cases, a slight further increase in bias is found, indicating that cloud variability detectable at the spatial and temporal scales of our measurements are not the origin of the bias. The large scatter supports that the assumption of representativeness of a ground-based pyranometer measurement

5.6 Summary and Conclusions

for a simultaneous and collocated satellite observation is limited by the effects of cloud inhomogeneity and the resulting variability in the radiation field.

The use of different retrievals for ice and water clouds and the classification of scenes according to their infrared brightness temperature achieves no measurable gain in the agreement of retrieval results from reflected and transmitted radiation. However, due to the different phase functions of ice and water clouds, and in particular the difference in asymmetry parameters, a correct classification of clouds according to thermodynamic phase is nonetheless essential for the accuracy of the retrieval. This conclusion is illustrated by the large differences in the mean cloud optical depth and the bias found for the water and ice cloud retrievals.

Analyzing the sensitivity of the retrievals to instrumental errors, it seems possible that a large part of the bias is caused by systematic errors in the measurements, as the calibration accuracy of the AVHRR instrument is limited, and recent investigations cast serious doubts on previous estimates of the accuracy of pyranometer accuracy (Bush et al., 2000; Philipona, 2002). Hence, an improvement in the accuracy of both pyranometer and satellite measurements is one of the key requirements to be able to draw more definite conclusions about the implications of the observed bias for our understanding of cloud - radiation interactions.

A part of the scatter found between pyranometer and satellite derived cloud optical depths can be attributed to the incomplete knowledge of the parameters required as inputs to the radiative transfer calculations. However, the strong reduction of the scatter in cases with little variability strongly supports that a large part originates from the spatial and temporal variability of the solar radiance field. By comparing satellite and ground-based measurements, a spatial average of the bidirectional reflectance is related to a temporal average of a time series of irradiance measured at a single point in space. The comparison implicitly assumes that the temporal average is representative for the spatial mean corresponding to the region used for the satellite analysis. The limits of this assumption have been pointed out by Barker and Li (1997), based on results of a Monte Carlo radiative transfer code. They conclude that pyranometer measurements achieve only a poor accuracy in sampling the spatial mean of irradiance corresponding to the satellite grid. Experimental evidence for this conclusion is presented in the current study by comparing pyranometer measurements separated by approximately the mean distance of two arbitrary points within the region used for satellite analysis.

While this deficiency in sampling seems solvable at first sight by using several pyranometers, Barker and Li (1997) show that the underlying mechanisms are closely linked to horizontal photon transport and other 3D radiative transfer phenomena. Hence, the observed deviations reported in our comparison are of fundamental nature, as the static view of a cloud field assumed in the retrievals does not reflect all aspects of real clouds. A cloud field is not only characterized by its mean microphysical properties, but also by the temporal and spatial variability of these properties (Mandelbrot, 1982). These are strongly connected, as shown by Feijt and Jonker (2000). To assess the agreement of measurements obtained at different temporal and spatial scales, the variability of clouds described by the scaling properties of the microphysical parameters and the resulting observations need to be considered in the retrieval.

However, current cloud retrievals are based on the assumption that a single set of

5. Cloud Optical Depth from Transmitted and Reflected Solar Radiation

microphysical parameters can be assigned to a given observation. A Bayesian approach matches reality much better, because any given instrumental measurement can be caused by a large variety of cloud fields. By quantifying the likelihood of a given combination of microphysical parameters to lead to the observation, the complexity of the problem is not artificially reduced. Such an approach also allows the natural incorporation of the results of 3D radiative transfer theory into the retrieval process, instead of imposing an a-posteriori correction of the results.

Chapter 6

Retrieval of Solar Surface Irradiance from Satellite Measurements of the TOA Narrowband Reflectance

6.1 Introduction

The interaction of the atmosphere and the geosphere has significant influence on the Earth's climate system. It takes place mainly through the exchange of radiation, turbulent heat and moisture at the surface. Accurate knowledge of the surface radiation budget is of particular importance as it constitutes the forcing which drives the energy exchange processes. The World Climate Research Program (WCRP) has set the goal of deriving a global climatology of radiative fluxes with an accuracy of 10 W m^{-2} for monthly mean values averaged over regions of $250 \times 250 \text{ km}^2$ (Suttles and Ohring, 1986). Due to the limited and inhomogeneous coverage of meteorological measurement stations, a retrieval from satellite is the only feasible means to obtain this information.

The current study focuses on one particular component of the surface radiation budget, the downwelling solar surface irradiance (DSSI). Numerous algorithms have been developed for its estimation from satellite measurements (overviews are given by Schmetz, 1989; Pinker et al., 1995). Starting from a purely statistical relation of the observed radiance at the TOA and the measured irradiance at the surface, algorithms have become increasingly sophisticated by including more physical representations of the underlying atmospheric radiative transfer. However, most current algorithms are based on empirical relations. Two typical examples are the use of a statistically derived angular distribution model (ADM) of the outgoing radiation (the ADMs obtained from ERBE data described by Suttles et al., 1988, are widely used in the scientific community) and the conversion of narrow-band to broad-band radiative quantities (e.g. Li and Leighton, 1992). Statistical measures can be used to assess the quality of such relations. However, the lack of an underlying physical model hinders further insights into potential deficiencies. Furthermore, it is often unclear whether the conditions used for the derivation of such a relation are representative for the conditions of application. If this requirement is not fulfilled, significant biases can occur. An illustrative example is given by Chang and Li (2000), who find biases for retrieved values of the TOA broad-band

albedo as a result of relying on the ERBE ADMs.

In contrast, this study describes and validates a physical algorithm for retrieving the downwelling solar surface irradiance from satellite images of $0.63\ \mu\text{m}$ reflectance, which is applicable to both cloudy and clear-sky conditions and is based exclusively on calculations of a detailed radiative transfer model. Hence, all deviations can be attributed either to shortcomings in the model or incomplete knowledge of required model inputs. A priori, it is unclear whether the accuracy of this approach and the underlying radiative transfer model is better or even comparable to the accuracy offered by algorithms including empirical relations. On the other hand, the validation of the algorithm is also a validation of the underlying radiative transfer model. It can help to identify and correct technical and conceptual shortcomings in the model treatment and improve our general understanding of atmospheric radiative transfer. Hence, we consider this approach conceptually superior to empirical algorithms, because it is capable of achieving more accurate results in the long term.

For the validation of the algorithm, images of the NOAA-14 AVHRR are used. But it can easily be adapted to images acquired by the SEVIRI instrument on board Meteosat Second Generation (MSG, see EUMETSAT, 2001). As its data will be available at 15 minute intervals starting from March 2003, this algorithm can be applied to operationally derive estimates of the DSSI for applications relying on high temporal and spatial resolution.

Sec. 6.2 provides a short overview of the algorithm and the dataset used for its validation. In Sec. 6.3, results of the algorithm are compared with 6 years of measurements to quantify the accuracy of the scheme. The observed deviations are analysed in the discussion in Sec. 6.4. Finally, a summary of the study is given and possible improvements are outlined.

6.2 Retrieval Method and Dataset

It has been shown in Ch. 5 that variations in the cloud optical depth cause a strong modulation of the broad-band atmospheric transmissivity (BAT) and the TOA bidirectional reflectance. The relation between BAT and the reflectance has been used to present and compare two retrievals of cloud optical depth obtained from surface pyranometer measurements and from satellite images of the AVHRR instrument. From the point of view taken there, the cloud optical depth can be seen as a parameter linking these two quantities for an otherwise constant atmospheric state and viewing geometry. Hence, the relation of bidirectional reflectance and broad-band atmospheric transmissivity can be established if the dependency of each individual parameter on the cloud optical depth is known. Only a slight modification of the setup described in Ch. 5 is thus required to infer the DSSI from satellite measurements.

The large deviations of cloud optical depth obtained from both retrievals, which were noted in the study of Ch. 5, can lead to low expectations about the accuracy of such a scheme. However, the non-linear relation of radiative quantities and cloud optical depth, together with the limited sampling accuracy of pyranometer measurements for estimating a spatial mean, have been identified as the principle origin of these deviations. In contrast, Li et al. (1993) show that the solar irradiance at the surface and the

TOA are related linearly with reasonably high accuracy. Furthermore, they find little sensitivity of this relation on surface type, cloud optical depth and cloud type. Their conclusions motivate the hope that the algorithm outlined above is capable of achieving a good accuracy, even if the cloud optical depth calculated during the retrieval process represents only an effective value.

The same set of lookup tables of radiative transfer calculations used in Ch. 5 are also used as basis for the current retrieval. The lookup tables store values of both the $0.63\ \mu\text{m}$ bidirectional reflectance and the BAT as calculated for a wide range of satellite viewing geometries and solar zenith angles for 14 values of cloud optical depth. The dependence of BAT on changes in the vertical profile of water vapor is partly accounted for by using three sets of lookup tables with different values of the vertically integrated water vapor. A description of the lookup tables, the radiative transfer model used for their generation and the assumptions made in the calculations are given in Ch. 5 and Ch. 2. For a single satellite pixel, multilinear interpolation in the geometrical parameters and the vertically integrated water vapor is used first to extract the corresponding pairs of reflectance/transmissivity for a given measurement at all values of cloud optical depth included in the lookup tables. Then, the relation of reflectance and transmissivity is established by bicubic spline interpolation and the transmissivity corresponding to the AVHRR measurement is determined.

For the validation of the retrieval of DSSI, the dataset compiled for the study of Ch. 5 is used again. Measurements of global irradiance obtained by a dense network of 32 stations located throughout the Netherlands during the period from March 1995 until the end of the year 2000 are available together with simultaneous and collocated images of the $0.63\ \mu\text{m}$ bidirectional reflectance as acquired by the AVHRR on board NOAA-14. More details about the dataset can be found in the relevant sections of Ch. 5 and Ch. 3.

6.3 Validation

The results of the satellite retrieval of the DSSI are shown in Fig. 6.1 in comparison to values obtained from individual pyranometer measurements. To preserve the comparability with Ch. 5, the same averaging period of 40 minutes is used to obtain a corresponding pyranometer irradiance from the measured time-series. Instead of directly calculating a mean irradiance, the mean of the atmospheric transmissivity has been calculated and multiplied with the solar constant and the cosine of the solar zenith angle at the moment of the satellite overpass to regain an irradiance. The atmospheric transmissivity shows less dependence on the solar zenith angle than the DSSI. Therefore, this approach compensates at least for a part of the variability in irradiance induced by the change of the solar zenith angle during the 40-minute period. For the satellite retrieval, a grid consisting of 10×10 pixels located above the pyranometers is analyzed. Instead of calculating a mean irradiance and using this as retrieval input, as has been done in Ch. 5, the transmissivity is obtained for each individual pixel and then averaged and translated to a spatial mean of the irradiance. This approach yields a slightly better agreement of retrieval results with the measurements. However, as the change is hardly statistically significant, little influence of the algorithm's performance on satellite resolution is present. Only cases with a cosine of the solar zenith angle

6.3 Validation

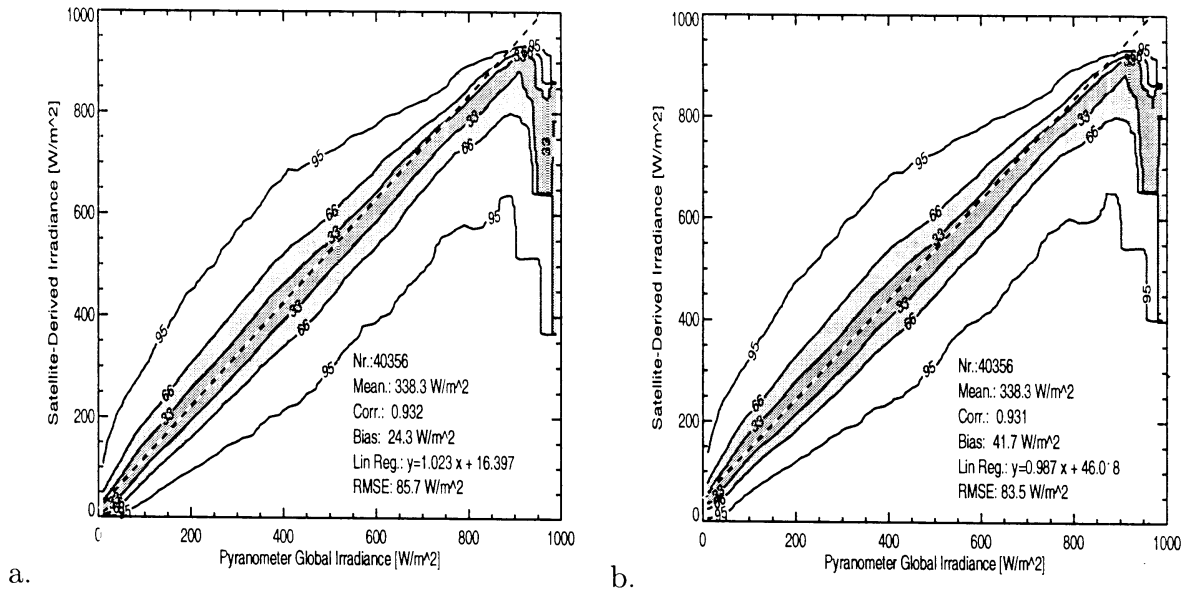


Figure 6.1: Comparison of satellite-retrieved downwelling solar surface irradiance with individual pyranometer measurements assuming that the cloud consists of (a.) water droplets and (b.) ice crystals. Shown are contours of the estimated distribution density of satellite-retrieved values given the pyranometer measurement (in %).

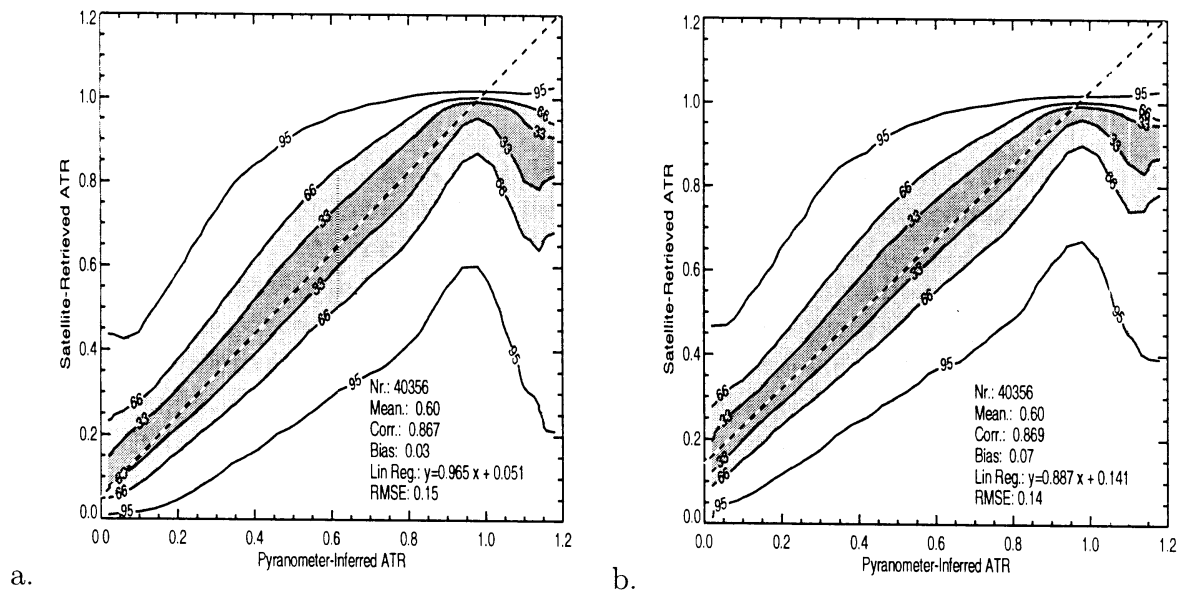


Figure 6.2: Comparison of satellite-retrieved and pyranometer-inferred atmospheric transmission ratio (ATR) assuming that the cloud consists of (a.) water droplets and (b.) ice crystals. Shown are contours of the estimated distribution density (in %).

exceeding 0.2 are included in the comparison, as large errors are expected at low sun elevations for both the radiative transfer calculations and the measurements. Apart from quality checks to exclude corrupted satellite data and pyranometer records, no further selection of data has been made, providing 40,358 individual measurements. In Fig. 6.1, the correlation, the overall bias, the parameters obtained by a linear regression to the data, and the root mean square error (RMSE) are also listed. The RMSE is calculated as the standard deviation of individual points from the regression line.

As the phase of the cloud particles is unknown, results are shown assuming that all clouds consist either completely of ice or water. Rather similar values are found for the correlation coefficient and the RMSE, having magnitudes of about 0.93 and 85 W m^{-2} , respectively. However, the bias of satellite retrieval and actual measurements is nearly twice as large if all clouds are assumed to consist of ice instead of water, increasing from 24 W m^{-2} to 42 W m^{-2} . Attempts to classify the phase of the cloud with the help of the infrared radiative temperature obtained by the AVHRR at $11 \mu\text{m}$ do not lead to a measurable improvement of the retrieval.

The explicit physical representation of cloud-radiation interactions as caused by the cloud optical depth can be viewed as the main advantage of the current retrieval algorithm over algorithms including empirical relations. To evaluate the quality of this representation, it is convenient to consider the atmospheric transmission ratio ATR, which is defined as

$$\text{ATR} = \frac{F_{SFC}^-}{F_{SFC,CS}^-}, \quad (6.1)$$

where F_{SFC}^- is the value of the measured DSSI and $F_{SFC,CS}^-$ is the DSSI expected for otherwise identical clear-sky conditions. For the purpose of the current study, the value of $F_{SFC,CS}^-$ has been obtained from the lookup tables as the result of the radiative transfer calculations for zero cloud optical depth. A discussion of the accuracy of this value is given in Ch. 4. Fig. 6.2 shows the distribution of retrieved and measured values of the ATR for the dataset assuming either a water or an ice cloud in the retrieval. The two plots clearly show a difference resulting from this assumption, which is also the origin of the different retrieval biases. The radiative transfer calculations assuming an ice cloud overpredict the ATR for larger cloud optical depths in comparison to both the calculations based on a water cloud and the measurements.

A further interesting feature visible in Fig. 6.2 is the occurrence of pyranometer-inferred ATR's larger than unity, respectively. As shown in Ch. 4, the radiative transfer model predicts values of the clear-sky DSSI which are generally a few percent larger than corresponding measurements. Hence, only a negligible number of these cases can be attributed to true clear-sky situations. Nevertheless, 6.5% of all pyranometer records are found to have an ATR exceeding unity. This fraction decreases somewhat for higher sun elevations, but not below 5%. Comparison with synoptic cloud reports identify the majority of these cases as broken cloud field situations, where significant net horizontal photon transport occurs due to reflection off the sides of clouds. These cases of enhanced DSSI cannot be explained within the concepts of 1D radiative transfer theory. Nevertheless, the cloud is typically located within the region used for the satellite analysis due to its larger spatial extent. Hence, the reduction of the spatially averaged irradiance caused by the cloud is correctly predicted by the model. This

6.3 Validation

leads to the decrease of the corresponding satellite ATR, if the pyranometer inferred value significantly exceeds unity. A similar behavior is also visible in Fig. 6.1 at very high values of the solar irradiance, which exceed the maximum clear-sky irradiance determined by the minimum observed solar zenith angle.

In principle, this phenomenon can be viewed as a symptom of the limited representativeness of a temporally averaged pyranometer time series for estimating a spatial mean irradiance. This shortcoming has been studied by Barker and Li (1997) with the help of 3D radiative transfer calculations and confirmed based on pyranometer data in Ch. 5. To reduce this effect, the average of all pyranometer measurements available for individual NOAA-14 overpasses are shown and compared to the average of the retrieval results in Fig. 6.3. A mean number of 28 pyranometer records is used for each satellite overpass. This averaging reduces the RMSE substantially to 33 W m^{-2} . Furthermore, the linear fit goes almost perfectly through the origin. The bias found between retrieval and measurements remains nearly constant at 7.2%. The small change is caused by the different weighting of individual measurements due to the variable number of stations used for the comparison with different satellite images. Only one value of the averaged ATR exceeds unity by more than two percent. The results of the comparison is only shown for the water cloud retrieval due to its better performance. For the ice cloud retrieval, a similar reduction in scatter is observed. However, the deficiencies of a larger bias and a larger constant term obtained by linear regression are still present after averaging. The fraction of cases where the averaged ATR exceeds unity is reduced to less than 1%.

It has already been stated in the introduction that the World Climate Research Project (WCRP) aims for an accuracy of 10 W m^{-2} for monthly mean radiative fluxes at a spatial resolution of $250 \times 250 \text{ km}^2$. The extension of the Netherlands in North-South and East-West direction is about 350 and 250 km, respectively, and the spatial distribution of meteorological stations is reasonably homogeneous as can be seen in Fig. A.1. Thus, the averaged irradiance of all meteorological stations corresponds to a spatial scale similar to the one mentioned by WCRP and will be treated as a representative example of such a grid box. Hence, the WCRP goal is used here to judge the performance of the present algorithm. Monthly averages of the retrieved and measured irradiance and corresponding values of the ATR are plotted in Fig. 6.4. Only months with a minimum of 300 individual measurements at a cosine of the solar zenith angle larger than 0.2 are included, a criterion fulfilled for 55 out of 70 months. Excluded were all December values and three November and three January averages. The rejection is only partly caused by the low sun during these months, but also by a much lower number of available images. For three other months, not enough satellite images were available from the archive due to technical failures. It is important to stress that these monthly averages consist of individual samples obtained at the time of NOAA-14 overpasses and represent no real monthly averages of the DSSI. Data provided by MSG will ensure a sufficient temporal sampling to overcome this limitation in the near future.

A comparison of Fig. 6.4 and Fig. 6.3 reveals interesting differences. A significant reduction in RMSE to 12 W m^{-2} is found, indicating that a further statistical cancellation of errors takes place for retrieval results of the different satellite overpasses. This quality almost achieves the goal set by the WCRP. However, the parameters obtained

6. Satellite Retrieval of Solar Surface Irradiance

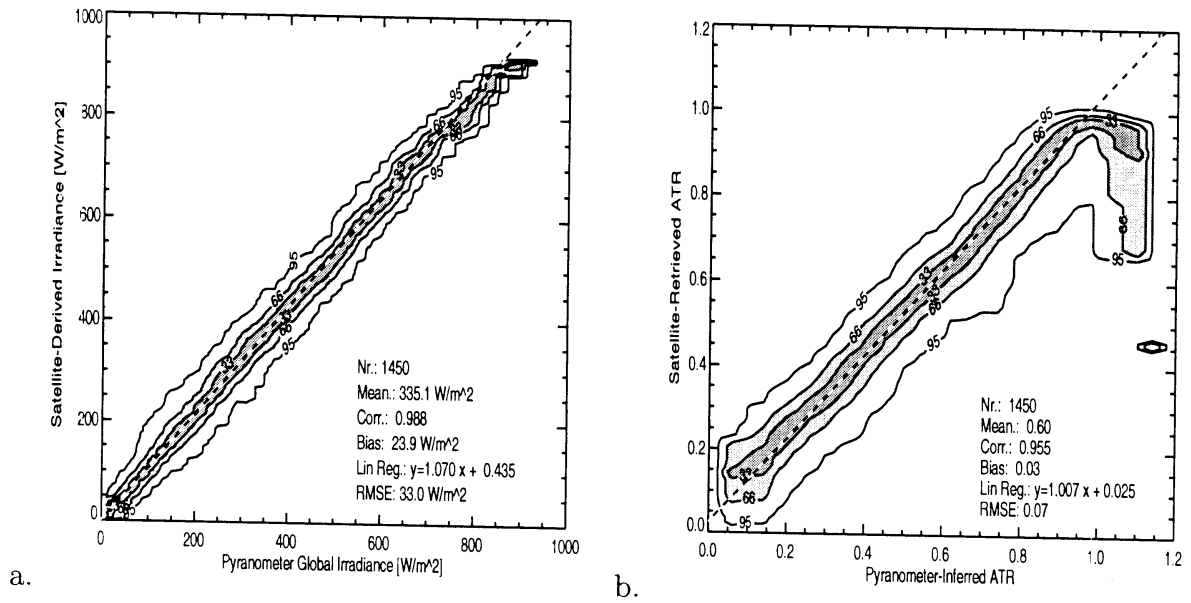


Figure 6.3: Comparison of (a.) downwelling solar surface irradiance and (b.) atmospheric transmission ratio as averaged for all pyranometer measurements available for a single satellite overpass and assuming water clouds. Shown is the estimated distribution density (in %).

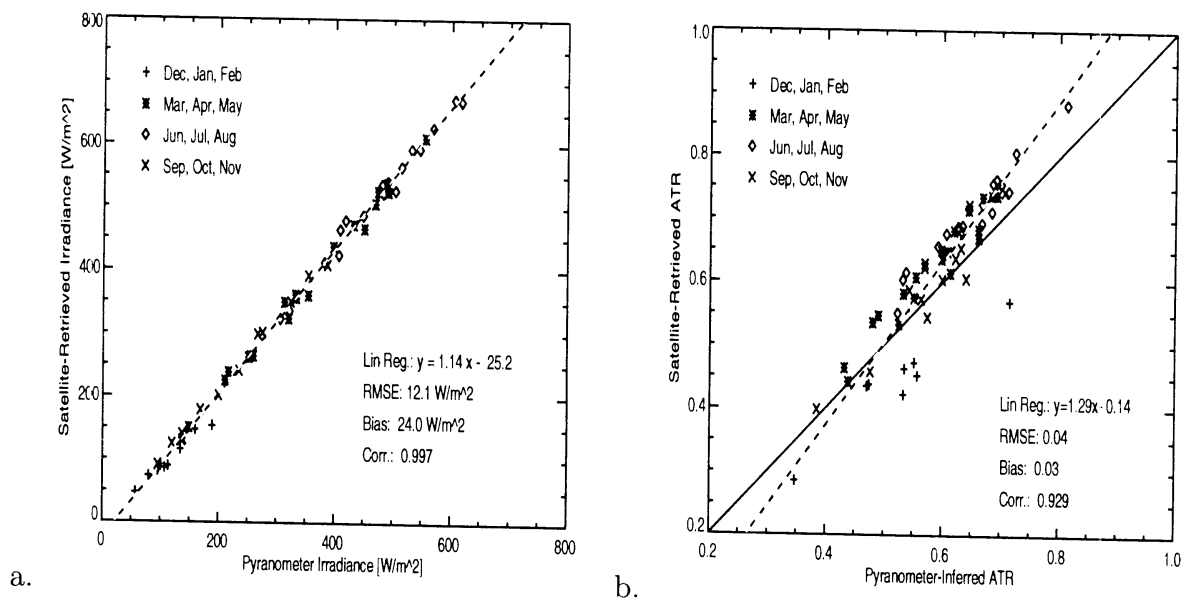


Figure 6.4: Scatterplot of satellite-retrieved and pyranometer inferred monthly averages of the (a.) downwelling solar surface irradiance and (b.) atmospheric transmission ratio assuming water clouds.

6.3 Validation

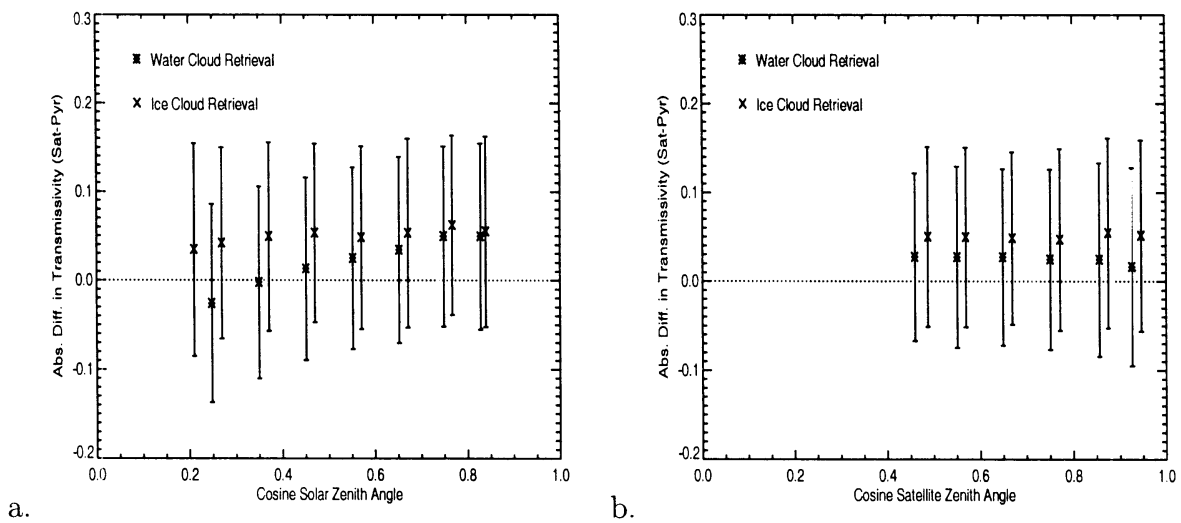


Figure 6.5: Dependence of retrieval performance on (a.) solar zenith angle and (b.) satellite zenith angle. Shown are the bias and the standard deviation for the water and ice cloud retrievals.

by the linear regression show a rather significant constant offset of -25 W m^{-2} and a slope of 1.14, which is a strong deviation from the desired value of zero and unity, respectively. The origin of this behavior can clearly be identified in Fig. 6.4.b, as the ATR removes part of the variability caused by different solar zenith angles and allows for a better comparison. During autumn and especially the winter months, the overall high bias of the satellite-retrieved irradiances versus the measurements is reversed and mean pyranometer irradiances actually exceed satellite-inferred values. Due to the low values of TOA insolation caused by the lower elevation of the Sun, the absolute values of the DSSI are also systematically smaller than for the other months, which causes the observed regression results. As this reversal of the bias is present as a systematic trend in the dataset, it provides a mathematical explanation for the deviation of the slope from unity. Possible physical mechanisms are analyzed in the discussion part of this chapter as a first step towards an explanation and an improvement of the retrieval.

From an application perspective, it is rather important that no undetected artificial dependencies are introduced by a retrieval. Otherwise, deviations could be erroneously attributed to a non-existent physical mechanism. As the diurnal cycle of radiative fluxes is an important signal, which is also strongly correlated with the solar zenith angle, the performance of the algorithm as function of μ_0 is shown in Fig. 6.5. As a measure, the absolute difference of the retrieved and measured BAT is used, and results of the ice cloud and water cloud retrieval are shown. The second parameter studied in the figure is the cosine of the satellite zenith angle. Both bias and standard deviation of both quantities are plotted, as the expected magnitude and the mean value of the retrieval error are of interest. From Fig. 6.5.a, it can be seen that the positive bias in BAT of the water cloud retrieval diminishes with decreasing cosine of the solar zenith angle and even turns into a slight negative bias below a value of about 0.35. No such dependence

is found for the ice cloud retrieval. Also, no strong change in bias is detectable for both retrievals as a function of the satellite zenith angle. Furthermore, the standard deviation remains reasonably constant for both retrievals and the full range of satellite and solar zenith angles, indicating that the performance is not significantly affected by a low sun or large satellite viewing angles. This conclusion is particularly relevant for application of the algorithm to data from MSG or other geostationary satellites due to the strong dependence of satellite zenith angle on latitude, which has a value of about 60 degrees for the Netherlands.

6.4 Discussion

The results presented in the previous section clearly show that the presented algorithm is capable of accurately capturing the influence of clouds on the DSSI. Nevertheless, a number of discrepancies are evident in the comparison of retrieval results with pyranometer measurements. While an empirical correction can be applied to remove biases, it seems desirable to identify the underlying physical reasons and to resolve potential shortcomings in the measurements and the radiative transfer model. A number of possible explanations for the observed discrepancies will be discussed in this section as a first step towards this goal. Special attention will be given to the large scatter present in the comparison of individual pyranometer records and retrieval results.

6.4.1 Radiative Transfer Calculations

The quality of the radiative transfer calculations is the main criterion determining the accuracy of the retrieval of DSSI from satellite data. However, several inputs to the RTM have to be estimated. For an overview of these parameters and the resulting uncertainties, see Ch. 5.

Realistic values of both the broad-band and $0.63\ \mu\text{m}$ narrow-band surface albedo are important prerequisites, as severe errors in the BAT are possible, if deviations become too large. Li et al. (1993) avoid this requirement by retrieving the net irradiance at the surface instead. For this investigation, the decision has been made to infer the downwelling irradiance as primary product for a number of reasons. Measurements of the upwelling solar irradiance are available only at two sites. Thus, an estimate of the surface albedo cannot be avoided in most cases for the present dataset. The representativeness of a small-scale surface albedo derived from the upwelling irradiance typically measured at 2 meters height is questionable for estimating its influence on radiation reflected by clouds over much larger spatial scales. Furthermore, significant biases in effective and true cloud optical depth are expected if a wrong surface albedo is assumed, so the advantage of a physical representation of the cloud-radiation interactions in the radiative transfer model would be lost. It is important to realize, however, that the approach presented here relies on a sufficient contrast between clear-sky and cloudy reflectance, a criterion which is fulfilled for the location of the meteorological stations considered in the current study in the absence of snow on the surface.

The assumption of an isotropic and constant surface albedo for all stations is a major limitation of the scheme in its current form. Due to the variability introduced by

different surface types, seasonal changes in the state of vegetation, and the dependence on solar zenith angle, errors of several percent are expected to occur either in form of random noise or even as a bias. Much larger errors are possible if the surface is covered by snow, an aspect which has been ignored for the current study due to the rare occurrence of snow in the Netherlands.

Maps of the surface albedo are available operationally on a global scale and can thus be used to generalize our algorithm to arbitrary locations. A possible source is e.g. the MODIS instrument (Salomonson et al., 1989), which derives both narrow-band and broad-band surface albedos together with the corresponding BRDFs. An alternative is a derivation from AVHRR or SEVIRI data during cloud-free situations (Csiszar and Gutman, 1999). However, the accuracy of such retrievals are significantly lower due to a larger calibration uncertainty and the smaller number of spectral channels available.

Another important aspect of the retrieval is the correct representation of cloud optical properties in the radiative transfer calculations. As ice crystals and water droplets have rather different phase functions, the correct choice of cloud phase was initially expected to lead to a significant improvement of retrieval accuracy. However, attempts to classify the phase by thresholds of the $11\ \mu\text{m}$ cloud top temperature have not lead to any difference in performance. Fig. 6.2 also shows that the water cloud assumption works better for cases with a small ATR, which generally correspond to clouds with large optical depths. At first sight, this is somewhat surprising, as most of these cases have a cloud top temperature which is $20 - 30^\circ\text{C}$ below the freezing point. Thus, the cloud top is likely formed by ice crystals. However, these clouds typically have also a rather large vertical extend. A significant fraction of the optical depth might be attributable to water droplets and thus cause the better agreement of the water cloud retrieval and measurements. Detection of the phase of the cloud is required to further investigate this issue (Jolivet and Feijt, 2002). Unfortunately, the measurements of $1.6\ \mu\text{m}$ bidirectional reflectance needed for this method are not available for the NOAA-14 AVHRR instrument.

Even if a reliable classification of cloud phase is possible, several unsolved aspects remain. With current satellite data, it is impossible to identify satellite pixels containing mixed-phase or multi-layered clouds with sufficient accuracy. Representative optical properties for ice clouds are still subject of debate (Doutriaux-Boucher et al., 2000). And last but not least, effects of cloud inhomogeneity and 3D radiative transfer are completely neglected in the scheme in its current form.

6.4.2 Instrumental Accuracy

The AVHRR measurements are affected by the limited accuracy of the instrumental calibration, which is estimated to be about 5%. The pyranometer records should have an uncertainty of about 3% for hourly averages of the irradiance according to the classification of the instruments given by WMO (1996). However, recent investigations of the accuracy of pyranometers find significant shortcomings and inconsistencies in the measurements (Bush et al., 2000; Cess et al., 2000; Philipona, 2002). Their results indicate that the real quality is probably significantly lower. A systematic underestimate of measured irradiance in the range of 3 – 5% or even more seems likely (see Ch. 3

and Philipona, 2002). As the origin of these errors is only partly understood, it is impossible to estimate the effects of this error on the data.

The combination of the uncertainties of pyranometer records and satellite calibration is sufficient to completely explain the high bias of 7% of the retrieval results in comparison to the measurements. This is also a further confirmation of the results described in Ch. 5, where it was concluded that the positive bias of cloud optical depths inferred from pyranometers instead of satellite is possibly caused by instrumental errors. The limited calibration accuracy of the satellite images and the recently found shortcomings in pyranometer measurements can thus be seen as the largest obstacle to a further evaluation and improvement of this scheme and the underlying RTM. In particular, no definite conclusions are possible about mechanisms whose magnitude are significantly smaller than the instrumental uncertainties until these issues are resolved. This includes effects like the impact of cloud phase and biases due to 3D radiative transfer.

Several satellites are now available, which have highly accurate calibrations of short-wave channels based on on-board calibration sources. Their data can be used either directly or indirectly by transferring the calibration to a different satellite. However, the intercalibration necessarily leads to a degraded accuracy. In addition, a new generation of pyranometers and an improved calibration setup will become operationally shortly, which address several of the shortcomings of previous pyranometers and should significantly improve the accuracy of measurements of the DSSI. Based on this instrumental data, a reevaluation of the issues found in the present study seems desirable to be able to separate the effects of instrumental shortcomings and retrieval deficiencies.

6.4.3 Effects of Variability

For the validation of the retrieval, a spatially averaged value of the DSSI corresponding to 10×10 pixels (or approximately a 150 km^2 region) has been compared to a 40 minute average of a time series as measured by the pyranometer. Adapting this approach, the assumption is inherently made that both quantities are representative for the other type of measurement. As shown by Barker and Li (1997) and in Ch. 5, large deviations can result from this assumption for individual cases. The origin of these deviations is the spatial and temporal variability of the radiation field caused by changes in cloud structure. Temporally averaged pyranometer measurements have to be considered as a statistical samples of the spatially averaged surface irradiance corresponding to the area used for the satellite analysis. This aspect of the problem can be minimized by decreasing the spatial region, which leads to a reduction of the expected sampling error. However, the effects of horizontal photon transport will then limit the correspondence of TOA and surface measurements. The impact of the variability in irradiance is illustrated in Fig. 6.6 with help of pyranometer records obtained at the two stations De Bilt and Soesterberg. They are only separated by 7.5 km, which is close to the mean distance of two arbitrary points located within the area selected for the satellite analysis. 40-minute averages of the DSSI and the ATR inferred for the two stations are shown Fig. 6.6. It is interesting to note that several features visible in these plots are quite similar to features present in Fig. 6.1 and Fig. 6.2, suggesting that the underlying effects causing the deviations are possibly closely related.

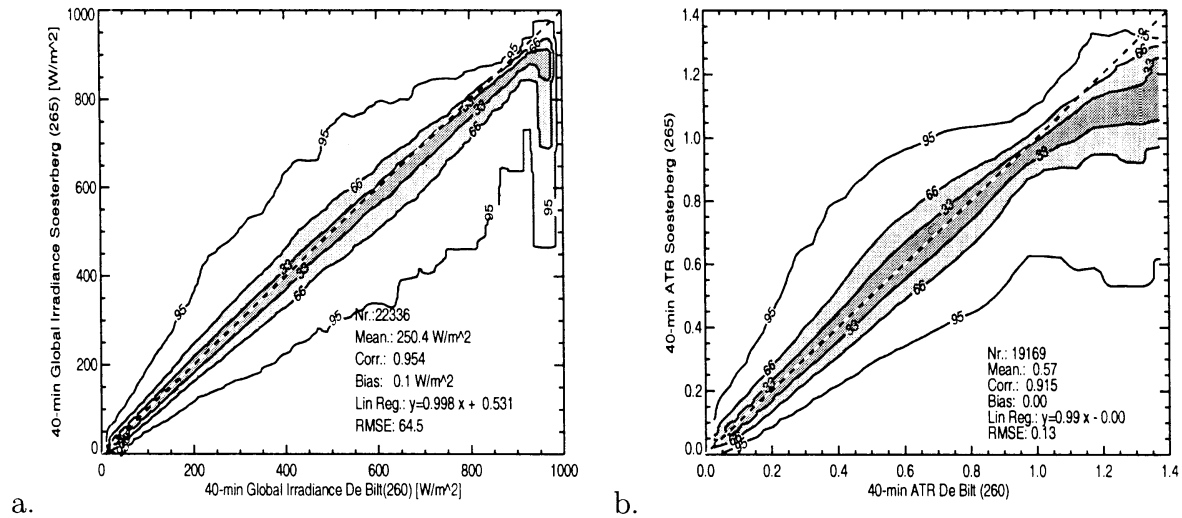


Figure 6.6: Difference in (a.) downwelling solar irradiance and (b.) atmospheric transmission ratio (ATR) measured by pyranometers at the stations De Bilt (260) and Soesterberg (265), which are separated by a distance of only 7.5 km. Shown is the estimated distribution density (in %) for one measurement given the other one.

In principle, the mechanism outlined above needs to be accounted for in a quantitative estimate of retrieval performance, as it is completely independent of retrieval deficiencies. To achieve this goal, the errors incurred by the effects of spatial sampling, temporal averaging and horizontal photon transport need to be quantified. A detailed analysis of the spatial and temporal scaling properties of the DSSI is required for this, which is beyond the scope of the current study. A rough estimate for the sampling error has been given in Ch. 5 under simplified assumptions. The two stations considered in Fig. 6.6 are treated as statistically independent samples of the spatially averaged mean irradiance. Furthermore, retrieval errors and the deviations of pyranometer records from the spatial mean are assumed to be given by normal distributions, which makes Gaussian error propagation applicable. It states that the combination of two error sources with standard deviations SD_1 and SD_2 is given by

$$SD = \sqrt{SD_1^2 + SD_2^2}, \quad (6.2)$$

where SD is the combined standard deviation. The numerical values are likely inaccurate due to violations of some of the assumptions. Nevertheless, they should provide a reasonable first-order estimate.

The RMSE of 69.1 W m^{-2} found in Fig. 6.6 corresponds to a normal distribution with a standard deviation of $(69.1/\sqrt{2}) \text{ W m}^{-2} = 48.9 \text{ W m}^{-2}$. The factor of $\sqrt{2}^{-1}$ is introduced by estimating the deviation of any individual sample from the spatial mean from the difference of two samples. The mean scatter of 86 W m^{-2} found in Fig. 6.1 for the water cloud retrieval is thus composed of the sampling error and the retrieval uncertainty, which is determined to be 71 W m^{-2} by applying Eq. 6.2. As the squares of the individual errors have to be added, about a third of the observed

RMSE is attributable to an inaccurate sampling of the spatial mean irradiance by the pyranometer. An average number of 28 stations are included in the comparison shown in Fig. 6.3. Then, the RMSE of 33 W m^{-2} originates from a retrieval error of 31.7 W m^{-2} and a remaining sampling error of 9.2 W m^{-2} . Thus, the retrieval error dominates the magnitude of the total error for this analysis. Averaging over all available stations thus achieves the goal of minimizing sampling errors. This conclusion is also true for the monthly averages, where a much larger number of at least 300 stations is combined.

Two interesting observations can be based on these values. Firstly, by averaging the irradiance available for all stations, the influence of sampling errors is strongly reduced and random retrieval uncertainties dominate the RMSE found in Fig. 6.3. Secondly, the random retrieval uncertainty is also strongly reduced by averaging measurement results obtained at several stations available for a satellite overpass. Errors resulting from shortcomings in 1D radiative transfer calculations are expected to be highly correlated for individual satellite scenes, because the cloud structure and atmospheric conditions are expected to be reasonably homogeneous for the spatial extent of the measurement network. Hence, the observed reduction suggests that a large fraction of the retrieval error is also caused by uncertainties introduced by cloud variability, such as 3D radiative effects.

An important consequence of these findings is the dependency of the retrieval quality on the region and the time interval chosen for averaging. Hence, any intercomparison of satellite retrievals of the DSSI must be made using similar scales. Averaging periods ranging from 10 minutes to an hour are studied here in comparison to regional scales ranging from approximately 5 km^2 to about 400 km^2 as given by grids of 2×2 to 16×16 satellite pixels. A reduction of RMSE and an increase of correlation is observed for longer averaging periods and larger retrieval regions. Minimum and maximum values of 0.872 and 0.944 are found for the correlation and 120 W m^{-2} and 78 W m^{-2} were calculated as corresponding RMSE for retrieved values of the DSSI. This finding clearly shows that the radiation field is strongly autocorrelated in space and time at the considered scales.

The large number of cases having an ATR exceeding unity has already been mentioned in the previous section. It can be seen as a consequence of the channelling of radiation from vertical columns with high optical depth to columns having smaller optical depths (Coley and Jonas, 1996). The underlying mechanism is the horizontal transport of photons taking place in inhomogeneous atmospheres. For the cloud optical depth retrieval presented in Ch. 5, a value of the DSSI below the expected clear-sky value is required. Hence, cases having an enhanced value of the DSSI are rejected even though the irradiance is altered by a cloud. In particular, the retrieval assumptions do not account for the fact that these occurrences of enhanced DSSI are compensated by an apparently missing amount of radiation underneath the cloud, if measurements are compared to 1D radiative transfer calculations. To quantify this effect, the change of mean irradiance due to this subselection of data is studied. If only cases having an ATR less than unity are considered, the mean irradiance of all pyranometer measurements is reduced by 13.0 W m^{-2} . If the mean of the satellite retrieval results is calculated for same cases, a reduction of only 7.1 W m^{-2} is obtained, because the retrieval is less susceptible to horizontal photon transport due to the larger spatial extent of the mea-

6.5 Conclusions and Outlook

surement. Hence, 5.9 W m^{-2} of mean irradiance or a corresponding 0.8% in mean BAT are lost by the subsampling of cases, if measurements with an enhanced irradiance are rejected. Horizontal photon transport is thus a mechanism which can lead to an overestimate of pyranometer retrieved cloud optical depths for the method used in Ch. 5. However, the magnitude of the resulting bias is expected to be much smaller than the bias found in Ch. 5. While the impact of horizontal photon transport is easiest to detect in cases having an ATR above unity, it is important to stress that it generally occurs in all cloudy situations.

6.5 Conclusions and Outlook

A physical algorithm for the retrieval of the downwelling solar surface irradiance has been presented, which explicitly accounts for variations of cloud optical depth and column water vapor. Validation with a six year dataset of pyranometer measurements obtained at 32 stations located throughout the Netherlands reveals a positive bias of 7% for the retrieval results and a standard deviation of 85 W m^{-2} for individual measurements. Pyranometer and satellite data have been averaged to correspond to temporal and spatial scales of 40 minutes and 150 km^2 , respectively. If the retrieved irradiances are averaged for all stations available for an individual satellite overpass, a reduction of scatter to 33 W m^{-2} is found. For monthly averages of the mean irradiance at all stations, the standard deviation decreases even further to 12 W m^{-2} .

It is shown that a significant part of the scatter cannot be attributed to retrieval shortcomings, but originates from the variability in the solar irradiance caused by cloud inhomogeneity and partial cloud cover. This variability limits the representativeness of a temporally averaged pyranometer time series for inferring a spatial mean of the irradiance. While the exact magnitude of this effect is difficult to quantify, a first-order estimate suggests that it causes about a third of the total scatter present in the comparison of individual pyranometer measurements and collocated satellite results for the present comparison.

This finding has important implications for the validation of similar retrievals and a possible extension of the current scheme. A large number of cases is required to reliably quantify the performance due to the size of the scatter. This makes the evaluation of the impact of modifications a difficult task. Furthermore, results need to be compared at the same averaging scales and under climates with similar cloud variability to be able to assess differences in performance.

Several questions arising from this study require further investigation. The high bias of satellite-retrieved values is consistent with several other studies concluding a systematic overestimate of modeled versus measured DSSI (Cess et al., 1995). Likely explanations include an underestimate of atmospheric absorption in current radiative transfer models (e.g. Ramanathan et al., 1995) or the presence of systematic biases in the pyranometer measurements (see Bush et al., 2000; Cess et al., 2000; Philipona, 2002, and Ch. 3)). These issues are currently the subject of detailed investigations due to their implications for our understanding of atmospheric radiative transfer and climate research (Ramanathan, 1987). A solution of these problems is required before processes of smaller magnitude can be studied and quantified, as e.g. caused by 3D radiative

transfer.

A second interesting result of the study is the dependence of the bias on the solar zenith angle, if a water cloud is assumed for the retrieval. Possible explanations include 3D effects in radiative transfer, a larger fraction of ice clouds during winter months, which contribute most of the cases having a low sun elevation, or instrumental errors. Unfortunately, the data available is insufficient to identify the origin conclusively.

An extension of the current retrieval based on established scientific algorithms is possible with minor effort. The incorporation of a cloud detection algorithms as pre-processing would allow the use of a separate and specifically adapted algorithm for estimation of the DSSI during clear-sky situations and likely improve the accuracy (Frouin et al., 1989). Reliable cloud detection would also allow the derivation of maps of the surface albedo (e.g. Csiszar and Gutman, 1999), which are required for a generalisation of the retrieval to larger regions with no a priori knowledge about the surface albedo. A more realistic cloud characterization in the radiative transfer calculations is also possible and is likely to improve the accuracy of the scheme. Based on the $1.6\ \mu\text{m}$ channel available on NOAA-16 and MSG, the retrieval of the cloud droplet size and a discrimination of water and ice clouds is possible (Jolivet and Feijt, 2002). The cloud top height can be estimated from the $11\ \mu\text{m}$ radiance. However, the inclusion of additional parameters in the retrieval also requires a strong increase in the size of the lookup tables and the time required for their computation. Possibly, a different approach has to be adopted to be able to deal with this additional information.

Chapter 7

Evaluation of Model Predictions of Cloud Parameters and the Solar Radiation Budget

7.1 Introduction

A realistic representation of cloud-climate interactions in General Circulation Models (GCMs) is an important prerequisite for our ability to accurately predict the response of the climate system to anthropogenic and natural forcings (Cess et al., 1990). Nevertheless, many processes and feedbacks related to clouds are not adequately reproduced in the current generation of GCMs and cause large uncertainties in climate predictions (IPCC, 2001).

The reason for these shortcomings is the complicated and non-linear nature of cloud processes, their dependence on large-scale atmospheric motion and their interaction with convection and radiation. These processes need to be parameterized correctly for accurate model forecasts of cloud properties. However, our knowledge about these processes is still too limited to develop accurate formulations. Furthermore, variability occurring at spatial scales below the model resolution needs to be accounted for by sub-grid parameterizations, which limits the achievable accuracy.

Progress is only possible if the remaining shortcomings of current models can be identified by comparisons with observational data. Unfortunately, the information available from current measurements often covers only a limited number of cloud parameters, has large uncertainties, or is ambiguous. For example, the statistical properties of the vertical profiles of cloud cover are known only with limited accuracy for the middle troposphere, because the field of view is often blocked for observations from ground or space by under- or overlying cloud layers. The task of model evaluation is further complicated by the large variability of clouds and the limited representativeness of surface measurements for grid-box mean quantities, which often results from the much smaller spatial scale of the measurements.

The objective of the current study is the evaluation of a multi-year time series of model output generated by the single column version of RACMO (Regional Atmospheric Climate Model, Christensen et al., 1996) with focus on cloud parameters and the solar

7.2 Model Setup

radiation budget. The length of the period is expected to be sufficient to allow reliable conclusions about model climatologies. For an assessment of the model performance, not only climatological means of relevant parameters are important, but also their statistical distributions. In principle, the model errors of physical quantities for different averaging periods are of interest, as this characteristic will influence the error propagation to other variables. However, the present investigation is restricted to a comparison of mean values and their variability for the full time period, in addition to an analysis of the model performance on a case-by-case basis.

Observations collected within a small region of about $60 \times 60 \text{ km}^2$, which is a typical size for a model grid box, are used for the comparison. It contains two automated and six synoptic stations operated as part of the meteorological measurement network of KNMI. These stations provide pyranometer measurements of the downwelling solar radiation at the surface in combination with synoptic cloud reports. Due to the large number of stations, difficulties arising from the limited representativeness of a point measurement for estimating the spatial mean of a model grid box are minimized, as they are e.g. encountered in Ch. 5 and Ch. 6. Furthermore, atmospheric profiles obtained from close-by radiosonde launches are available for an evaluation of the model atmosphere.

The study is structured as follows: First, a short overview of the model and the setup used for generating the output dataset is given. Then, model-predicted fields of water vapor are evaluated with help of the radiosonde data because it is a central quantity for the determination of cloud processes. In Sec. 7.4, synoptic reports of cloud cover are compared to model predictions, both for the total atmosphere and the synoptic classification of low, medium and high-level clouds. Measured and modeled values of the transmission of solar radiation through the atmosphere are studied in Sec. 7.5 to identify potential shortcomings in the model treatment of cloud-radiation interactions. The implications of the observed model deficiencies are discussed, and a summary of the results and conclusions are given in Sec. 7.6.

7.2 Model Setup

For the current investigation, a single column model (SCM) based on RACMO is used (Christensen et al., 1996), which is denoted as SCR in the following. RACMO and its single-column derivative are research models developed at KNMI in collaboration with the Danish Meteorological Institute. They combine the adiabatic part of HIRLAM (Gustaffson, 1993) with the physics package included in the ECHAM4 GCM (Roeckner et al., 1996).

The SCR runs used to create the output for the current study are initialized at 12 UTC each day and cover a 36 hour forecasting period. For the lateral boundary conditions of the SCR, time series of dynamical forcings calculated by the full 3D version of RACMO for the Cabauw grid-box (51.89°N , 4.82°E) are employed, which are generated and archived as part of standard operations. The 3D forecast runs are conducted with a horizontal resolution of 55 km and with 19 hybrid levels in the vertical. Eulerian time stepping is used with a 5-minute step size. The model domain of the forecast spans 92×81 grid points covering Western Europe. The atmospheric fields used for the model initialization and the conditions at the lateral boundaries of the domain are taken from

analyses generated operationally at the European Centre for Medium-Range Weather Forecasts (ECMWF) by their Integrated Forecast System. Prognostic surface and soil variables, and prognostic cloud water are initialized from the previous forecast.

A short overview of the description of relevant physical processes is given here, which is applicable to both SCR and the full 3D version of RACMO. Convection is parameterized based on the bulk mass flux concept of Tiedtke (1989) with modifications of entrainment and detrainment suggested by Nordeng (1994). This scheme also determines the microphysical properties of convective clouds. The treatment of stratiform clouds follows Sundqvist (1978). Cloud fraction is diagnosed as a non-linear function of grid-mean relative humidity if a pre-set threshold is exceeded (Sundqvist et al., 1989). Random-maximum overlap of cloud layers is assumed to obtain the total cloud cover. The amount of total cloud water is a prognostic variable. The ratio of liquid and ice water is diagnosed based on temperature below the freezing point. Shortwave radiative fluxes are calculated with the scheme developed by Fouquart and Bonnel (1980). It is a two-stream algorithm considering two spectral intervals with limits at 0.2, 0.68 and $4.0\ \mu\text{m}$. The spectroscopic information on gas absorption used in this scheme has been updated for the ECHAM4 model based on the 1991 release of the HITRAN database (Rothman et al., 1992) and includes all relevant absorbing gases in the solar spectral region. Optical properties of cloud particles are derived from Mie calculations, which have been weighted by the Planck function corresponding to the Sun's radiative temperature. A polynomial fit is used to parameterize the functional form for different effective radii of the prescribed droplet size distributions for both liquid and ice particles.

Two significant modifications of the model have been made for the SCR runs for this study. The aerosol optical depth prescribed by ECHAM4's model climatology has been scaled to a value of 0.1925 at 550 nm to conform to the observed climatological mean value reported at De Bilt, the Netherlands by Stammes and Henzing (2000). This reduces the original value of aerosol optical depth by more than a factor of two and leads to strong differences in mean solar radiative fluxes. In particular, the solar irradiance downwelling at the surface during clear-sky conditions increases strongly, as the total atmospheric transmissivity is increased by several percent. Also, the modified treatment of water vapor absorption proposed by Bennartz and Lohmann (2001) is included in the radiation scheme, which accounts for recent updates of absorption line parameters of water vapor published by Giver et al. (2000).

With these two updates, a positive bias of about $25\ \text{W m}^{-2}$ is found between model-predicted and measured irradiance during clear-sky conditions, as is described in Ch. 4. However, recent investigations of pyranometer measurements (Bush et al., 2000; Cess et al., 2000; Philipona, 2002) suggest that this bias is probably attributable to instrumental shortcomings.

For the comparison, SCR runs covering a four-year time period starting in January 1997 and ending in December 2000 are considered.

7.3 Water Vapor

The amounts of cloud water and water vapor are fundamentally linked through the processes of condensation and evaporation. Furthermore, water vapor is the gas causing

7.3 Water Vapor

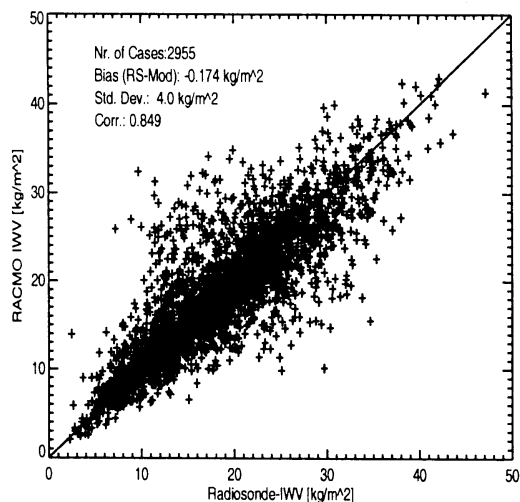


Figure 7.1: Comparison of SCR predictions of the vertically integrated water vapor for the Cabauw grid-box (51.89°N, 4.82°E) with values derived from radiosondes launched at De Bilt, the Netherlands (52.10°N, 5.18°E) at 6, 12, and 18 UTC (+18 to +30 h).

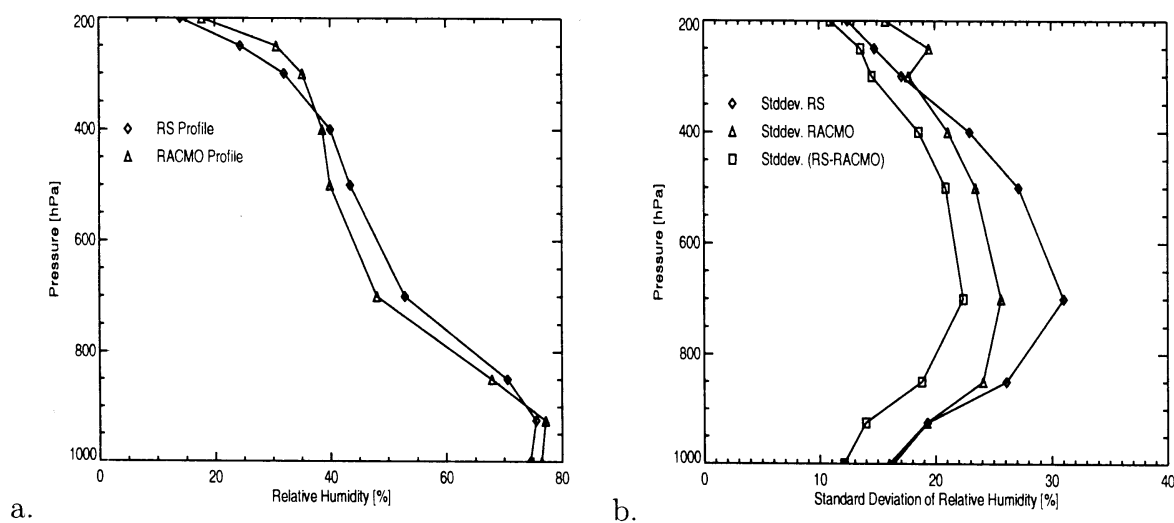


Figure 7.2: Comparison of water vapor profiles predicted by SCR for Cabauw and measured by radiosondes at De Bilt at 6,12 and 18 UTC. The mean profiles of relative humidity versus pressure for the four-year period from 1997 until 2000 are shown for radiosonde data (RS) and SCR model output (a.). The standard deviation of individual profiles from the climatological mean are shown for both data sources together with the standard deviation of radiosonde and SCR data in (b.).

the largest part of absorption of shortwave radiation in the Earth's atmosphere. In contrast to well-mixed gases, it exhibits a substantial amount of variability in time and space, which is induced by the hydrological cycle. A good model skill for predicting water vapor including its vertical distribution is required for the accurate representation of cloud processes and for the calculation of vertical profiles of heating caused by the absorption of solar radiation.

To evaluate the quality of SCR's water vapor fields, radiosonde data from De Bilt (52.10°N, 5.18°E) are used as reference. Due to the use of a single column model, the quality of the humidity fields is mainly determined by the forcings prescribed by the 3D forecasts of RACMO. Furthermore, a strong influence of the lateral boundary conditions given by the ECMWF analysis is expected. During the time period of the model runs, radiosondes of type RS80 built by Vaisala were launched every six hours as part of the operational service of KNMI. Only the launch times at 6, 12 and 18 UTC are included in the comparison, corresponding to forecast lengths of 18, 24 and 30 hours. The midnight launch has been excluded as it is not relevant for the solar radiation budget. This results in 2,936 individual profiles in combination with simultaneous model output. Deviations of the atmospheric profiles at De Bilt and Cabauw originating from the spatial distance of 22.5 km between both sites have been found to be small (van Meijgaard et al., 2001). Hence, the radiosonde data are assumed to be also representative for Cabauw, the base point of the SCR model runs.

Two quantities of model-predicted water vapor fields are studied here. The first quantity is the vertically integrated water vapor (IWV), which is a measure for the total amount of water vapor present in an atmospheric column and accounts for most of the variability in column-integrated atmospheric absorption by water vapor (Li et al., 1993). The second quantity is the vertical profile of relative humidity. The relative humidity is defined as the ratio of the current mixing ratio of water vapor to the saturation mixing ratio with respect to water at the same temperature and pressure. Thus, it is the central parameter which determines condensation and evaporation processes and thus influences the development of clouds. For the intercomparison, the saturation pressure with respect to liquid water is used for calculation of the relative humidity even for temperatures below the freezing point. This treatment is in contrast to the algorithm used to infer the saturation pressure in RACMO and is made in order to stay consistent with the measurements reported by the radiosondes.

An important point to consider is the limited accuracy of measurements of relative humidity made by radiosondes. The employed sensors are known to produce unreliable results at temperatures well below 0° C. In cloudy situations, the response of the detector is too slow to capture sharp gradients of humidity. Furthermore, moisture on the sensors can lead to significant biases. Quantified estimates of these errors are given in Miloshevich et al. (2001) and an intercomparison of the data of different types of radiosondes is presented in WMO (1993). Uncertainties relevant for the current investigation are mainly limited to the upper troposphere, which makes conclusions less reliable for that region. As most of the water vapor is generally located in the lower troposphere, no large errors in the IWV are expected to result from these shortcomings. A further aspect is probably also relevant. The radiosonde measures atmospheric parameters for a very small atmospheric volume. At this small scale, larger fluctuations

are expected than for grid-box mean quantities at typical model resolution. While this sampling should not affect the climatological means derived from a large number of profiles, a higher observed variability should occur for radiosonde data than for model forecasts.

A scatter plot of model-predicted and radiosonde-derived IWV is shown in Fig. 7.1. The climatological mean is reproduced well, having values of 18.5 kg m^{-2} and 18.7 kg m^{-2} for the radiosonde-derived IWV and the SCR output. The observed variability in IWV is characterized by a standard deviation of 7.3 kg m^{-2} , versus 7.1 kg m^{-2} for the model. Comparing modeled and measured values of IWV for individual cases, a standard deviation of 4.0 kg m^{-2} and a linear correlation coefficient of 0.85 are found. Thus, the size of these deviations is a substantial fraction of the observed variability. The explained part of the variance is given by the square of the linear correlation coefficient in case of a simple linear model (see e.g. Rice, 1988). This leads to the conclusion that about 72% of the natural variance is reproduced by the model.

A comparison of vertical profiles of relative humidity obtained by radiosondes and SCR is presented in Fig. 7.2. The climatological mean values of model-predicted and measured profiles of relative humidity show a reasonable agreement. Deviations of no more than 6% occur throughout the full range of heights considered. A slightly too moist and shallow boundary layer is followed by a too dry middle troposphere in the model. Above 400 hPa, the model atmosphere seems to be too wet again in comparison to the radiosonde profiles. However, this behavior can possibly be attributed to the underestimate of radiosonde-inferred relative humidity at low temperatures reported by Miloshevich et al. (2001).

Studying the deviations of modeled and measured profiles of the relative humidity on a case-by-case basis, a number of model shortcomings become evident. In Fig. 7.2.b, the standard deviation of both the radiosonde data and the model output from their climatological means are plotted as function of pressure to present a visualization of the natural variability. Also shown is the standard deviation of the difference of model output and measurements. An underestimate of the modeled variability of relative humidity in the middle troposphere by the measurements is clearly visible. It is not clear whether this behavior is attributable to model shortcomings or is caused by the smaller spatial scale of the radiosonde measurement mentioned above. A comparison of the magnitude of the standard deviations shows that the mean model error is a significant fraction of the observed variability. Correlation coefficients calculated for the different pressure levels range from values of 0.64 to 0.74, with a mean of about 0.7. The values of correlations below 0.7 correspond to the height interval from 700 hPa to 400 hPa. The range of correlations indicates that only about 40 – 55% of the observed variance is captured by the model predictions. Thus, the model's ability to reproduce individual profiles of relative humidity is rather low.

7.4 Cloud Cover

For a realistic representation of cloud-radiation interactions, the statistical properties of cloud coverage including its vertical distribution need to be reproduced by numerical models with reasonable accuracy (Ramanathan et al., 1989). Unfortunately, no reliable

7. Evaluation of Model Predictions.

a.

Octas	0-1.5	1.5-4.0	4.0-6.5	6.5-8	Nr. SCR
0-1.5	5.5	5.9	6.2	4.2	21.8
1.5-4.0	1.2	4.5	9.3	7.3	22.3
4.0-6.5	0.6	3.7	11.5	16.4	32.1
6.5-8	0.3	2.0	8.1	26.7	37.0
Nr. Obs.	7.6	16.1	35.0	54.5	15157

b.

Octas	0-1.5	1.5-4.0	4.0-6.5	6.5-8	Nr. SCR
0-1.5	20.4	12.5	9.3	4.5	46.6
1.5-4.0	2.5	6.1	8.6	4.4	21.6
4.0-6.5	1.6	4.0	7.9	8.2	21.8
6.5-8	0.3	0.8	2.7	6.3	10.0
Nr. Obs.	24.8	23.4	28.4	23.4	17157

c.

Octas	0-1.5	1.5-4.0	4.0-6.5	6.5-8	Nr. SCR
0-1.5	52.4	7.6	3.5	0.8	64.3
1.5-4.0	8.6	4.8	3.2	1.3	17.9
4.0-6.5	4.3	3.7	3.9	1.7	13.6
6.5-8	1.1	1.1	1.2	0.8	4.2
Nr. Obs.	66.4	17.1	11.9	4.5	4747

d.

Octas	0-1.5	1.5-4.0	4.0-6.5	6.5-8	Nr. SCR
0-1.5	35.7	11.8	6.5	1.4	55.4
1.5-4.0	4.4	5.3	5.9	1.2	16.7
4.0-6.5	2.8	5.0	6.3	3.5	17.5
6.5-8	1.2	1.8	4.1	3.2	10.3
Nr. Obs.	44.1	23.8	22.9	9.3	2908

Table 7.1: Contingency table showing the fraction of events (in percent) of (a.) total, (b.) low-level, (c.) medium level and (d.) high-level clouds separated according to four classes of cloud cover specified in octas. Column and row number correspond to the classification of synoptic report and SCR cloud cover, respectively. Also shown is the total number of cases.

7.4 Cloud Cover

and objective measurements of the vertical profiles of cloud fraction are available for the considered dataset. Hence, synoptic cloud reports are used instead in the current analysis. Due to the subjective nature of synoptic cloud reports, some conclusions are likely less reliable than for similar comparisons based on instrumental data sources such as e.g. cloud lidars or radars.

A short summary of the cloud information available from synoptic reports is given here. Clouds are grouped into three vertical atmospheric levels, which are low-level (0 – 2 km), medium-level (2 – 7 km) and high-level clouds (7 – 13 km). The height intervals apply to standard midlatitude conditions and are different for the tropics and the polar region due to differences in the tropopause height. Generally, estimates of cloud amount are given in octas. However, a minimum value of 1 octa must be reported if any cloud is present within the field of view of the observer. Similarly, 8 octas may only be reported if the sky is completely obstructed by clouds and in the presence of a stratiform cloud type. Both rules introduce a non-linear dependence of synoptic and real cloud cover. Two estimates of cloud cover are reported, which correspond to the total and to the low- and medium-level cloud amount. The value of the low- and medium-level cloud amount either refers to the lowest atmospheric level in the presence of low-level clouds or to the medium level in the absence of low-level clouds. This information can be inferred from the cloud type reports, which are available for all three levels. Not all of the information is generally available in a single report. For example, no information about clouds located above a fully cloudy level can be given due to the obstructed view of a surface observer. Due to the nature of these reports, underlying atmospheric levels must be completely cloud-free to be able to infer reliable information on the amount of mid- and high-level clouds.

For the current study, each synoptic cloud report available from all six manned meteorological stations surrounding Cabauw is included as an independent estimate of the mean cloud profile for the Cabauw grid box. The total cloud cover and the cloud cover for each individual atmospheric level at a given time are determined by averaging, if at least one report is available. Otherwise, the information is marked as missing. This procedure implies that non-integer values of the cloud cover reported in octas can occur. To separate the SCR cloud cover into equivalent vertical levels, pressure limits of 795 hPa and 410 hPa have been selected, which correspond to average geometric heights of 1993 and 7011 meters. Random-maximum cloud overlap is assumed to combine the cloud cover of multiple layers into a single level-averaged cloud cover. The height limits of atmospheric levels vary by several tens of meters for individual cases due to the natural variability of the pressure field. In practice, the impact of these variations is expected to be minor, as synoptic observers will also make errors in assigning clouds to the correct vertical level.

Contingency tables of cloud cover are shown in Tab. 7.1. For this purpose, both modeled and observed cloud amounts are classified into four different categories, corresponding to no or little clouds (0-1.5 octas), partly cloudy (1.5-4 octas), mostly cloudy (4-6.5 octas), and nearly or fully overcast conditions (6.5-8 octas). Each individual pair of forecast and observation is then assigned to one of the sixteen fields according to the classifications of both cloud covers. The column number denotes the classification of the observation and the row number of the model cloud cover. The bottom row

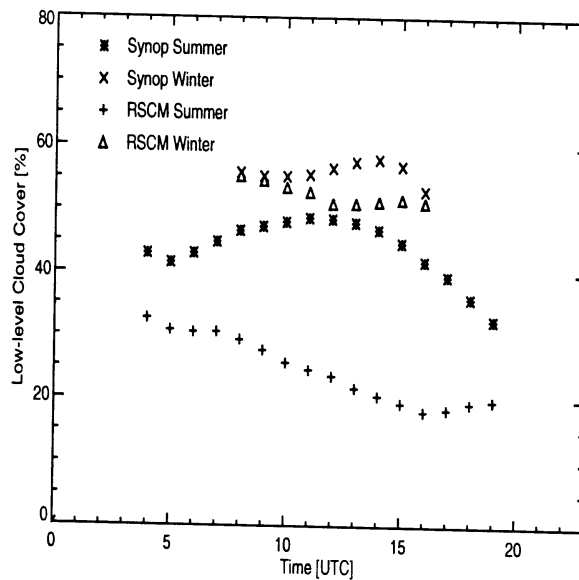


Figure 7.3: Comparison of the diurnal cycle of low-level cloud amounts from SCR output and synoptic cloud reports for winter and summer months.

and rightmost column list the frequency distribution of each class for observations and model predictions, respectively.

The contingency table for the total cloud cover is presented in Tab. 7.1.a based on 17157 individual cases. Several shortcomings are evident. The model significantly overestimates the frequency of cases with little or no cloud cover. On the other hand, the model strongly underestimates the occurrence of nearly overcast skies. A general tendency of the model to underestimate cloud cover is present, with climatological mean values of 57% and 71% for model and synoptic cloud cover. The model predictions are only correct in about 40% of the cases. This is reflected by the large number of cases contributing to the off-diagonal elements of the contingency table, in particular in the upper-right corner.

The model predictions of low-level cloud amount show a behavior rather similar to the total cloud cover, as can be seen from the contingency table in Tab. 7.1.b. Mean cloud fractions of 49.5% and 35.3% are found for observations and SCR forecasts, respectively, indicating a large negative bias of the model output for low-level cloud amount. Too few events with nearly or fully overcast sky and too many events with little or no clouds are predicted by the SCR. Fig. 7.3 presents further insights into the origin of this model behavior. Shown are the diurnal cycle of observed and modeled low-level cloud amount for summer (June to August) and winter months (December to February). Only synoptic observations during day light hours are considered, which ensures a consistent accuracy of synoptic reports and explains the fewer data point available for the winter period. In winter, the model is in rather good agreement with synoptic observations, and only a weak diurnal change in cloudiness is evident. In summer, however, a pronounced maximum in cloud fraction can be seen at about 12 UTC in the synoptic observations.

7.5 Cloud Transmissivity

This diurnal cycle is not reproduced by the SCR, but a decline in cloud fraction is found instead during the course of the day. The increase in cloud fraction is likely the result of convective activity induced by the strong insolation during noon hours in summer. Thus, the observed diurnal cycle in cloud fraction is mainly caused by increases in the amount of convective clouds, which seem to be poorly represented in the SCR. This conclusion is confirmed by a large number of erroneous clear-sky predictions by the SCR, where small-scale convective clouds are present in reality. Out of a total of 5194 cases where synoptic observers report the presence of cumulus humilis, fractus, mediocris or congestus clouds, 2428 or 47 % are forecasted as clear-sky by SCR. In winter, large-scale processes are probably more dominating for the cloud formation and the relevance of convection is greatly reduced due to the smaller amounts of incident solar energy. This could explain the better agreement of model output and observations during winter months. Nevertheless, a similar trend with much smaller amplitude is still visible in Fig. 7.3.

Tab. 7.1.c and Tab. 7.1.d show the contingency tables for the mid-level and high-level cloud amounts. In calculating these tables, an important assumption has to be made. Underlying atmospheric levels are required to be cloud-free to be able to infer unambiguous information about the cloud amount for the middle and high atmospheric levels from synoptic reports. If this condition is met for at least one out of the total number of six stations, the case is included in the tables. This procedure is only correct in a statistical sense, if such a report is an unbiased estimate of the grid-box average cloud cover. A violation of this requirement is possible if a correlation of the cloud amounts of different vertical levels is present at small spatial scales relevant for the synoptical reports. The existence of such a correlation is thus neglected in this analysis. The smaller number of cases available for the comparison results from the obstructed field of view of synoptic observers by lower cloud layers. For the mid-level, average cloud amounts agree well with values of 19.5 % and 19.7 % for synoptic and modeled coverage. High-level cloud fraction is underestimated again by the model with an average value of 27.6 % versus 34.1 % from synoptic observations. The frequency distributions of the occurrence of the different classes of cloud cover agree well for model predictions and synoptic observations of mid-level clouds. The agreement is slightly worse for high-level clouds.

The contingency tables for all three atmospheric levels clearly show that the model's skill for predicting a correct cloud cover on a case-by-case basis leaves room for improvements. This is also reflected by the linear correlation coefficient of modeled and observed cloud cover, which is in the order of 0.5 for all atmospheric levels.

7.5 Cloud Transmissivity

A correct representation of the interaction of shortwave radiation and clouds is essential for GCMs if they are to be used as reliable predictors for climate sensitivity. The effects of clouds on the radiation balance depend on a variety of factors such as cloud fraction, vertical location, the amount of cloud water and the size and thermodynamic phase of cloud particles (Ramanathan et al., 1989; Slingo, 1990).

The amount of solar irradiance downwelling at the surface is used as one important

7. Evaluation of Model Predictions.

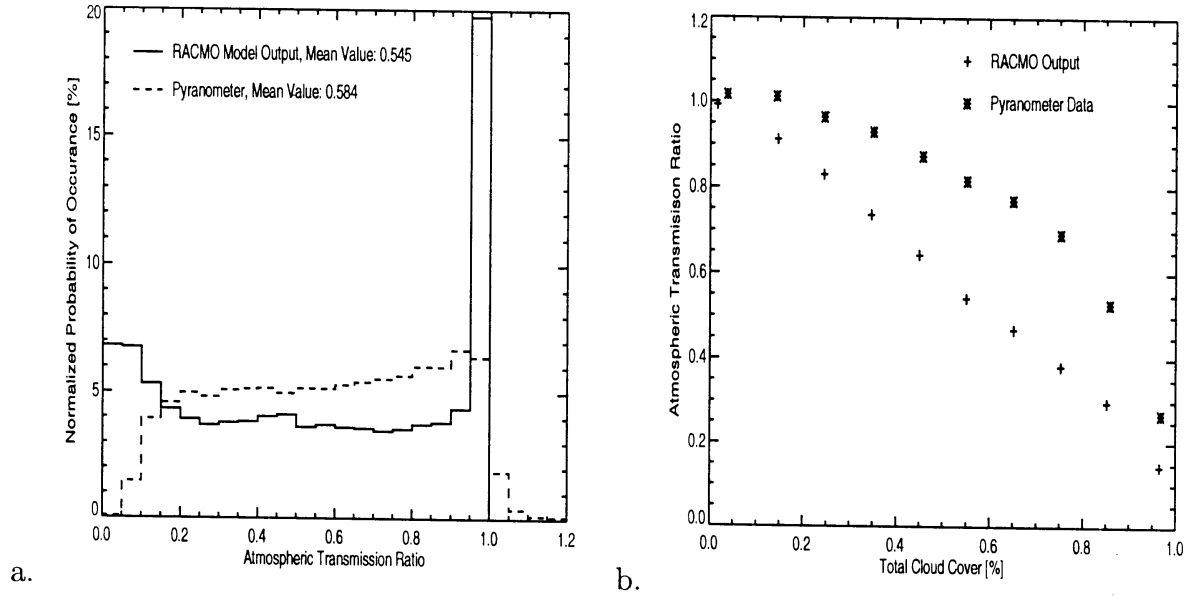


Figure 7.4: (a.) Normalized frequency distribution of the occurrence of atmospheric transmission ratios (ATRs) obtained from pyranometer measurements and from model output of SCR. (b.) Mean atmospheric transmission ratio as function of total cloud cover for observations and SCR output.

quantity to evaluate the agreement of the modeled and true shortwave radiation balance. As shown in Fig. 5.2, the fraction of solar radiation transmitted by the atmosphere is reduced strongly in the presence of clouds, mainly caused by an increase of the reflection of solar radiation back into space. This mechanism is generally referred to as the albedo effect. To quantify this reduction, the atmospheric transmission ratio (ATR) has been defined in Ch. 6 to be

$$\text{ATR} \equiv \frac{F_{SFC}^-}{F_{SFC,CS}^-}, \quad (6.1)$$

where F_{SFC}^- is the actual value of downwelling solar irradiance at the surface and $F_{SFC,CS}^-$ is the value expected during otherwise identical clear-sky conditions. The clear-sky irradiance at the surface calculated by the radiation code of RACMO is used for the calculation of both model predicted and measured values of the ATR throughout this investigation. Because errors in the RACMO-predicted amount of clear-sky solar irradiance will affect both observations and model output, at least a part of the resulting errors in ATR are expected to cancel. For low sun, large errors in the calculated ATR are possible, because the atmospheric transmissivity is small and the relative accuracy of pyranometers decreases for small values of the irradiance. The relevance of these cases for the shortwave radiation balance is low due to the small amount of solar energy incident at the top of the atmosphere. Thus, only cases with a cosine of the solar zenith angle exceeding 0.2 are considered in the following analysis.

Based on pyranometer data from the eight meteorological stations closest to Cabauw, an average ATR has been calculated for 30-minute intervals, which is also the tempo-

7.5 Cloud Transmissivity

ral resolution of the SCR output. The number of stations is large enough to provide a sufficient spatial sampling of the downwelling irradiance to ensure a good representativeness of pyranometer data for the grid-box averaged irradiance. The normalized frequency distributions of ATR for both observations and SCR output are shown in Fig. 7.4.a. Several differences are identified. Overall, the mean ATR predicted by the model is 54.5% and thus 4% lower than the average value inferred from the pyranometers, which has a magnitude of 58.4%. Re-expressed in terms of mean solar irradiance, pyranometer and SCR values of 282 W m^{-2} and 291 W m^{-2} are obtained. The strong peak of the model ATR close to a value of unity is attributable to model predictions of clear-sky conditions. Due to the natural variability of the clear-sky irradiance (see Ch. 4) and the sampling issues arising from broken cloud fields with low cloud cover (see Ch. 6), no such sharp peak is visible nor expected for the pyranometer data. However, if the number of cases having an ATR exceeding 0.9 is considered, the model's tendency to overestimate the occurrence of clear-sky situations can again be identified. 24.1% of the predictions exceed this value, in contrast to only 15.7% of the pyranometer records. On the other hand, the occurrence of very small values of the ATR is also overestimated by the model, with 13.7% of the model predictions and only 1.4% of the measurements falling below a value of 0.1. A general tendency of the model to overestimate extreme values of ATR and to underestimate the occurrence of intermediate values is evident. A correlation of 0.52 is found for the modeled and observed values of the ATR. As the ATR is a measure for the modulation of the atmospheric transmissivity by clouds, the square of the correlation indicates that only about 27% of the natural variability in atmospheric transmissivity induced by clouds is reproduced by the SCR. This value is of similar magnitude as the explained variance of the cloud amount, but significantly lower than for the relative humidity. The finding supports that the processes determining cloud parameters and cloud-radiation interactions are not adequately represented in this model for the studied region, a conclusion which is typical for current GCMs even on a global scale (IPCC, 2001).

The model underestimate of the mean atmospheric transmissivity seem to contradict the results of Sec. 7.4, where a too-low average of the cloud cover predicted by the model is found. To explain this behavior, the model-predicted transmissivities of clouds need to be significantly lower than real values for similar amounts of cloud cover. As a confirmation of this hypothesis, the mean ATR is calculated for 10 equally sized bins of the total cloud cover and is plotted as function of bin-averaged cloud cover for both model forecasts and observations in Fig. 7.4.b. The model curve decreases as a nearly linear function of total cloud cover. The corresponding decrease of measured values of the ATR is a strongly convex curve, with a much smaller decrease of the ATR at low values of the cloud cover than found for the SCR results. Throughout the full range of cloud amounts, the model predictions of ATR are 10 – 30% too low once the cloud cover exceeds 10%. The highly non-linear functional dependence of ATR on the total amount of cloud cover is not reproduced by the SCR. Intercomparing different models, van Meijgaard et al. (2001) find a similar underestimate of atmospheric transmissivity calculated by RACMO for a 10-day period. Based on the predictions of the other models, they propose an overestimate of atmospheric absorption as explanation for this behavior.

7.6 Summary and Discussion

In this chapter, output from a single-column version of RACMO is compared to radiosonde data and observations from six synoptic and two automated meteorological stations covering a region of about $60 \times 60 \text{ km}^2$ in the Netherlands in order to evaluate the representation of clouds and their interaction with solar radiation in SCR.

Water vapor is a central parameter responsible for the formation and development of clouds. Model predictions of the amount of vertically integrated water vapor match the observations closely both in terms of the climatological mean and the observed variability. Furthermore, about 70 % of the observed variability is captured by the model in a case-by-case comparison. For the vertical profiles of relative humidity, however, the SCR output shows less variability and underestimates the climatological mean by several percent in the middle troposphere. Only about 40-55 % of the observed variability is predicted by the model. It has to be noted, however, that the external forcings of the single column model are mainly responsible for the quality of humidity fields of SCR. Hence, these shortcomings have to be attributed either to the 3D forecasts of RACMO or to the ECMWF analysis used as lateral boundary conditions. A further source of uncertainty in the comparison is introduced by the limited representativeness of the radiosonde data for grid-box mean values, which might affect the observed variability. Model errors in relative humidity are expected to propagate to cloud properties such as the fraction of cloud water and the amount of clouds, unless the cloud parameterizations are tuned to accommodate for model shortcomings. As cloud fraction is directly diagnosed from relative humidity in RACMO and SCR, it is an excellent example of a quantity which is directly affected by the large case-by-case errors, biases and the underprediction of variability in the middle troposphere.

SCR forecasts of the vertical profiles of cloud fraction show significant deviations from synoptic observations. The total cloud cover is underestimated by 14 % as a result of too-low amounts of low-level and high-level clouds. In contrast, forecasts of the medium-level cloud amount seem to agree fairly well with observations. However, these conclusions need to be treated with some caution due to the subjective nature of synoptic cloud reports. A possible candidate causing the shortcomings of low-level clouds seems to be a poor representation of small-scale convection in the SCR. For individual cases, the correlation of synoptic cloud cover and model output is about 0.5 for all three atmospheric levels, which indicates that the reliability of predicted cloud amounts is rather low.

Despite the underestimate of cloud cover, the mean solar irradiance is 9 W m^{-2} lower in SCR than the pyranometer-inferred mean value. This behavior is caused by a substantial underestimation of mean cloud transmissivity in the presence of clouds for a given value of total cloud cover. If pyranometer measurements indeed underestimate the solar irradiance as is discussed in Ch. 3 and reported by Philipona (2002), the true magnitude of the bias is expected to be even larger. On the other hand, if the model overestimate of clear-sky irradiances found in Ch. 4 results from shortcomings in the radiative transfer scheme, the model biases during clear-sky and cloudy conditions have opposite signs and will partly cancel. Then, the exact magnitude of the difference will depend on the fraction of clear-sky and cloudy situations.

7.6 Summary and Discussion

Several factors can be responsible for the too-strong reduction of atmospheric transmissivity by the model clouds. Horizontal cloud inhomogeneity within a model grid box is not considered in the SCR radiation scheme, but can cause significant biases for the modeled radiation budget (Rossow et al., 2002). This shortcoming is addressed to some extent in recent versions of the ECMWF model. A reduction factor of 0.7 for the cloud optical depth is introduced to obtain an effective value representative for the calculation of radiative fluxes, following the approach proposed by Cahalan et al. (1994). This leads to a better agreement of modeled shortwave radiative fluxes in comparison to ERBE measurements (Barkstrom, 1984), as shown by (Tiedtke, 1996). An underestimate of the mean droplet size or an overestimate of cloud water will also lead to optically too-thick clouds. Crewell et al. (2002) find an indication of a high bias of cloud liquid water in RACMO output based on a comparison with microwave radiometer measurements. However, the length of the time period of two months is possibly not sufficient for reliable conclusions about long-term model climatologies. A rough estimate of the mean effective radius of droplets for water clouds used in the model and calculated with Eq. 5.1 yields a value of $5.8 \mu\text{m}$. This value is significantly lower than the value of $10 \pm 5 \mu\text{m}$ reported by Han et al. (1994) for mid-latitude conditions based on satellite data collected by the ISCCP project (Rossow and Schiffer, 1991). It has to be noted, however, that the satellite retrieval is mainly sensitive to the upper part of clouds, where the largest droplet sizes are expected, and is also not very accurate. Further possible explanations include the overestimate of atmospheric absorption in the presence of clouds reported by Wild et al. (1998) for the shortwave radiative transfer scheme used in the SCR. The unrealistic functional dependence of the atmospheric transmission ratio on cloud cover can also be an indication of an erroneous treatment of the overlap of independent cloud layers. Further information on cloud properties and atmospheric absorption are required to allow more definite conclusions about the underlying mechanisms.

The shortcomings of the model in correctly reproducing the influence of clouds on the shortwave radiation balance will have an effect on a variety of important physical processes, such as the hydrological cycle and in particular evaporation. This in turn will introduce errors in the prediction of humidity and cloudiness. The missing amount of radiation reaching the surface is either absorbed and causes an unrealistic heating of the atmosphere, or is reflected back into space and therefore lost in the calculation of the Earth's energy budget. Hence, a number of important climate feedbacks are affected by the model shortcomings, which may lead to an unrealistic model behavior.

In the introductory section of the chapter, the statement has been made that the considered period of four years is sufficient for reliable conclusions about the climatological performance of the model for the considered region of the Netherlands. To ensure that results are indeed representative for longer time periods, all comparisons reported in this study have also been carried out for individual years in a first effort to study long-term variations in model performance. Significant interannual variability in cloud cover, humidity fields and the mean atmospheric transmissivity for solar radiation are observed. Nonetheless, the reported deviations of model output and observations have been verified to be similar at least in a qualitative sense. The only exception is the mean difference of modeled and measured solar irradiance downwelling at the surface.

7. Evaluation of Model Predictions.

It is very sensitive to pyranometer accuracy and the ratio of clear-sky to cloudy situations due to the cancellation of biases described above. A quantitative estimate of the difference therefore requires a reliable estimate of the mean cloud cover. As the cloud cover exhibits a strong interannual variability of up to 10 % in both model output and synoptic reports, the time period of four years is insufficient for an accurate estimate.

The present investigation clearly shows that substantial improvements are still required to achieve a reliable representation of clouds and the resulting influence on the solar radiation budget in numerical models used for climate studies. Serious shortcomings have been identified in the predictions of humidity fields, cloud cover and the transmissivity of clouds to solar radiation. Each of these shortcomings is expected to affect the quality of predictions of other quantities and processes relevant to the climate system.

Chapter 8

Conclusions and Outlook

Within this thesis, several different aspects related to our current understanding of the solar radiation budget and the impact of clouds on solar radiative fluxes at the surface are analysed. For this goal, an extensive set of surface and satellite observations of the Netherlands has been used to evaluate their consistency with the output of a current radiative transfer model and a single-column version of a climate model developed for forecasts on a regional scale.

The high bias of model-predicted downwelling solar irradiances at the surface in comparison to measurements is an issue central not only to this thesis, but also to climate research and remote sensing in general. This bias is present in both clear-sky and cloudy situations, as is shown in Ch. 4 and Ch. 6. Similar deviations have been reported by numerous studies (e.g. Cess et al., 1995; Ramanathan et al., 1995; Kato et al., 1997; Wild et al., 1998).

Initially, an insufficient amount of atmospheric absorption in radiative transfer models has been proposed as an explanation (e.g. Arking, 1996; Halthore et al., 1998). As a result of reinvestigations, some deficiencies in the absorption properties of relevant atmospheric gases have been identified (e.g. Giver et al., 2000). Radiative transfer schemes in use have been updated to include more recent spectroscopic information on the absorption properties of atmospheric gases. However, no shortcomings have been found so far which are sufficient to explain the full magnitude of the bias.

A number of studies have provided further insight into the origin of the bias. During clear-sky situations, the direct solar irradiance is reproduced within the limits of instrumental accuracy (Halthore et al., 1997). A comparison of line-by-line radiative transfer calculations and spectrally resolved measurements of diffuse and direct radiation obtained with a rotating shadowband radiometer also showed good agreement (Mlawer et al., 1998). On the other hand, Cess et al. (2000) have found that the diffuse-field irradiances reported by pyranometers are sometimes even smaller than a lower limit set by the theory of Rayleigh scattering. Furthermore, Bush et al. (2000) show that the well-known thermal offset of pyranometers (see e.g. Wardle et al., 1996) can reach much larger values than reported in previous estimates. The theoretical analysis presented in Ch. 3 indicates that the thermal offset can also affect the accuracy of pyranometer calibration, because it is not accounted for in the calibration procedure. Based on measurements obtained with improved, temperature-stabilized and ventilated instruments,

Conclusions and Outlook

Philipona (2002) reports an underestimate of solar irradiances in the range from 3 – 5.5 percent for traditional pyranometer setups during a nine-day intercomparison and attributes it to the thermal offset and calibration errors. A two-year time series obtained from similar instruments under less controlled conditions reveals an even larger bias of 8 percent.

From the current perspective, it seems likely that at least a large part of the difference of modeled and measured solar irradiances can be attributed to shortcomings in the presently available pyranometer data. The questionable accuracy of pyranometers can thus be seen as a prime candidate for an explanation of the bias described above and also as a major obstacle for the evaluation of current radiative transfer models.

An investigation and solution of the issues affecting the accuracy of pyranometer measurements is expected within a short time frame. As part of the CESAR project (Russchenberg et al., 2001), KNMI is currently setting up improved measurements of solar surface radiative fluxes at the Cabauw site in accordance with the standards defined by the Baseline Surface Radiation Network (Ohmura et al., 1998). With state-of-the-art instruments and an optimal operating environment, a reference for the evaluation of the quality of standard KNMI pyranometer measurements will become available soon.

The investigation of Ch. 4 shows that the accuracy of model estimates of the clear-sky solar radiation budget is currently limited by insufficient knowledge of aerosol optical properties and their large temporal and spatial variations. The interaction of aerosols and radiation is also found to be relevant for cloudy conditions in Ch. 5. A better characterization of aerosols is thus an essential step for advancing our understanding of the forcing of the solar radiation budget by aerosols. This issue is currently being addressed by several major projects. The AERONET network of currently more than 70 globally distributed ground stations (Holben et al., 1998) retrieve a large number of aerosol properties from multi-angular and multi-spectral radiometer measurements in the visible and near-infrared spectral region. One of these stations has recently started operation at Den Haag, the Netherlands and will be moved to Cabauw as a contribution to the CESAR project. The aim of the Global Aerosol Climatology Project (Mishchenko et al., 2002) is the development of reliable aerosol retrievals from satellites and their validation with ground measurements. This will allow the derivation of an aerosol climatology with high spatial and temporal resolution having a global coverage, even if the uncertainties of the satellite retrievals will be substantially larger than for surface measurements. Nevertheless, a much better representation of aerosols in climate models will be possible as a consequence.

The investigations of Ch. 5 and Ch. 6 present promising results for determining the influence of clouds on the solar radiation budget from satellite measurements. Nevertheless, several limitations of current retrievals of cloud properties from meteorological satellites are encountered. The determination of thermodynamic phase and particle size in combination with cloud optical depth is required not only for a more realistic description of cloud-radiation interactions within the retrieval, but also for a comparison of retrieved cloud properties with those modeled by GCMs and NWP. The additional spectral channels available on newer NOAA satellites and Meteosat Second Generation allow these issues to be addressed (Jolivet and Feijt, 2002). However, a much more fundamental shortcoming is also encountered in these investigations. In

the current generation of retrievals, plain-parallel horizontally homogeneous clouds are assumed. In reality, cloud properties vary strongly on a wide range of spatial and temporal scales. As a consequence, two important aspects are not properly accounted for in retrievals. Firstly, it is well known that significant biases and uncertainties can result for radiative quantities due to the effects of 3D radiative transfer as a consequence of this variability (Cahalan et al., 1994). The magnitude of these effects and the uncertainties resulting from unresolved variability are still the subject of ongoing research. Aided by the development of 3D radiative transfer codes, substantial progress is made towards resolving these issues (e.g. Várnai and Marshak, 2001; Cairns et al., 2000) and estimating the resulting impact for model estimates of the radiation budget (Rossow et al., 2002). Secondly, the comparability of ground measurements and satellite images is affected by their differing spatial scales. Surface radiation measurements are point measurements with limited representativeness for larger spatial regions, while meteorological satellites have typical pixel sizes in the order of $1 \times 1 \text{ km}^2$. A common approach to overcome this problem is the selection of appropriate averaging scales for the surface-inferred time series and the satellite images, as has been done in Ch. 5 and Ch. 6. The theoretical study of Barker and Li (1997) and the measurement results presented in Ch. 6 show that deviations are expected as a result of this approach even for a hypothetical perfect retrieval. The underlying mechanism responsible for these deviations is the horizontal transport of photons and therefore closely related to the effects of 3D radiative transfer mentioned above. A quantification of these deviations is required to assess the quality of a retrieval.

In the final study of this thesis, the skill of a single-column model for representing clouds and their interaction with radiation is evaluated for a four-year time period for a small region located in the Netherlands. Based on synoptic reports and pyranometer measurements, it is found that neither the amount of clouds nor the transmission of solar radiation by clouds are correctly reproduced by the model. Deficiencies are also identified in the modeled fields of relative humidity, which is a central parameter determining the formation and development of clouds. These results show that one of the central goals of climate research, the development of numerical models which reliably reproduce the physical quantities and interactions relevant to the Earth's climate, is still far ahead and will require a significant amount of further research effort. Progress is mainly hampered by a lack of detailed and accurate long-term statistics of microphysical cloud properties, radiative fluxes and other quantities and processes of relevance for clouds, such as evaporation, precipitation and the concentration of cloud condensation nuclei. This information is required to evaluate and improve the formulations used in current general circulation models. A large number of projects focus on particular aspects of GCMs. Two typical examples are the Cloud Liquid Water Network (CLIWA-NET, 2002) and the EUROpean Cloud Systems (EUROCS, 2002) projects. CLIWA-NET uses a network of microwave radiometers distributed throughout Europe to provide reliable reference data on the liquid water content of clouds and to improve its representation in models. EUROCS aims for the improvement of the description of convection and the parameterization of convective clouds in climate models. The development of new and improved measurement techniques from ground and space, such as radars, lidars, microwave radiometers and multispectral radiometers aids these in-

vestigations, increases our knowledge about clouds and provides more detailed datasets for model evaluation.

Appendix A

Pyranometer Stations

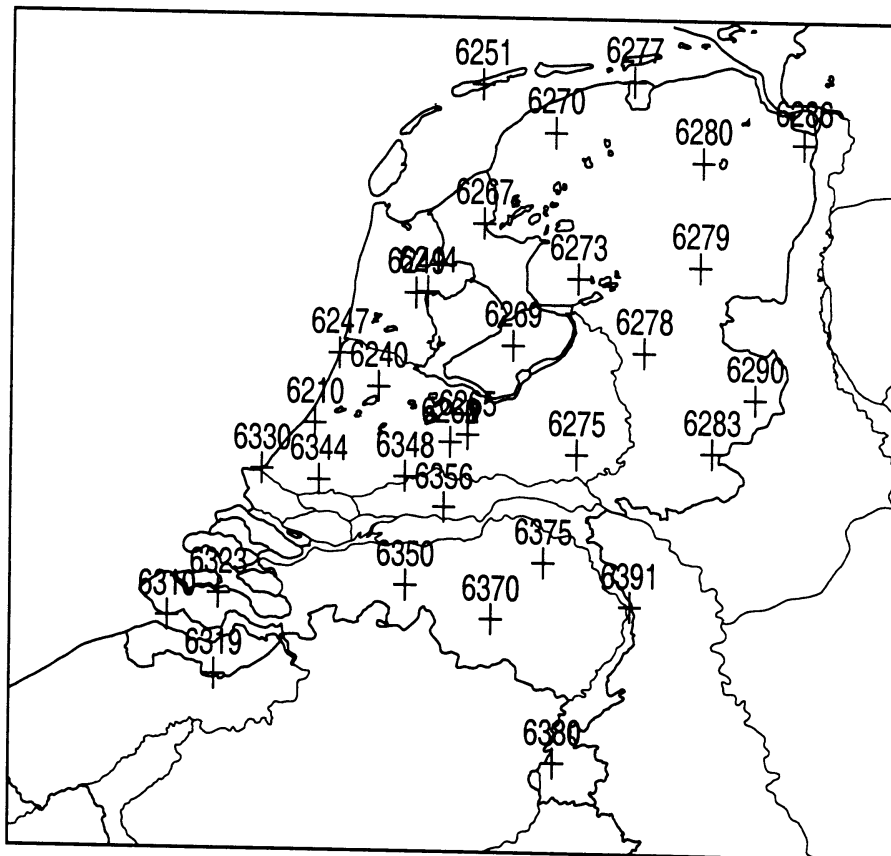


Figure A.1: Map showing the geographic location (+) of KNMI's meteorological measurement sites equipped with a pyranometer.

Number	Name	Latitude	Longitude	Synop	NWP Comp.
6210	Valkenburg	52.1650	4.4192	yes	yes
6240	Schiphol	52.3014	4.7742	yes	yes
6244	Hoorn AWS (NH)	52.6496	5.0444	no	no
6247	Bloemendaal	52.4216	4.5555	no	no
6249	Berkhout	52.6440	4.9791	no	no
6251	Hoorn AWS (Terschelling)	53.3928	5.3455	no	no
6260	De Bilt	52.1009	5.1774	yes	yes
6265	Soesterberg	52.1298	5.2744	yes	yes
6267	Stavoren AWS	52.8979	5.3557	no	no
6269	Lelystad AWS	52.4576	5.5260	no	no
6270	Leeuwarden	53.2251	5.7545	yes	no
6273	Marknesse	52.7032	5.8885	no	no
6275	Deelen	52.0609	5.8878	yes	no
6277	Lauwersoog	53.4092	6.1959	no	no
6278	Heino	52.4372	6.2635	no	no
6279	Hoogeveen	52.7502	6.5745	yes	no
6280	Eelde	53.1254	6.5858	yes	no
6283	Hupsel	52.0730	6.6495	no	no
6286	Nieuw Beerta	53.1962	7.1501	no	no
6290	Twenthe	52.2725	6.8896	yes	no
6310	Vlissingen	51.4424	3.5961	yes	no
6319	Westdorpe	51.2256	3.8616	no	no
6323	Wilhelminadorp AWS	51.5271	3.8840	no	no
6330	Hoek van Holland	51.9925	4.1238	yes	no
6344	Rotterdam	51.9546	4.4437	yes	yes
6348	Cabauw	51.9717	4.9270	no	yes
6350	Gilze-Rijen	51.5677	4.9332	yes	yes
6356	Herwijnen	51.8584	5.1452	no	yes
6370	Eindhoven	51.4455	5.4135	yes	no
6375	Volkel	51.6568	5.7056	yes	no
6380	Maastricht Airport	50.9104	5.7680	yes	no
6391	Arcen	51.4985	6.1957	no	no

Table A.1: WMO Number, station name and geographic coordinates of KNMI's measurement stations equipped with a pyranometer. Also indicated are the availability of synoptic cloud reports and the use for the SCR evaluation of Ch. 7.

Appendix B

Calibration Coefficients of the NOAA-14 AVHRR

Source	n	$\kappa'_{1,n}$	$\kappa'_{2,n}$
Rao and Chen (1996)	0	1.09E-1	1.29E-1
	1	2.32E-5	3.73E-5
Rao and Chen (1999)	0	1.11E-1	1.34E-1
	1	1.35E-5	1.33E-5
Tahnk and Coakley (2001a)	0	1.146E-1	1.432E-1
	1	1.195E-5	5.135E-5
Tahnk and Coakley (2001b)	0	1.141E-1	—
	1	1.705E-5	—
	2	-5.358E-9	—
Vermote and El Saleous (1999)	0	1.111E-1	1.375E-1
	1	8.548E-5	1.486E-4
	2	-2.586E-7	-4.25E-7
	3	3.958E-10	5.926E-10
	4	-2.723E-13	-3.877E-13
	5	6.843E-17	9.496E-17
Vermote and El Saleous (1999) (linear fit during years 1996-98)	0	1.196E-1	—
	1	9.414E-6	—
Nguyen et al. (2001)	0	1.204E-1	—
	1	1.847E-5	—
	2	-6.224E-9	—
Calibration used in this thesis	0	1.173E-1	—
	1	1.776E-5	—
	2	-5.791E-9	—

Table B.1: Calibration constants for channel 1 and 2 of the NOAA-14 AVHRR, in (% Count⁻¹ day⁻ⁿ) from different calibration studies as described in Ch. 3.

Appendix C

Aerosol Optical Properties

λ [μm]	τ_{AER}	ω	g	n_r	n_i
0.256	0.3767	0.964	0.704	1.5	0.005
0.278	0.3643	0.966	0.702	1.5	0.005
0.295	0.3537	0.967	0.701	1.5	0.005
0.317	0.3391	0.968	0.698	1.5	0.005
0.345	0.3199	0.969	0.695	1.5	0.005
0.385	0.2922	0.970	0.689	1.5	0.005
0.430	0.2622	0.971	0.681	1.5	0.005
0.485	0.2285	0.971	0.671	1.5	0.005
0.529	0.2043	0.971	0.662	1.5	0.005
0.545	0.1961	0.971	0.658	1.5	0.005
0.558	0.1897	0.971	0.655	1.5	0.005
0.586	0.1767	0.971	0.649	1.5	0.005
0.615	0.1643	0.965	0.644	1.5	0.006
0.646	0.1519	0.965	0.637	1.5	0.006
0.675	0.1413	0.964	0.630	1.5	0.006
0.694	0.1350	0.958	0.626	1.5	0.007
0.724	0.1256	0.951	0.620	1.5	0.008
0.767	0.1137	0.938	0.610	1.5	0.010
0.818	0.1008	0.936	0.598	1.5	0.010
0.867	0.0900	0.934	0.587	1.5	0.010
0.932	0.0777	0.931	0.572	1.5	0.010
1.010	0.0655	0.927	0.555	1.5	0.010
1.120	0.0520	0.920	0.530	1.5	0.010
1.355	0.0331	0.904	0.482	1.5	0.010
1.565	0.0229	0.887	0.442	1.5	0.010
1.789	0.0161	0.866	0.404	1.5	0.010
2.059	0.0109	0.837	0.363	1.5	0.010
2.214	0.0089	0.819	0.342	1.5	0.010
2.639	0.0055	0.764	0.291	1.5	0.010
3.319	0.0029	0.664	0.228	1.5	0.010
3.813	0.0020	0.587	0.194	1.5	0.010
4.298	0.0015	0.514	0.167	1.5	0.010

Table C.1: Aerosol optical properties used in this thesis, which are calculated by Mie theory and are given by the total aerosol optical depth, single scattering albedo ω and the asymmetry parameter g for a log-normal aerosol size distribution with an effective radius of 70 nm , an effective variance of 1.8, and scaled to a total aerosol optical depth of 0.1925 at $0.55\ \mu m$.

Appendix D

Notation

D.1 List of Symbols

Symbol	Meaning	Units
θ	zenith angle	[rad]
ϕ	azimuth angle	[rad]
μ	cosine of zenith angle	[1]
ω	(single scattering) albedo	[1]
λ	wavelength	[m]
ρ	mass density	[kg m ⁻³]
η	particle number density	[m ⁻³]
τ	optical depth	[1]
r	radius of particle	[m]
F	irradiance	[W m ⁻²]
F_{\odot}	solar constant	[W m ⁻²]
I	radiance	[W m ⁻² sr ⁻¹]
\mathcal{T}	transmissivity	[1]
\mathcal{R}	reflectivity	[1]
\mathcal{A}	absorptivity	[1]
z	height above surface	[m]
\mathcal{P}	phase function	[1]
κ	instrumental sensitivity	depends on instrument
ψ	spectral response function	[1]
Δ	width of spectral response function	[1]
ϱ	angular distribution model	[1]
T	temperature	[K] or [C]
p	pressure	[hPa]
P	probability distribution	[1]
δ	sun–Earth distance	[AU]

D.2 List of Subscripts

Symbol	Meaning	Units
C	detector counts	[1]
R	reflectance factor	[1]
r	reflectance	[1]
U	instrumental output voltage	[V]
n	refractive index	[1]
IWV	vertically integrated water vapor	[kg m ⁻²]
LWP	vertically integrated liquid water	[kg m ⁻²]
ATR	atmospheric transmission ratio	[1]
χ	size parameter	[1]
k	cross-section	[m ⁻²]

D.2 List of Subscripts

Subscript	Meaning
TOA	Top of Atmosphere top of atmosphere
SFC	at the surface
ATM	for the complete atmosphere
0	for the solar spectrum or the sun
SAT	for the satellite
λ	at a specific wavelength λ
r	at a specific particle radius r
SH	shaded pyranometer
US	unshaded pyranometer
ACR	active cavity radiometer
AER	atmospheric aerosol
DIF	diffuse component
DIR	direct component
$GLOB$	global component ($DIF + DIR$)
RAY	Rayleigh scattering

D.3 List of Acronyms

ACR	Active Cavity Radiometer
ADM	Angular Distribution Model
AER	Aerosol
ATR	Atmospheric Transmission Ratio
AVHRR	Advanced Very High Resolution Radiometer
BAT	Broadband Atmospheric Transmissivity
BRDF	Bidirectional Reflectance Distribution Function
CSGI	Clear-sky Solar Global Irradiance
CM11	Pyranometer built by Kipp en Zonen
CSM	Component Summation Method
DIF	Diffuse-field radiation
DIR	Direct-beam radiation
DISORT	Discrete Ordinates Method
DSSI	Downwelling solar surface irradiance
DU	Dobson Units, measure for the ozone column amount
ECHAM	European Center Hamburg Climate Modell
ECMWF	European Center for Medium-Range Weather Forecasts
ERBE	Earth Radiation Budget Experiment
GCM	General Circulation Model
GLOB	Global radiation
GPS	Global Positioning System
GPS	Global Positioning System
HIRLAM	High Resolution Limited Area Modell
HITRAN	High Resolution Transmission Molecular Absorption Database
IPCC	Intergovernmental Panel on Climate Change
ISCCP	International Satellite Cloud Cimatology Project
ISO	International Standards Organisation, Geneva, Switzerland
IWV	Vertically Integrated Water Vapor
KLAROS	KNMI'S Local Imple of APOLL
KNMI	Koninklijk Nederlands Meteorologisch Instituut, The Netherlands
LWP	Liquid Water Content
MODTRAN	Moderate Resolution Radiative Transfer Model
MSG	Meteosat Second Generation
NASA	National Space Agency (USA)
NOAA	National Oceanic and Atmospheric Administration (USA)
NWP	Numerical Weather Prediction Model
POLDER	Polarization and Directionality of the Earth's Reflectance
PSP	Precision Spectral Pyranometer, built by Eppley Inc.
RACMO	Regional Climate Model
RMSE	Root Mean Square Error
RTE	Radiative Transfer Equation
RTM	Radiative Tranfer Model
SCR	Single-Column version of RACMO

List of Acronyms (continued)

TOA	Top-of-Atmosphere
UTC	Universal Time Coordinated
WCRP	World Climate Research Programme
WMO	World Meteorological Organisation
WRC	World Radiation Center, Davos, Switzerland

List of Figures

2.1	Geometrical Setup of the Measurements.	6
3.1	Setup for the component summation method for pyranometer calibration.	21
3.2	Response resulting from the CSM calibration due to the neglect of the thermal offset of pyranometers	23
3.3	Spectral response function of the visible channels of the NOAA-14 AVHRR instrument.	26
3.4	Comparison of different calibrations for the NOAA-14 AVHRR instrument.	28
4.1	Fraction of solar radiation absorbed by atmospheric gases	38
4.2	Distribution Density of the difference of modeled and measured clear-sky shortwave atmospheric transmissivity.	43
4.3	Bias of modeled and measured transmissivity in comparison to the systematic uncertainties.	43
5.1	Dependence and sensitivity of broad-band atmospheric transmissivity and planetary albedo on cloud optical depth	50
5.2	Comparison of retrieved cloud optical depths for ice and water clouds .	55
5.3	Comparison of retrieval results for plane-parallel homogeneous clouds .	55
5.4	Bias of retrieved cloud optical depths resulting from systematic instrumental errors	59
6.1	Comparison of satellite-retrieved downwelling solar surface irradiance .	66
6.2	Comparison of satellite retrieved and measured atmospheric transmission ratio	66
6.3	Comparison of averages of satellite retrieval and pyranometer measurements averaged for individual satellite overpasses.	69
6.4	Comparison of monthly averages of the satellite retrieval and the measurements	69
6.5	Dependence of retrieval performance on solar zenith angle and satellite zenith angle.	70
6.6	Difference in downwelling solar irradiance and atmospheric transmission ratio measured at De Bilt and Soesterberg	73
7.1	Comparison of SCR predictions of the vertically integrated water vapor with radiosonde-derived values.	82

LIST OF FIGURES

7.2	Comparison of water vapor profiles predicted by SCR and measured by radiosondes.	82
7.3	Comparison of the diurnal cycle of low-level cloud amounts from SCR output and synoptic cloud reports for winter and summer months. . . .	87
7.4	Difference in the distribution of atmospheric transmission ratios of SCR predictions and pyranometer measurements.	89
A.1	Map of KNMI's radiation measurement sites in the Netherlands.	99

List of Tables

3.1	Overview of pyranometer uncertainties.	25
4.1	Modeled mean clear-sky atmospheric transmissivity and its sensitivity for the Netherlands.	32
4.2	Differences in radiation components due to the assumption of a spectrally invariant surface albedo.	35
4.3	Clear-sky radiation components of the reference atmosphere calculated by different radiative transfer models.	39
7.1	Contingency table of observed and modeled cloud amount.	85
A.1	List of KNMI's radiation measurement sites in the Netherlands.	100
B.1	Calibration coefficients for the NOAA-14 AVHRR.	101
C.1	Aerosol optical properties used in this thesis	103

References

- Anderson, G., S. Clough, F. Kneizys, and J. Chetwynd. AFGL atmospheric constituent profiles (0-120km). GL - TR -86 - 0110, Air Force Geophys. Lab., Hascom AFB, Mass., USA (1986).
- Ångström, A. Diffuse radiation in the galaxy. *Annale Geografiska*, 11:164–172 (1929).
- Arking, A. Absorption of solar energy in the atmosphere: Discrepancy between model and observations. *Science*, 273:779–781 (1996).
- Barker, H., T. Curtis, E. Leontieva, and K. Stamnes. Optical depth of overcast cloud across Canada: Estimates based on surface pyranometer and satellite measurements. *Journal of Climate*, 11:2980–2994 (1998).
- Barker, H. and Z. Li. Interpreting shortwave albedo-transmittance plots: true or apparent anomalous absorption? *Geophysical Research Letters*, 24:2023–2027 (1997).
- Barker, H., B. Wielicki, and L. Parker. A parameterization for computing grid-averaged solar fluxes for inhomogeneous marine boundary layer clouds. part II: Validation using satellite data. *Journal of the Atmospheric Sciences*, 53:2304–2316 (1996).
- Barkstrom, B. The Earth radiation budget experiment (ERBE). *Bulletin of the American Meteorological Society*, 65:1170–1185 (1984).
- Bennartz, R. and U. Lohmann. Impact of improved near infrared water vapor line data on absorption of solar radiation in GCMs. *Geophysical Research Letters*, 28:4591–4595 (2001).
- Berk, A., L. Bernstein, and D. Robertson. MODTRAN: A moderate resolution model for LOWTRAN. GL - TR -89 - 0122, Air Force Geophys. Lab., Hascom AFB, Mass., USA (1989).
- Bishop, J. and W. Rossow. Spatial and temporal variability of global surface solar irradiance. *Journal of Geophysical Research*, 99:16,839–16,858 (1991).
- Boers, R., A. van Lammeren, and A. Feijt. Accuracy of cloud optical depth retrievals from ground based pyranometers. *Journal of Atmosphere and Ocean Technology*, 17:916–927 (2000).
- Boucher, O. On aerosol direct shortwave forcing and the Henyey-Greenstein phase function. *Journal of the Atmospheric Sciences*, 55:128–134 (1998).

REFERENCES

- Bowker, D., R. Davis, D. Myrik, K. Stacy, and W. Jones. Spectral reflectances of natural targets for use in remote sensing studies. NASA Ref. Pub. 1139, NASA, Washington, D.C., USA (1985).
- Bush, B., F. Valero, A. Simpson, and L. Bignone. Characterization of thermal effects in pyranometers: A data correction algorithm for improved measurement of surface insolation. *Journal of Atmosphere and Ocean Technology*, 17:165–175 (2000).
- Cahalan, R. and J. Joseph. Fractal statistics of cloud fields. *Monthly Weather Review*, 117:261–272 (1989).
- Cahalan, R. F., W. Ridgway, W. J. Wiscombe, and T. L. Bell. The albedo of stratocumulus clouds. *Journal of the Atmospheric Sciences*, 51:2434–2455 (1994).
- Cairns, B., A. Lacis, and B. Carlson. Absorption within inhomogeneous clouds and its parameterization in general circulation models. *Journal of the Atmospheric Sciences*, 57:700–714 (2000).
- World Radiation Center. *Calibration Certificate Kipp en Zonen CM 11 SN: 0123010-02*. Davos, Switzerland (2000).
- Cess, R., M. Zhang, P. Minnis, L. Corsetti, E. Dutton, B. Forgan, D. Garber, W. Gates, J. Hack, E. Harrison, X. Jing, J. Kiehl, C. Long, J. Morcrette, G. Potter, V. Ramanathan, B. Subasilar, C. Whitlock, D. Young, and Y. Zhou. Absorption of solar radiation by clouds: observations versus models. *Science*, 267:496–499 (1995).
- Cess, R. D., G. Potter, J. Blanchet, G. Boer, A. Del Genio, M. Deque, V. Dymnikov, V. Galin, W. Gates, S. Ghan, J. Kiehl, A. Lacis, H. Le Treut, Z. Li, X. Liang, B. McAvaney, V. Meleshko, J. Mitchell, J. Morcrette, D. Randall, L. Rikus, E. Roeckner, J. Royer, U. Schlese, D. Sheinin, A. Slingo, A. Sokolov, K. Taylor, W. Washington, R. Wetherald, I. Yagai, and M. Zhang. Intercomparison and interpretation of climate feedback processes in 19 atmospheric general circulation models. *Journal of Geophysical Research*, 95(D20):16,601–16,615 (1990).
- Cess, R. D., T. Qian, and M. Sun. Consistency tests applied to the measurement of total, direct and diffuse shortwave radiation at the surface. *Journal of Geophysical Research*, 105(D20):24,881–24,887 (2000).
- Chandrasekhar, S. *Radiative Transfer*. Dover, New York, USA (1960).
- Chang, F. and Z. Li. Examining the relationship between cloud and radiation quantities derived from satellite observation and model calculations. *Journal of Climate*, 13:3342–3858 (2000).
- Christensen, J., O. Christensen, P. Lopez, E. van Meijgard, and M. Botzet. The HIRHAM4 regional atmospheric climate model. DMI Scientific Report 96-4, Danish Meteorological Institute, Copenhagen, Denmark (1996).
- CLIWA-NET. CLIWA-NET web page (2002).
<http://www.knmi.nl/samenw/cliwa-net/>.

- Clough, S. A., F. X. Kneizys, and R. W. Davis. Line shape and the water vapor continuum. *Atmospheric Research*, 23:229–241 (1989).
- Coley, P. and P. Jonas. The influence of cloud structure and droplet concentration on the reflectance of shortwave radiation. *Annales Geophysicae*, 14(8):845–852 (1996).
- Crewell, S., M. Drusch, E. van Meijgaard, and A. van Lammeren. Cloud observations and modeling within the European BALTEX Cloud Liquid Water Network. *Boreal Environmental Research*, 7:235–245 (2002).
- Csiszar, I. and G. Gutman. Mapping global land surface albedo from NOAA AVHRR. *Journal of Geophysical Research*, 104(D6):6215–6228 (1999).
- Dutton, E., J. Michalsky, T. Stoffel, B. Forgan, J. Hickey, D. W. Nelson, T. L. Alberta, and I. Reda. Measurement of broadband diffuse solar irradiance using current commercial instrumentation with a correction for thermal offset errors. *Journal of Atmosphere and Ocean Technology*, 18:297–314 (2001).
- EUMETSAT. Meteosat Second Generation System Overview. EUM-TD 07, EUMETSAT, Darmstadt, Germany (2001). Available from <http://www.eumetsat.de>.
- EUROCS. EUROCS web page (2002).
<http://www.cnrm.meteo.fr/gcss/EUROCS/EUROCS.html>.
- Feijt, A. *Quantitative Cloud Analysis using Meteorological Satellites*. Ph.D. thesis, Wageningen Universiteit, Wageningen, The Netherlands (2000).
- Feijt, A. and H. Jonker. Comparison of scaling parameters from spatial and temporal distributions of cloud properties. *Journal of Geophysical Research*, 105(D12):29,089–29,097 (2000).
- Fouquart, Y. and B. Bonnel. Computations of solar heating of the earth's atmosphere: A new parameterization. *Beiträge zur Physik der Atmosphäre*, 53:32–62 (1980).
- Fouquart, Y., B. Bonnel, and V. Ramaswamy. Intercomparing shortwave radiation codes for climate studies. *Journal of Geophysical Research*, 96:8955–8968 (1991).
- Fröhlich, C. History of solar radiometry and the World Radiometric Reference. *Metrologica*, 28:111–115 (1991).
- Frouin, R., D. Ligner, C. Gautier, K. Baker, and R. Smith. A simple analytical formula to compute clear sky total and photosynthetically available solar irradiance at the ocean surface under clear skies. *Journal of Geophysical Research*, 94:9731–97,108–124 (1989).
- Fu, Q. and K. Liou. On the correlated k-distribution method for radiative transfer in nonhomogeneous atmospheres. *Journal of the Atmospheric Sciences*, 49:2139–2156 (1992).

REFERENCES

- Giver, L., C. Chackerian, and P. Varanasi. Visible and near infrared H_2^{16} line intensity correction for HITRAN96. *Journal of Quantitative Spectroscopy and Radiative Transfer*, 66:101–105 (2000).
- Goody, R. and Y. Yung. *Atmospheric Radiation - Theoretical Basis*. Oxford University Press, Oxford, UK (1989).
- Gustaffson, N. HIRLAM 2 Final Report. HIRLAM Tech Report No. 1, Swedish Meteorological and Hydrological Institute, Norrköping, Sweden (1993).
- Halthore, R., S. Nemesure, S. Schwartz, D. Imre, and A. Berk. Models overestimate diffuse clear-sky surface irradiance: A case for excess atmospheric absorption. *Geophysical Research Letters*, 25:3591–3594 (1998).
- Halthore, R. N., S. E. Schwartz, J. Michalsky, G. Anderson, R. Ferrare, B. Holben, and H. Ten Brink. Comparison of model estimated and measured direct-normal solar irradiance. *Journal of Geophysical Research*, 102:29,991–30,002 (1997).
- Han, Q., W. Rossow, and A. Lacis. Near-global survey of effective droplet radii in liquid water clouds using ISCCP data. *Journal of Climate*, 7:465–497 (1994).
- Heney, L. and J. Greenstein. Diffuse radiation in the galaxy. *Astrophysical Journal*, 93:70–83 (1941).
- Hess, M., R. Koelemeijer, and P. Stammes. Scattering matrices of imperfect hexagonal ice crystals. *Journal of Quantitative Spectroscopy and Radiative Transfer*, 60:301–308 (1998).
- Hess, M. and M. Wiegner. COP: a data library of optical properties of hexagonal ice crystals. *Applied Optics*, 33:7740–7746 (1994).
- Holben, B. N., T. F. Eck, I. Slutsker, D. T. amd J. P. Buis, A. Setzer, E. Vermote, J. A. Reagan, Y. J. Kaufman, T. Nakajima, F. Lavenu, I. Jankowiak, and A. Smirnov. AERONET- a federated instrument network and data archive for aerosol characterization. *Remote Sensing of Environment*, 66:1–16 (1998).
- Hu, Y. and K. Stamnes. An accurate parameterization of the radiative properties of water clouds suitable for use in climate models. *Journal of Climate*, 6:728–742 (1993).
- Hu, Y. and K. Stamnes. Climate sensitivity to cloud optical properties. *Tellus*, 52B:81–93 (2000).
- van de Hulst, H. *Light Scattering by Small Particles*. Wiley, New York, USA (1957).
- van de Hulst, H. *Multipole Light Scattering, Tables, Formulas, and Applications*. Academic Press, New York, USA (1980).
- ISO. Solar energy – specification and classification of instruments for measuring hemispherical solar direct solar radiation. ISO-TR 9060, International Organization for Standardization, Geneva, Switzerland (1996).

- Isobe, T., E. Feigelson, M. Akritas, and G. Babu. Linear regression in astronomy. *Astrophysical Journal*, 364:104–113 (1990).
- Jolivet, D. and A. Feijt. Cloud thermodynamic phase and particle size estimation using 0.67 and 1.6 micrometer channels from meteorological satellites. *submitted to Annales Geophysicae* (2002).
- Kato, S., T. Ackerman, E. Clothiaux, J. Mather, G. Mace, M. Weseley, F. Murcray, and J. Michalsky. Uncertainties in modeled and measured clear sky surface short wave irradiances. *Journal of Geophysical Research*, 102:25,881–25,898 (1997).
- Kato, S., T. Ackerman, J. Mather, and E. Clothiaux. The k-distribution method and correlated-k approximation for a shortwave radiative transfer model. *Journal of Quantitative Spectroscopy and Radiative Transfer*, 62:109–121 (1999).
- Kidwell, K. B. NOAA polar orbiter data (POD) user's guide. Technical report, National Oceanic and Atmospheric Administration, Suitland, , USA (1998). Available from <http://www2.ncdc.noaa.gov/docs/podug/>.
- King, M. Determination of the scaled optical thickness of clouds from reflected solar radiation measurements. *Journal of the Atmospheric Sciences*, 44:1734–1751 (1987).
- Knap, W., L. Labonnote, G. Brogniez, and P. Stammes. Modelling light scattering in ice clouds using various ice crystal models: validation with POLDER and ATSR-2 measurements. *in preparation* (2002).
- Kratz, D. The correlated k-distribution technique as applied to the AVHRR channels. *Journal of Quantitative Spectroscopy and Radiative Transfer*, 53:501–517 (1995).
- Kriebel, K. Cloud liquid water path derived from AVHRR data using APOLLO. *International Journal of Remote Sensing*, 10:723–729 (1989).
- Kuik, F. Global radiation measurements in the operational KNMI meteorological network - effects of pollution and ventilation. TR-197, Koninklijk Nederlands Meteorologisch Instituut, De Bilt, the Netherlands (1997).
- Kurucz, R. The solar irradiance by computation. In Anderson, G., R. Picard, and J. H. Chetwynd (editors), *Proceedings of the 17th Annual Review Conference on Atmospheric Transmission Models* (1995).
- Kylling, A. and B. Mayer. libRadtran V0.99 user manual. available from <http://www.libradtran.org> (2001).
- Lacis, A., J. Chowdhary, M. Mishchenko, and B. Cairns. Modeling errors in diffuse-sky radiation: Vector versus scalar treatment. *Geophysical Research Letters*, 25:135–138 (1998).
- Lenoble, J. *Atmospheric Radiative Transfer*. A. Depaak Publishing, Hampton, Virginia, USA (1993).

REFERENCES

- Leontyeva, E. and K. Stamnes. Estimation of cloud optical thickness from ground-based measurements of incoming solar radiation in the arctic. *Journal of Climate*, 7:566–578 (1994).
- Li, Z. and H. Leighton. Narrowband to broadband conversion with spatially autocorrelated reflectance measurements. *Journal of Applied Meteorology*, 31:421–330 (1992).
- Li, Z., K. Masuda, and T. Takashima. Estimation of SW flux absorbed at the surface from TOA reflected flux. *Journal of Climate*, 6:317–330 (1993).
- Loeb, N. G. In-flight calibration of NOAA AVHRR visible and near-IR bands over Greenland and Antarctica. *International Journal of Remote Sensing*, 18:477–490 (1997).
- Long, C. and T. Ackerman. Surface measurements of solar irradiance: A study of the spatial correlation between simultaneous measurements at separated sites. *Journal of Applied Meteorology*, 34:1039–1046 (1995).
- Lorenz, E. Available potential energy and the maintenance of general circulation. *Tellus*, 7:157–167 (1955).
- Lyddane, R. H. Small eccentricities or inclinations in the Brouwer theory of the artificial satellite. *The Astronomical Journal*, 68:555–558 (1963).
- Macke, A., J. Müller, and E. Raschke. Single scattering properties of atmospheric ice crystals. *Journal of the Atmospheric Sciences*, 53:2813–2825 (1996).
- Mandelbrot, B. *The fractal geometry of nature*. W.H. Freeman and Company, San Francisco, USA (1982).
- C.-Labonnote, L., G. Brogniez, M. Doutriaux-Boucher, J. Gayet, J. Buriez, and H. Chepfer. Modeling of light scattering in cirrus clouds with inhomogeneous hexagonal monocrystals: Comparison with in-situ and ADEOS-POLDER measurements. *Geophysical Research Letters*, 27:113–116 (2000).
- Doutriaux-Boucher, M., J. Buriez, G. Brogniez, and L. C.-Labonnote. Sensitivity of retrieved POLDER directional cloud optical thickness to various ice particle models. *Geophysical Research Letters*, 27:109–112 (2000).
- Intergovernmental Panel on Climate Change*, J. Houghton, Y. Dings, D. Griggs, M. Noguer, P. van der Linden, X. Dai, K. Maskell, and C. Johnson (editors). *Climate Change 2001: The Scientific Basis*. Cambridge Univ. Press, Cambridge, UK (2001).
- Kipp en Zonen. *Instruction Manual Pyranometer CM 11*. Delft, The Netherlands (1992).
- van Meijgaard, E., U. Andrae, and B. Rockel. Comparison of model predicted cloud parameters and surface radiative fluxes with observations on the 100 km scale. *Meteorology and Atmospheric Physics*. 77:109–130 (2001).

- Michalsky, J. Errata: The Astronomical Almanac's algorithm for approximate solar position (1950-2050). *Solar Energy*, 41:113 (1988a).
- Michalsky, J. The Astronomical Almanac's algorithm for approximate solar position (1950-2050). *Solar Energy*, 40:227–235 (1988b).
- Mie, G. A contribution to the optics of turbid media, especially colloidal metallic suspensions. *Annalen der Physik*, 25(4):377–445 (1908).
- Miloshevich, L., H. Vömel, A. Paukkunen, A. Heymsfield, and S. Oltmans. Characterization and correction of relative humidity measurements from Vaisala RS80-A radiosondes at cold temperatures. *Journal of Atmosphere and Ocean Technology*, 18:135–156 (2001).
- Min, Q. and L. Harrison. Cloud properties derived from surface MFRSR measurements and comparison with GOES results at the ARM SGP site. *Geophysical Research Letters*, 23:1641–1644 (1996).
- Mishchenko, M., J. Penner, and D. Anderson. Editorial: Global aerosol climatology project. *Journal of the Atmospheric Sciences* (2002).
- Mitchell, R. M. In-flight characteristics of the space count of NOAA AVHRR channel 1 and 2. Technical report, CSIRO Atmospheric Research Division, Aspendale, Australia (2001).
- Mlawer, E., P. Brown, S. Clough, L. Harrison, J. Michalky, P. Kiedron, and T. Shipert. Comparison of spectral direct and diffuse solar irradiance measurements and calculations for cloud-free conditions. *Geophysical Research Letters*, 25:3591–3594 (1998).
- Nguyen, L., P. Minnis, J. K. Ayers, and D. R. Doeling. Intercalibration of meteorological satellite imagers using VIRS, ATSR-2 and MODIS. In *AMS 11th Conference of Atmospheric Radiation* (2001).
- Nicolet, M. On the molecular scattering in the terrestrial atmosphere: An empirical formula for its calculation in the homosphere. *Planetary and Space Science*, 32:1467–1468 (1984).
- Nordeng, T. Extended versions of the convective parameterization scheme at ECMWF and their impact on the mean and transient activity of the model in the tropics. Technical Memorandum No. 206, European Centre for Medium Range Weather Forecasts, Reading, UK (1994).
- Ohmura, A., E. Dutton, B. Forgan, C. Frhlich, H. Gilgen, H. Hegner, A. Heimo, G. König-Langlo, B. McArthur, G. Müller, R. Philipona, R. Pinker, C. Whitlock, K. Dehne, and M. Wild. Surface Radiation Network (BSRN/WCRP): New precision radiometry for climate research. *Bulletin of the American Meteorological Society*, 79(10):2115 – 2136 (1998).

REFERENCES

- Oreopoulos, L. and H. Barker. Accounting for subgrid-scale cloud variability in a multi-layer 1d solar radiative transfer algorithm. *Quarterly Journal of the Royal Meteorological Society*, 125:301–330 (1999).
- Penner, J. R. C., J. Hales, N. Laulainen, R. Leifer, T. Novakov, J. Ogren, L. Radke, S. Schwartz, and L. Travis. Quantifying and minimizing uncertainty of climate forcing by anthropogenic aerosols. *Bulletin of the American Meteorological Society*, 75:375–400 (1994).
- Philipona, R. Underestimation of solar global and diffuse radiation measured at the Earth’s surface. *submitted to Journal of Geophysical Research* (2002).
- Pinker, R., R. Frouin, and Z. Li. A review of satellite methods to derive surface shortwave irradiance. *Remote Sensing of Environment*, 51:108–124 (1995).
- Pruppacher, H. and J. Klett. *Microphysics of clouds and precipitation*. D. Reichel Publishing Company, Dordrecht, The Netherlands (1978).
- Ramanathan, V. The role of earth radiation budget studies in climate and general circulation research. *Journal of Geophysical Research*, 92:4075–4095 (1987).
- Ramanathan, V., R. Cess, E. Harrison, P. Minnis, B. Barkstrom, E. Ahmad, and D. Hartmann. Cloud-radiative forcing and climate: Results from the Earth Radiation Budget Experiment. *Science*, 243:57–63 (1989).
- Ramanathan, V., B. Subasilar, G. Zhang, W. Conant, R. Cess, J. Kiehl, H. Grassl, and J. Shi. Warm pool heat budget and shortwave cloud forcing: a missing physics? *Science*, 267:499–503 (1995).
- Rao, C. R. N. and J. Chen. Post-launch calibration of the visible and near-infrared channels of the Advanced Very High Resolution Radiometer on the NOAA-14 spacecraft. *International Journal of Remote Sensing*, 17:2743–2747 (1996).
- Rao, C. R. N. and J. Chen. Revised post-launch calibration of the visible and near-infrared channels of the Advanced Very High Resolution Radiometer on the NOAA-14 spacecraft. *International Journal of Remote Sensing*, 20:3485–3491 (1999).
- Rice, J. *Mathematical statistics and data analysis*. Wadsworth & Brooks/Cole, Belmont, USA (1988).
- Roeckner, E., K. Arpe, L. Bentsson, M. Christoph, M. Claussen, L. Dümenil, M. Esch, M. Giorgetta, U. Schlese, and U. Schulzweida. The atmospheric general circulation model ECHAM4: Model description and simulation of present-day climate. Rep. 218, Max Planck Institut für Meteorologie, Hamburg, Germany (1996).
- Rossow, W., C. Delo, and B. Cairns. Implications of the observed mesoscale variations of clouds for the Earth’s radiation budget. *Journal of Climate*, 15:557–585 (2002).

- Rossow, W. and A. Lacis. Global, seasonal cloud variations from satellite radiance measurements. part II: Cloud properties and radiative effects. *Journal of Climate*, 2:419–462 (1990).
- Rossow, W. and R. Schiffer. ISCCP cloud data products. *Bulletin of the American Meteorological Society*, 72:2–20 (1991).
- Rossow, W., A. Walker, D. Beuschel, and M. Rolter. International Satellite Cloud Climatology Project (ISCCP): Documentation of new cloud datasets. WMO/TD 703, World Meteorological Organization, Geneva, Switzerland (1996).
- Rothman, L., R. Gamanche, A. Barbe, A. Goldman, J. Gilis, L. Brown, R. Toth, J. Flaud, and C. Camy-Peyret. AFGL atmospheric line parameters compilation: 1982 edition. *Applied Optics*, 22:2247–2256 (1983).
- Rothman, L., C. Rinsland, A. Goldman, S. Massie, D. Edwards, J. Flaud, A. Perrin, C. C. Peyret, V. Dana, J. Mandin, J. Schroeder, A. McCann, R. Gamache, R. Wattson, K. Yoshino, K. Chance, K. Jucks, L. Brown, V. Nemtchinov, and P. Varanasi. The HITRAN molecular spectroscopic database and HAWKS (HITRAN atmospheric workstation). *Journal of Quantitative Spectroscopy and Radiative Transfer*, 60:665–710 (1998).
- Rothman, L. S., R. R. Gamach, R. H. Tipping, C. P. R. M. A. H. Smith, D. C. Benner, V. M. Devy, J.-M. Flaud, C. Camy-Peyret, A. Perrin, A. Goldman, S. T. Massie, L. R. Brown, and R. A. Toth. The HITRAN molecular database: Editions of 1991 and 1992. *Journal of Quantitative Spectroscopy and Radiative Transfer*, 48:469–507 (1992).
- Russchenberg, H., A. van Lammeren, S. Heijnen, and D. Swart. Cabauw Experimental Site for Atmospheric Research: CESAR, project plan. Technical report, KNMI, De Bilt, the Netherlands (2001).
- Salomonson, V., W. Barnes, P. Maymon., H. Montgomery, and H. Ostrow. MODIS: advanced facility instrument for studies of the Earth as a system. *IEEE Transactions on Geoscience and Remote Sensing*, 27(2):145–153 (1989).
- Schmetz, J. Towards a surface radiation climatology: Retrieval of downward irradiances from satellites. *Atmospheric Research*, 23:287–321 (1989).
- Shettle, E. and R. Fenn. Models for the aerosols of the lower atmosphere and the effects of humidity variations on their optical properties. Environmental Research Paper 675, Air Force Geophys. Lab. (1979).
- Slingo, A. Sensitivity of the Earth's radiation budget to changes in low clouds. *Nature*, 343:49–51 (1990).
- Spencer, J. W. Fourier series representation of the position of the sun. *Journal of Climate*, 6:1764–1772 (1971).

REFERENCES

- Spencer, J. W. Comments on the Astronomical Almanac's algorithm for approximate solar position (1950-2050). *Solar Energy*, 42:353 (1989).
- Stammes, P. and J. Henzing. Multispectral aerosol optical thickness at De Bilt 1997-1999. *Journal of Aerosol Sciences*, 31:283-284 (2000).
- Stammes, K., S. Tsay, W. Wiscombe, and K. Jayaweera. Numerically stable algorithm for discrete-ordinate-method radiative transfer in multiple scattering and emitting layered media. *Applied Optics*, 27:2502-2509 (1988).
- Stephens, G. How much solar radiation do clouds absorb? *Science*, 271:1131-1133 (1996).
- Sundqvist, H. A parameterization scheme for non-convective condensation including prediction of cloud water content. *Quarterly Journal of the Royal Meteorological Society*, 104:677-690 (1978).
- Sundqvist, H., E. Berge, and J. Kristjansson. Condensation and cloud parameterization studies with a mesoscale numerical weather prediction model. *Monthly Weather Review*, 117:1641-1657 (1989).
- Suttles, J., R. Green, P. Minnis, G. Smith, W. Staylor, B. Wielicki, I. Walker, D. Young, V. Taylor, and L. Stowe. Angular radiation models for Earth-atmosphere systems. Vol. I - shortwave radiation. NASA RP-1184, National Space Agency, Washington D.C., USA (1988).
- Suttles, J. and G. Ohring. Report of the Workshop on Surface Radiation Budget for Climate Applications. WCRP, WC-119, WMO/TD 109, World Meteorological Organization, Geneva, Switzerland (1986).
- Tahnk, W. R. and J. A. Coakley. Improved calibration coefficients for NOAA-14 AVHRR visible and near-infrared channels. *International Journal of Remote Sensing*, 22:1269-1283 (2001a).
- Tahnk, W. R. and J. A. Coakley. Updated calibration coefficients for NOAA-14 AVHRR channels 1 and 2. *International Journal of Remote Sensing*, 22:3053-3057 (2001b).
- Teillet, P. Rayleigh optical depth comparison from various sources. *Applied Optics*, 26:1897-1900 (1990).
- Ten Brink, H., C. Kruisz, G. Kos, and A. Berner. Composition/size of the light-scattering aerosol in the Netherlands. *Atmospheric Environment*, 31(23):2502-2508 (1997).
- Tiedtke, M. A comprehensive mass flux scheme for cumulus parameterization in large-scale models. *Monthly Weather Review*, 121:1779-1800 (1989).
- Tiedtke, M. An extension of cloud-radiation parameterization in the ECMWF model: The representation of subgrid-scale variations of optical depth. *Monthly Weather Review*, 124:745-750 (1996).

- Valero, F. and B. Bush. Measured and calculated clear-sky solar radiative fluxes during the Subsonic Aircraft Contrail and Cloud Effects Special Study (SUCCESS). *Journal of Geophysical Research*, 104:165–175 (1999).
- Várnai, T. and A. Marshak. Statistical analysis of the uncertainties in cloud optical depth retrievals caused by three-dimensional radiative effects. *Journal of the Atmospheric Sciences*, 58:1540–1548 (2001).
- Vermote, E. and Y. J. Kaufman. Absolute calibration of AVHRR visible and near-infrared channels using ocean and cloud views. *International Journal of Remote Sensing*, 16:2317–2340 (1995).
- Vermote, E. and N. El Saleous. private communications (1999). Listed at <http://www.dar.csiro.au/rs/CalWatch/>.
- Wardle, D., L. Dahlgren, K. Dehne, L. Liedquist, L. McArthur, Y. Miyake, O. Motschka, C. Velds, and C. Wells. Improved measurement of solar irradiance by means of detailed pyranometer characterization. Rep. IEA-SHCO-9C-2, International Energy Agency, Downsview, Canada (1996).
- Wild, M. and B. Liepert. Excessive transmission of solar radiation through the cloud-free atmosphere in GCMs. *Geophysical Research Letters*, 14:2165–2168 (1998).
- Wild, M., A. Ohmura, H. Gilgen, E. Roeckner, M. Giorgetta, and J. Morcrette. The disposition of radiative energy in the global climate system: GCM versus observational estimates. *Climate Dynamics*, 24:853–869 (1998).
- WMO. WMO international radiosonde intercomparison: Final report. WMO-No. 59, World Meteorological Organization, Geneva, Switzerland (1993).
- WMO. Guide to meteorological instruments and methods of observation. WMO-No. 8, 6th Edition, World Meteorological Organization, Geneva, Switzerland (1996).

Acknowledgements

This Ph.D. thesis has been made possible, improved and influenced by the contributions of several people. Here, I would like to take the opportunity and thank everybody who had an influence in one way or another on the final outcome.

My promoter Prof. Dr. Clemens Simmer and the second referee Dr. Susanne Crewell from the Meteorological Institute of the University of Bonn (MIUB) initiated my contact to the research department of the Koninklijk Nederlands Meteorologisch Instituut (KNMI) and thus provided me with the unique opportunity to work in a stimulating research environment. During the course of my Ph.D., Clemens supported my research with suggestions, criticism and advice on the general direction. However, it was not only the work relation, but also the personal atmosphere which made my contacts to you and the MIUB very pleasant.

My supervisors at the KNMI, Dr. Andre van Lammeren, Dr. Erik van Meijgaard and Dr. Arnout Feijt deserve a warm thank-you for making my stay at KNMI possible in the first place, and for their assistance, encouragement and constructive criticism during the course of my research. Starting as an inexperienced scientist directly after graduation from University, I learnt a lot from your expertise and enjoyed the time working together with you both on a professional and personal level.

Several aspects of my work have greatly benefited from valuable input my colleagues at the KNMI gave on my work. Thanks go in particular to Bas Henzing for the discussions on pyranometer uncertainties and the support with the MODTRAN calculations, to Dr. Rose Dhopolsky for advice and support with the processing of AVHRR data, and to Dr. Piet Stammes for advice on the representation of aerosols in radiative transfer calculations, as well as providing me with sun photometer data on aerosol optical depth. Such a list of names will always remain incomplete to some extent. Thus, I generally want to say thank you to all other colleagues at KNMI, and in particular to the Atmospheric Research section, who answered my questions, gave me advice on particular scientific topics or provided me with data. However, it was not only the scientific expertise, but also the pleasant work atmosphere which made my stay at KNMI a unique experience.

My busy work life has been balanced and compensated by private activities. Thus, I want to thank both my friends and my family for their support and the nice times we have spent together during my stay in the Netherlands. You helped me find the energy and motivation required for writing this thesis.

Last but not least, I would like to thank my wife Sinidu. You are the only person who has managed to distract me from my work for several weeks just a few months before the end of my thesis. Our marriage was a very good reason for this. Thank you for enduring three years of weekend relationship, you have made the weekends very special.

Curriculum Vitae

I was born in Bonn, Germany, on the 31st of December 1973 as the third child and first son of Jutta Mebold, born Hanisch, and Dr. Ulrich Mebold. I grew up in Bonn until 1975, when my family moved to Sydney, Australia and my father worked as a visiting scientist at the Institute of Radio Physics of the Commonwealth Scientific and Industrial Research Organization for two years. Shortly after our return to Bonn, my family moved to the close-by town of Meckenheim in 1978. I visited the Evangelische Gemeinschaftsgrundschule from 1980 until summer 1984 and continued my school education at the Konrad-Adenauer Gymnasium. My youth in Meckenheim was interrupted by two half-year stays in Tuscon, Arizona, and Sydney, Australia, in 1985 and 1990, respectively, during research sabbaticals of my father. After my graduation from high-school with the German *Abitur* in June 1993, I commenced a university course in physics at the *Rheinische-Friedrich Wilhelms Universität* in Bonn in October of the same year. During the year 1996, I visited the *University of New South Wales* in Sydney, Australia, as participant of the programme *Integriertes Auslandsstudium* organized by the *Deutsche Akademische Auslandsdienst*. During this stay, I completed a four-month long *honour's project* on the absorption of solar radiation by atmospheric aerosols under the supervision of Dr. Michael Box and gained my first experiences in atmospheric radiative transfer. In 1997, I commenced a job as an undergraduate research assistant at the Meteorological Institute of the University of Bonn, where I wrote software for data acquisition, and visualization for a lidar ceilometer, an infrared radiometer and a micro-wave radiometer. Extending this work, I began my *Diplomarbeit* at the Meteorological Institute early in 1998 about the interpretation of ceilometer backscatter profiles. It was completed in June 1999 and is titled *Quantitative Analyse von Ceilometer-Rückstreuprofilen*. In October 1999, I started a position as a research scientist at the Koninklijk Nederlands Meteorologisch Instituut (KNMI) in De Bilt, the Netherlands, with the goal of obtaining a PhD at the University of Bonn on the basis of my scientific work. The topic of the research were the evaluation of the representation of clouds and cloud-radiation interactions in models by comparison to ground-based and satellite measurements. In May 2002, I married Sinidu Deneke and changed my family name from Mebold to Deneke. This thesis presents a summary of my work done during my employment at the KNMI, which ended in November 2002.